Phenomenological Study of Radar Scattering at High Millimeter-Wave Frequencies in Support of Autonomous Vehicles

by

Abdulrahman A. Alaqeel

A dissertation submitted in partial fulfillment
of the requirements for the degree of
Doctor of Philosophy
(Electrical and Computer Engineering)
in the University of Michigan
2022

Doctoral Committee:

- Professor Kamal Sarabandi, Chair
- Professor Eric Michielssen
- Associate Research Scientist Dr. Adib Nashashibi
- Professor Christopher Ruf
- Professor Fawwaz Ulaby

Abdulrahman A. Alaqeel
alaqeel@umich.edu
ORCID iD: 0000-0001-8214-278X

DEDICATION

To my family, with love and gratitude.

ACKNOWLEDGMENTS

First of all, all my thanks and praises go to God (Allah). We praise Him as He has praised Himself. Second, I would like to offer my deepest gratitude and most indebtedness toward my parents, my mother for her affection, love, and care, and my father for believing in me, for his support and encouragement. Everything I achieve in my life is owed to them. I would also like to thank my grandparents for always believing in me and for their endless support.

At the end of this journey, I would like to express my sincere gratitude to my PhD adviser Professor Kamal Sarabandi. His continuous support, guidance, and encouragement were indispensable. He is a perfect mentor and an exceptional educator. I am honored to be one of his students.

Special thanks go to Dr. Adib Nashashibi for his continuous support and guidance. His expertise and advice were invaluable. I am grateful for his generosity and all his time and efforts in supporting me during my graduate studies. I am also thankful to him for serving on my thesis committee and for his valuable feedback.

I would also like to thank professor Fawwaz Ulaby for serving on my thesis committee. His invaluable input and special care are greatly appreciated. It was a privilege to be one of his students and to have him serve on my PhD committee. Appreciation is also extended toward Professor Eric Michielssen and Professor Christopher Ruf for being members of the dissertation committee and for their valuable inputs and suggestions.

I would like to take this opportunity to thank current and former colleagues at the Radiation Laboratory at the University of Michigan and the friends whom I was lucky to have at Ann Arbor. I am thankful to Abdulrahman Aljurbua, Amr Ibrahim, Austin Travis, Mostafa Zaky, Navid Barani, Mani Kashanianfard, Abdullah Alburadi, Abdelhamid Nasr, Tanner Douglas, Saud Alrufaydah, Omar Bakry, Zainulabideen Khalifa, Faris Alsolamy, Nasser Aldaghri. I have been very blessed to be surrounded by such great people.

I also want to thank the graduate program coordinator Kristen Thornton for her kindness and willingness to help at any time.

I am genuinely grateful for my brothers and sisters, whom I really missed during these years away from home. They are the best. Their support and kind words have always been sources of motivation. Many thanks to Abdullah, Mohammad, Nora, Omar, and all of them.

My deepest gratitude goes to my wife Nora for her endless support and love. She has always been there for me. I cannot thank her enough, and I am indebted to her. I am also very grateful for our son Abdulaziz and all the joy he brought to our life.

TABLE OF CONTENTS

LIST OF FIGURES

FIGURE

LIST OF TABLES

TABLE

ABSTRACT

There has been significant investment in realizing autonomous vehicles technology. Despite tremendous efforts and investments, the initial optimism in achieving total autonomy has not yet been materialized. This is not totally surprising as the required false alarm rate and probability of detection are very stringiest for a complex navigation problem which includes fast-changing scenarios of many dynamic obstacles of different kinds. This situation is often exacerbated by inclement weather and road conditions. In an effort to improve sensors' capabilities, this thesis focuses on examining the applications and advantages of polarimetric J-band (220 – 325 GHz) radars for driverless cars.

Automotive radars operating at lower J-band frequencies are envisioned to replace the current 77-GHz systems in vehicles for their superior resolution, compact size, and wider bandwidth. This dissertation aims at studying the polarimetric radar response of typical traffic scenes at this frequency. For highly automated vehicles, identifying each target on the road and its vicinity is crucial in planning the navigation and ensuring safety for all. Characterization of the radar backscatter from various objects enables their identification in traffic scenes and is necessary for optimizing the design of automotive sensors. The polarization signature of different targets can help with sematic mapping of targets on the road, especially for those targets that may be in the same range and Doppler bin.

Considering vehicles as the most critical objects for automotive radars to detect and locate, a thorough study is conducted to investigate the response of vehicles from different

aspects. This experimental study aims to identify the scattering phase centers on different vehicle bodies and determine the statistics of the radar return. A vehicle's orientation and movement can be predicted from these features. In addition, the statistical parameters of the response are very distinct, and hence accurate determination can be made.

Another study focuses on investigating and characterizing the response from various road surfaces. The knowledge of the expected radar signal from these surfaces is not only helpful in developing detection algorithms for other objects in the presence of this background but also for assessing the road conditions, such as detecting the presence of water, ice, snow, or harmful objects and debris on the road. Radar backscatter models are developed for various surfaces and conditions that actual measurements can be classified based on their correlation to these models.

One of the most vulnerable road users is pedestrians. The radar backscatter cross-section of the human body ($\sim$ -17 dBsm) is significantly less than that of a typical vehicle ($\sim$ 0 dBsm). The identification of pedestrians also should be performed at a further distance to allow a vehicle to react appropriately in a timely manner. As a result, backscattering from human subjects should be thoroughly examined to determine the radar return level and offer the most effective detection and identification techniques. Extensive experimental research that resulted in characterizing the polarimetric radar response and the micro-Doppler spectrum from human subjects is carried out as part of this thesis.

CHAPTER I

Introduction

Transportation is one of the most important aspects of everyday life. Despite being the most dangerous mode of transportation, driving remains the most popular. Many efforts have been made throughout the years to improve vehicle safety and convenience. Many advanced driver assistance systems (ADAS) have been designed to notify and warn drivers of potential risks, considering that the majority of accidents are caused by the driver's distraction or his delayed action, and some are caused by weather related sudden changes of conditions. ADAS functions are designed to inform drivers of nearby objects, however, currently they have limited decision making functionality. These systems are considered to be intermediate steps toward complete autonomous driving [1]. The acceleration toward autonomous vehicles will be stimulated by technology developments, ease of regulations and user contentment and assurance. The society of automotive engineers (SAE) categorized in their $J3018$ standard [2] driving automation into six levels. Level zero category is considered when all steering and acceleration are handled by the driver even with some features that provide warning and momentary assistance to the driver. When some ADASs assist in either steering, acceleration/braking based on inputs from the driver, the vehicle is considered in automation level one. Vehicles in automation level two have ADAS with sensors that are capable of supporting the driver in both steering and acceleration/braking at the same time. Automation levels three and four are assigned to vehicles with ADAS that can handle all driving functions under certain conditions only, however, in level three, the driver needs to intervene whenever needed and might be requested to take over the driving rapidly at any moment. The full automation which is categorized in level five requires systems that are capable of driving in all conditions and do not require any human intervention. These various automation and assisting levels are shown in 1.1 with more details. It should be noted that none of the commercially available vehicles at this date have gone beyond level three. The highest automation level requires significant improvements and advancements in the driving assistance systems. That includes higher sensing modality, computing capabilities, robust integration of various systems and extensive experimental testing. Moreover, environment understanding is of a great importance in the path toward full automation. At that level, vehicles might be called autonomous vehicles and various systems in the vehicle become driving systems rather than driver assistance systems.

1.1 Advanced Driver Assistance Systems

Driver assistance systems are electronic systems that are designed to enhance the safety and comfort of driving. Some of these systems were introduced in vehicles as early as 1970s. These systems often consist of some sensors to monitor both the vehicle and its surroundings to enhance the driver awareness of both the vehicle and road status. In addition to passive systems that provides the driver with some information, there are active systems that are designed to take action in some situations. The first active assistance system that was introduced to vehicles is the Anti-lock braking system (ABS) [3]. Traction control system (TCS) and Electronic stability control (ESC) along with ABS are of the earliest examples of Driver assistance systems, where their purpose reside in enhancing the mechanical stability of the vehicle [4, 1].

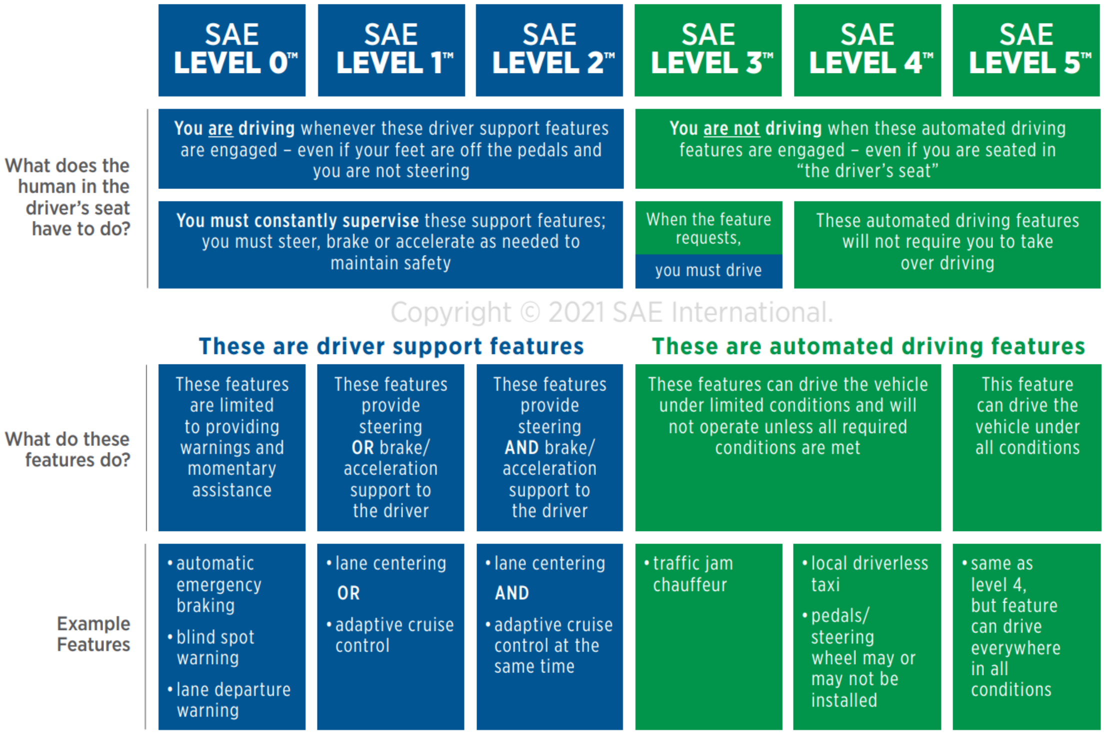

	SAE LEVEL 0™	SAE LEVEL 1™	SAE LEVEL 2™	SAE LEVEL 3™	SAE LEVEL 4™	SAE LEVEL 5™
What does the human in the driver's seat have to do?	**You are driving** whenever these driver support features are engaged – even if your feet are off the pedals and you are not steering			**You are not driving** when these automated driving features are engaged – even if you are seated in "the driver's seat"		
	You must constantly supervise these support features; you must steer, brake or accelerate as needed to maintain safety			When the feature requests, you must drive	These automated driving features will not require you to take over driving	
	These are driver support features			**These are automated driving features**		
What do these features do?	These features are limited to providing warnings and momentary assistance	These features provide steering **OR** brake/ acceleration support to the driver	These features provide steering **AND** brake/ acceleration support to the driver	These features can drive the vehicle under limited conditions and will not operate unless all required conditions are met		This feature can drive the vehicle under all conditions
Example Features	• automatic emergency braking • blind spot warning • lane departure warning	• lane centering **OR** • adaptive cruise control	• lane centering **AND** • adaptive cruise control at the same time	• traffic jam chauffeur	• local driverless taxi • pedals/ steering wheel may or may not be installed	• same as level 4, but feature can drive everywhere in all conditions

Figure 1.1: SAE Standard for Automated Driving Levels (J3016) [2]

To improve the safety of driving for both human inside the vehicle and those in other vehicles as well as pedestrians in the road, new generations of driver assistance systems focused on sensing the vehicle's surroundings by means of many sensing technologies such as Ultra-sonic, Infrared, Lidar, Radar and Vision sensors. This introduced many ADASs such as adaptive cruise control (ACC) that was first used in the late 1990s. ACC represented first kind of automation where the acceleration and deceleration are controlled by the system to maintain a specific distance to the vehicle ahead [5, 6, 7]. Earlier versions of the system were limited to operate at relatively higher driving speeds (i.g. above 30 km/hour) [1]. However, newer versions of ACC system are capable of driving in broader range of speeds, and more specifically those that have the feature of stop-and-go driving that can support the driver in traffic jams. This system was a major milestone in ADASs advancement that would not be achievable without the employment of Radar technology.

Many other advanced electronic systems have been introduced in vehicles over the past few decades that depend on various remote sensing technologies. For instant, parking assistance systems that are based on ultrasonic sensors were first used in the 1990s. Ultrasonic sensors use sound waves to measure the distance to an very close objects. Hence, these system's capabilities are limited to warn the driver, while parking, of obstacles with very coarse estimation of the distance to them [8]. After that, rear-looking cameras were employed to assist the driver in observing behind the vehicle while parking, which represented first use of vision sensor in vehicles. As parking assistance systems evolved, and with utilizing numerous sensors along with the new electronically controllable steering feature, semi-automated parking is being featured by many car manufactures [9]. The lane departure warning (LDW) system is another type of ADASs, which was followed by some flankers such as active lane keeping and lane centering assisting systems [10, 11]. These systems rely heavily on vision sensors, through tracking the road's lane markings. Their entrance to automobiles market marks another milestone in ADASs history [12, 13]. Other sensors like Lidar found its applications in vehicles for short-distance low-speed forward collision prevention. However, forward collision avoidance (FCA) systems for longer distances and higher speeds face the challenges of limited range of operation and poor resolution in Lidars, hence more advanced systems have switched to Radar technology despite the incorporated extra cost and more computational requirements [14].

Moreover, advancements in automated driving would have not been progressing without many technologies and systems beyond those installed in the vehicle. Obvious examples of such systems are Global Navigation Satellite systems (GNSS) such as the Global Positioning System (GPS), various forms of communication links weather it was dedicated communication networks or cellular networks, and many other developing technologies that are cooperative and might be part of the infrastructure such as vehicle-to-vehicle (V2V) and vehicle-to-infrastructure (V2I) communications [8, 15]. Figure 1.2 shows the time line of ADAS systems since 1980s. The figure also shows the introduction of various technologies on a rough time scale based on their first presence in vehicles.

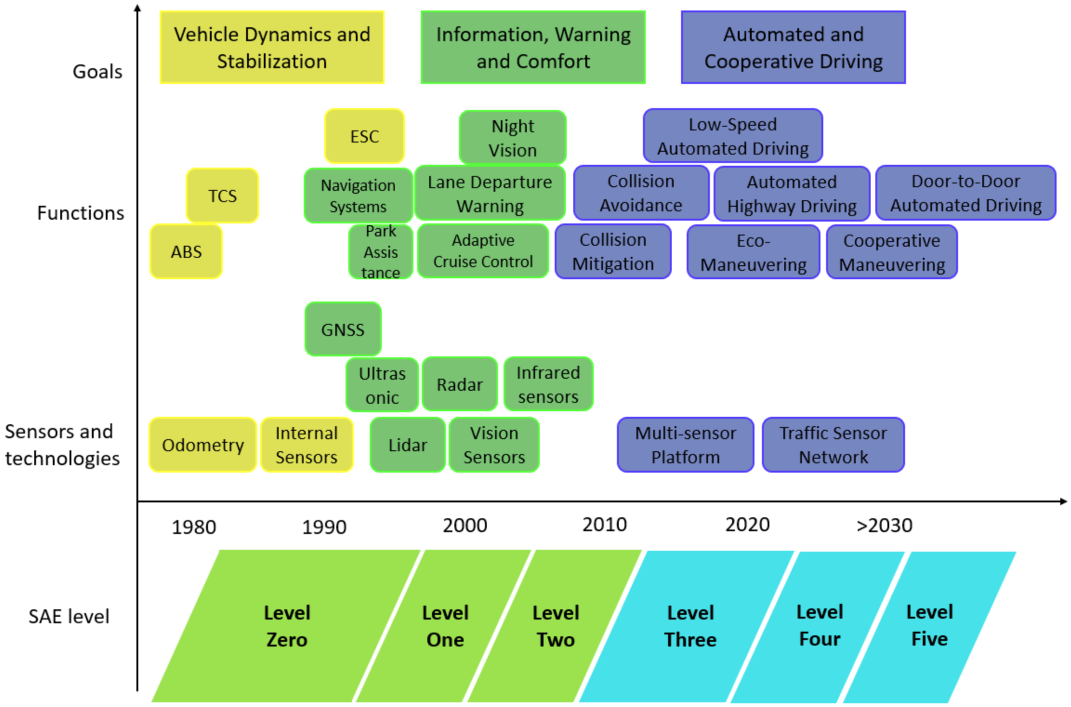

Figure 1.2: Time line of the past and expected future evolution of driving assisting systems along with technologies associated these system. Each generation is marked with a rough level of the SAE standard based on its capabilities [1]. SAE levels are outlind in the previous section and in Fig.1.1

Radars and cameras are the most common sensors nowadays and, in many cases, the sole sensors used by ADAS systems [16, 17]. The advantages of these two remote sensing technologies have shadowed all other technologies. This is apparent in both the intensive research and development that these two technologies have attracted and in the raging competition between the supporters of each of the two sensing technologies. Because cameras work in the same way as human eyes, they are prone to many of the same shortcomings that human eyes have, such as blind spots, low visibility in inclement weather and at night, and misinterpretation of some objects. However, the principle of operation in vision sensors requires least effort for interpretation by human, and hence simplifies feature extraction, algorithms development and techniques that permits processing machines to analyze and understand the driving environment based on input from such sensors. In addition, color distinction gives vision sensors the ability to read traffic signals and signs, and understand various road markings without any changes on the road infrastructures. Radars, on the other hand, operate on an entirely different principle, giving them some distinct advantages. Not only can radars work in practically any weather, produce extremely accurate relative speed and distance measurements, and have a very wide dynamic range, but they can also detect objects that are invisible to the human eye. Nevertheless, interpreting the output of radars requires some level of phenomenology studies since the response depends on many factors including the radar operating frequency and polarization. Moreover, specific adjustments to roads' infrastructure are being suggested to increase radars ability to interpret traffic signs and signals. Without diving into more detailed comparison between radar and vision sensors, many researchers believe that both are necessary and that only multi-sensor platform that integrates more than one technology would permit the envisioned full automated driving [18, 1]. That is despite many promises and limited deployments that were based on single sensing technology [19, 20]. However the author believes that radars would have a better chance of surviving if one of the two technologies —radars or cameras— were to be replaced in the future.

ACC and FCA systems were the earliest use of radar in vehicles. As the cost of radar systems started to decline and with the many advantages they offer, the promising features of radar technology have kept raising since then [21]. Nevertheless, the relatively poor resolution, cost of manufacturing, and difficulties in interpreting radar data must be improved significantly for a bigger role in the envisioned autonomous driving. The resolution issue have been addressed to some extent by operating at higher frequencies. Many companies had built radars that operated at 24 GHz, but 77 GHz became the industry standard [22]. Highly automated vehicles (HAV) require several sensors to do various tasks [23]. Given the tight space and places that a number of such sensors can occupy on the outside of a vehicle, even 77 GHz systems have a large enough size to provide adequate resolution for many applications [24, 25]. As a result, several strategies have been proposed to improve the resolution while maintaining a tolerable sensor size. Fundamentally, finer resolution might be achieved by utilizing multiple sensors or antennas, or by increasing the operating frequency. The cost associated with increasing the number of sensors is an obvious drawback. Also, the increase in processing load in addition to extra ambiguities that might be brought are more downsides of this approach. In fact, keeping the number of sensors minimal is very desired despite being a major challenge [19]. Minimizing the number of sensors simplifies the synchronization between various sensors and the number of data streams provided to the central processing unit. These factor have led researchers to propose radars operating at higher millimeter wave (MMW) frequencies. In the next two sections, the current status of automotive radar technology is discussed which dominated by 77 GHz systems. Then, the future of automotive radars is foretold which relates this introduction to the main focus of this dissertation.

1.2 Current Status of Automotive Radar Technology

As stated before, the vast majority of current automotive radars operate at 77 GHz. However, the continuing evolution of ADAS technologies places big pressure on the sensing capabilities putting various vendors and developers at competition. For instance, the three segments of radar operation in long-range (LRR), medium-range (MRR) and short-range (SRR) radars have distinct specifications and requirements. Although traditionally the three modes have their own dedicated radars, multi-mode radars that operate at different ranges would still have different requirements for each mode of operation. LRRs for example are meant to detect targets from ranges that start from 10-meter to as far as 250-m. These radars usually have relatively narrow field of view (FoV). A FoV that is about 10-15 degrees is sufficient in azimuth, and for elevation half of this is considered adequate [26, 27]. In the contrary, SRRs sense the area very close to the vehicle and often require very wide FoV that in some cases should be at least 120-degrees in azimuth and 90-degrees in elevation [28, 29]. As the field-of-view defines the angular range observed, how fine and specific this range is scanned is another criteria that is determined by the angular resolution and accuracy of the radar. Angular resolution is an important key feature in automotive radars as a non-exception from the majority of radar applications. The ability to identify the location of a specific target accurately, in the range and angle domain, and to distinguish targets of close proximity both range and angular resolutions should meet some desired minimum accuracy. With the continuous evolution of ADAS systems, a finer resolution is always strived toward. Many scientists require radars to have azimuthal resolution that are better than 1-degree in order to provide the specific accuracy called for by automation levels four and five [30]. The physical principles require a minimum size for the antenna aperture for a specific resolution. In the case of antenna arrays, the overall size of the array sets the minimum achievable resolution. Nevertheless, some techniques can achieve a specific resolution with antenna sizes smaller than traditional single apertures or simple arrays, as in some multiple-input multiple-output (MIMO) radar systems [31]. Such systems, however, require more complicated hardware and processing power, and often encompass either bandwidth or time division multiplexing [32, 33, 34].

The first 77 GHz automotive radar used in vehicles was made by Macom for Mercedes Benz in 1999 [36, 37, 38]. Since the start of this century, many companies have developed their own systems, some of which are companies that were established for this purpose in partnerships with car manufacturers [39]. Several generations of 77 GHz automotive radars are being produced by Continental AG (Conti), Veoneer, Bosch, Valeo, infineon, Texas Instrument, Aptiv, Arbe and many others. Two of these systems are discussed here to show the current technology, its limitations and the level of competition between various providers. The first example is Bosch's Front Radar Sensor Plus that was introduced in 2020 [40]. The radar is for long range detection and can detect objects as far as 210-meter. The frequency range of the system is 76-77 GHz which provides range resolution of 21-cm. The system and its antenna configurations are shown in Fig. 1.3 where the antennas configuration is shown. Three transmit and four receive antennas are used. Two of the transmit antennas have four parallel elements while the third has only one to achieve both higher gain and wide FoV in azimuth. Each of the four receive antennas have two parallel elements. The vertical and horizontal positions of various antennas are predetermined to realize a specific virtual MIMO array. Surface mounted in the center of the board is the RF front-end which is realized in monolithic microwave integrated circuit (MMIC). The MMIC chip contains three transmitting and four receiving channels that are fabricated with silicon germanium (SiGe) bipolar complementary metal-oxide semiconductor (BiCMOS) technology [41, 26, 39]. The technical characteristics of this radar are summarized in the first column of Table.1.1. The author was also aware of a newer generation of this radar that was announced by Bosch during this writing [42]. Some of the limited details about this version performance are also added in the second column of Table.1.1 for comparison. Even though it is not confirmed, the larger size and higher power consumption indicate that multiple versions of the original system (possibly four) are integrated together to achieve this finer resolution. With this

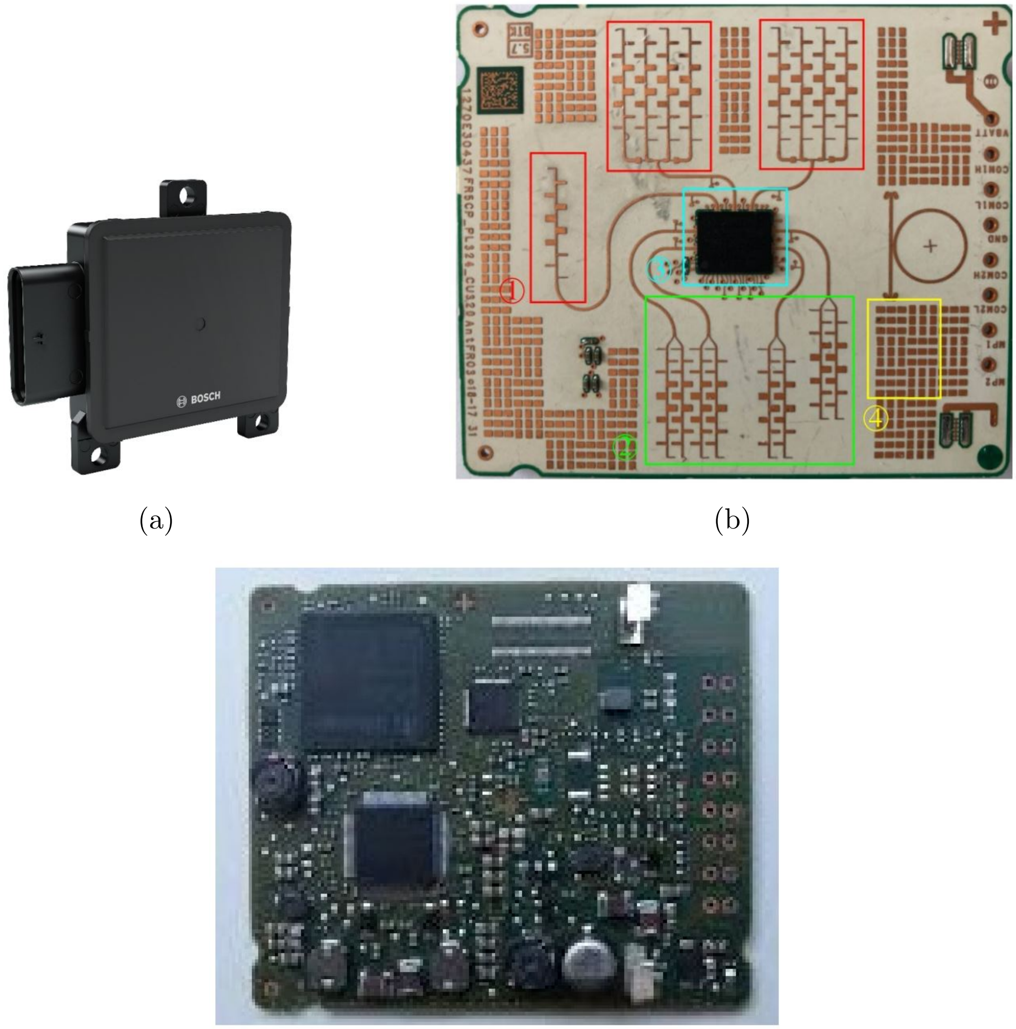

(a)

(b)

(c)

Figure 1.3: Bosch's state of the art 77 GHz automotive radar named "Front Radar Sensor Plus". (a) picture of the system in its package. (b) Photo of the printed circuit board shows antennas configuration and the RF front-end MMIC chip with marks to point the 1- the three transmit antennas with one is placed in a different vertical position than the other two, 2- the four receive antennas, 3- the MMIC RF front-end, and 4- grounded metallic cover to control the reflection from the board. (c) the other side of the radar board. Pictures are taken from Dr. Jürgen Hasch [35].

Table 1.1: Key features of some state of the art 77 GHz automotive radars.

Feature	Front Radar Sensor Plus from Bosch	Front Radar Sensor Premium from Bosch	TI's AW2243 Cascade radar prototype
Frequency	76-77 GHz	76-77 GHz	76-81 GHz
Max. detection range	210 m	302 m	350 m
Horizontal FoV	$\pm 60^o$	$\pm 60^o$	$\pm 70^o$
Vertical FoV	$\pm 15^o$	$\pm 12^o$	-
Range resolution	0.2 m	0.41 m	< 6 cm
Azimuth ang. resolution	3^o	1^o	1.4^o
Elevation ang. resolution	6^o	1^o	18^o
Velocity resolution	0.1 m/s	0.17 m/s	0.15 m/s
Size	$63 \times 72 \times 19\ mm^3$	$110 \times 143 \times 30\ mm^3$	$133 \times 157 mm^2$

assumption, the newer version would include 12 transmitting and 16 receiving channels similar to the second example.

The second example is for the prototype evaluation module that is based on Texas Instrument's AWR2243 single-chip 76-81-GHz Frequency-Modulated Continuous-Wave (FMCW) transceiver. The AWR2243 is one of a family from Texas Instrument (TI) MMW sensors that are compact, high-performance front-end, supporting fast chirp FMCW modulations. All MMW transceiver, clock and analog baseband circuits are integrated in a single die in TI's MMW CMOS technology, along with a digital sub-system for control, calibration and digital front-end [43]. The module support cascading multiple units to improve angular estimation and increase detection range. Figure 1.4a shows the front-end evaluation board for a single chip which has 3 transmit and four receive channels that are connect to identically series-fed patch antennas. The cascading capability of the device is demonstrated in development kit shown in Fig. 1.4b [44, 45]. The radar prototype in Fig. 1.4b utilizes time division multiple access (TDMA)-MIMO to achieves azimuth angular resolution as small as 1.4 degrees in short and medium ranges. In addition, the radar can increase detectability using transmit antennas beam-forming configuration. The key features of this experimental radar are listed in the third column of Table. 1.1. These two radar radar systems from Bosch and Texas Instrument show how crucial angular resolution is in ADAS sensors. In fact, angular resolution is the major disadvantage of radar compared to vision and Lidar sensors. In the next section, some prospected developments in automotive radar are presented.

1.3 New Generations of Automotive Radars

It is well established that angular resolution is the key parameter for improving performances of automotive radars [29]. In the previous section, some examples of tackling the resolution issue were presented. However, the increase of radar system complexity not only requires intricate hardware but also involves more processing time and power as well as space. For instance, the MIMO scheme requires time-division multiplexing or orthogonality between multiple transmitters. In FMCW, time-division multiplexing increases the chirp repetition period and hence limits the maximum unambiguous velocity. Even though newer frequency synthesizers can significantly reduce the chirping time, fast sweeping is constrained by linearity, noise level, maximum beat frequency, and maximum unambiguous range [39]. On the other hand, in frequency-division multiplexing, the range resolution is sacrificed [46, 47]. Some other techniques like code division multiplexing and chirp modulation have other drawbacks like liming the signal dynamic range, bandwidth deficiency, and needed sampling rates [48, 49, 39]. Despite some promising novel approaches such as radar networks, where information from multiple radars that are not necessarily coherent are used to improve the angular estimation [39, 50, 51, 52]. Automotive radars that operate at frequencies higher than 77 GHz have been envisioned for a while. That is primarily with the rapid advances in integrated circuit technologies and the deemed appealing wide bandwidth at higher MMW bands.

Two frequency ranges for radars in autonomous vehicles are under considerations by researchers at car manufacturers and suppliers and governmental labs, with frequencies around 150-160 GHz and 220-240 GHz, representing double and triple the current approved band of operation (Fig.1.5). The standard nomenclature for millimeter-wave band refers to a wide

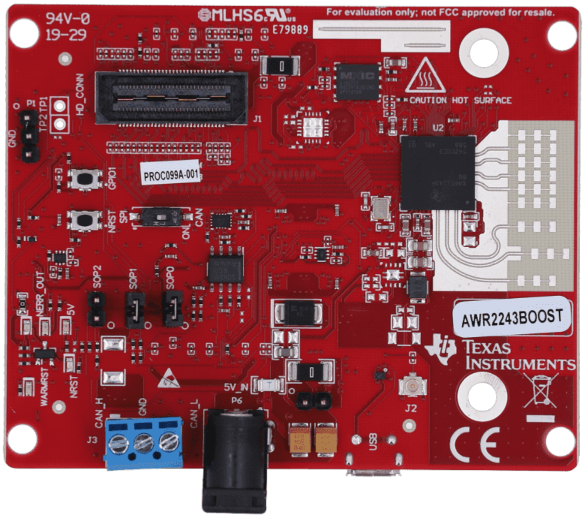

(a)

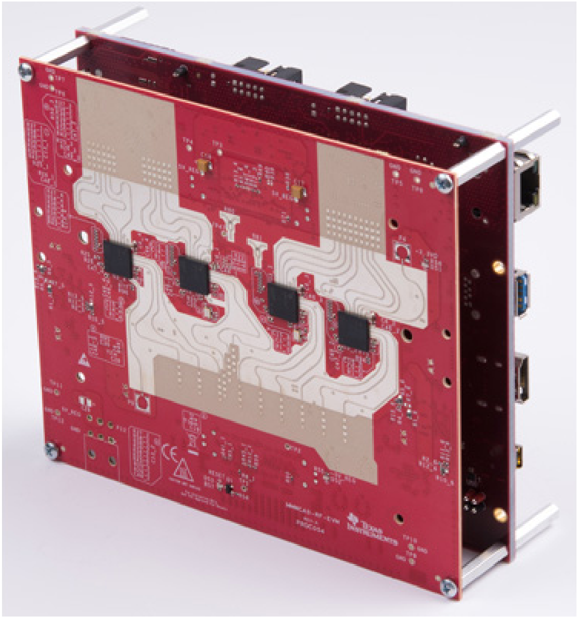

(b)

Figure 1.4: Texas Instrument imaging radar using cascaded MMW sensor AWR2243. (a) The BoosterPack evaluation board for the single-chip AWR2243 device. (b) AWR2243 four-device cascade radar with 16 receive and 12 transmit series-fed patch antennas embedded in the boards [35].

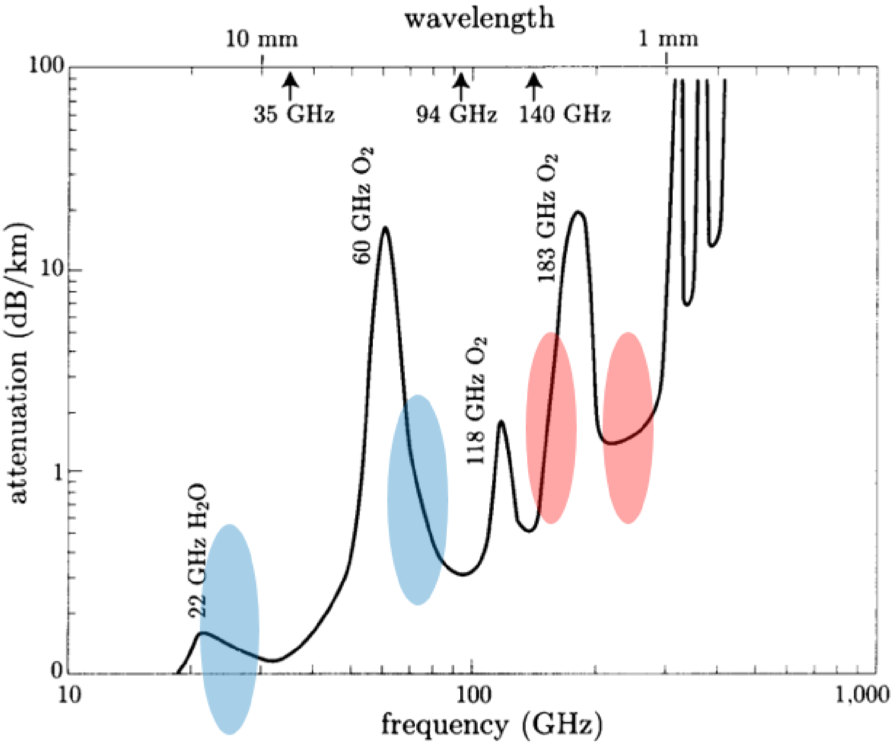

Figure 1.5: The spectrum of MMW band with the blue shades mark the current automotive radars bands, while red shades mark two of the proposed frequency bands with two distinct atmospheric windows [53].

frequency spectrum covering frequencies between 30 GHz and 300 GHz [54]. However a more specific frequency band nomenclature has been adopted by supplier of MMW components, where frequencies in the range 110 - 170 GHz are usually named D-band, while the range 220 - 325 GHz is usually refereed to as J-band. Recently, there have been significant advancements in solid-state and micromachining technologies that have made radar-based sensors operating at higher MMW frequencies economically viable [55, 56, 57, 58, 59, 60, 61]. Several applications have been proposed for radars operating at such frequencies including vehicle collision avoidance [62], robotic indoor navigation and mapping [63], assisted landing, and concealed object detection [64, 65, 66, 67, 68]. Although few phenomenological studies of radar backscatter from terrain have been reported in the open literature [63, 69, 70], none have considered the phenomenology of radar backscatter from targets at J-band in complex road environment. The backscatter responses of different objects in a road scene are expected to vary significantly as their physical properties, the look angle, and the transmit/receive radar polarization combination are varied [71, 72, 73, 74]. Examining the operation of such sensors in real circumstances and conducting phenomenological studies for specific applications is considered a vital input to take full advantage of these proposed frequencies. This research focuses on building the base knowledge for radars operating at J-band frequencies as proposed for automotive applications.

1.4 Phenomenology Studies

Beyond the standard functions such as detecting targets and measuring their distances and estimating their speeds based on the frequency Doppler shift, radars have other capabilities such as recognizing some targets based on previously known specified features, and in some cases determining other target features such as orientation and size. The knowledge required to phenomenologically examine and model common objects requires a thorough examination and modeling of these targets.

To start the study of the radar response of various objects in a road scene, a typical scene is observed by an instrumentation radar that operates at J-band, with a center frequency at 222 GHz. A typical scene is shown in Fig.1.6a along with a sketch to illustrate the scene and different objects in Fig.1.6b. The image is created using an instrumentation radar which has a 1^o effective antenna beamwidth and 2-GHz signal bandwidth at J-band. Figure.1.6c shows the radar image created from the scene. The resolution pixels are determined from the bandwidth along the propagation or range direction (7.5 cm range-resolution if no post-processing tapering is applied) and the effective beamwidth in the perpendicular or cross-range direction which is range dependent. This imaging mode is usually referred to as real-aperture mode. The image is created by mechanically scanning the radar beam in elevation and azimuth over the viewing road scene. The radar image clearly shows strong radar return from the vehicles in the scene compared to the radar returns that are distributed over most of the scene such as the road surfaces. In addition, the two stationary passenger vehicles in Fig.1.6 appear to have different radar signatures, considering the different shapes and sizes in addition to the difference in the look angle. It should be noted that a threshold is applied for clarity and therefore not all the dynamic range is actually color coded. The backscattering response of various surfaces, namely, the asphalt, concrete sidewalk, and short grass-covered surface, are also markedly different. The backscatter responses of the different constituents of the road scene are expected to vary significantly as their physical properties, the local incidence angle, and the transmit/receive radar polarization combination are varied. For example, early experimental research conducted at 94 GHz of different road surfaces have shown that the mean backscatter response at near grazing incidence is sensitive to the radar's polarization state, the local incidence angle, and physical properties of the road surfaces [71, 72, 73]. It was also demonstrated that an optimal transmit/receive polarization combination can be used to discriminate between different surfaces and under different weather conditions (wet, snow-covered, ice-covered) [74]. Other objects like traffic signs, trees, lighting poles, and pedestrians may also be present in the scene. In order for the radar to not only detect and locate all these kinds of targets, but also to identify the target category for various navigation purposes and to ensure the safety for all of the road participants, a very well characterized response of each target category is required. Such characterization can then be used to find certain unique features for the specific target that can be used for its identification. In the following sub-sections a discussion of the major categories that are examined and studied in this dissertation are discussed.

Phenomenology of Radar Backscatter Response from Vehicles

Vehicles are the most important targets in traffic scenes and not only must be identified, located, but also assessed for their other important parameters such as speed, orientation, and the space they occupied. There are no reported studies in the open literature on the nature of radar response of vehicles at J-band. Specifically, sources of radar scattering from vehicles, their location and strengths, as well as the statistical nature of the total radar return from vehicles have not been determined [75]. This effort addresses the aforementioned issues by reporting on a series of controlled polarimetric radar backscatter measurements at 222 GHz of a selected set of vehicles. As such, the reported results are of the "discovery" type and are by no means comprehensive. A combination of outdoor high-resolution synthetic aperture radar imaging experiments and real-aperture imaging measurements of vehicles are performed using a 222 GHz polarimetric instrumentation radar. The aim of these experiments is to examine the radar cross section (RCS) and its characteristics for different kinds of vehicles. That includes identifying the scattering phase-centers on different vehicle bodies, which are the fixture that are responsible for the strongest reflections and hence show brighter spots on the radar image of the vehicle.

Since the overall backscatter response is the coherent sum of many scatterings from the target vehicle body, a random-like fluctuation is observed. In addition, changes in the local

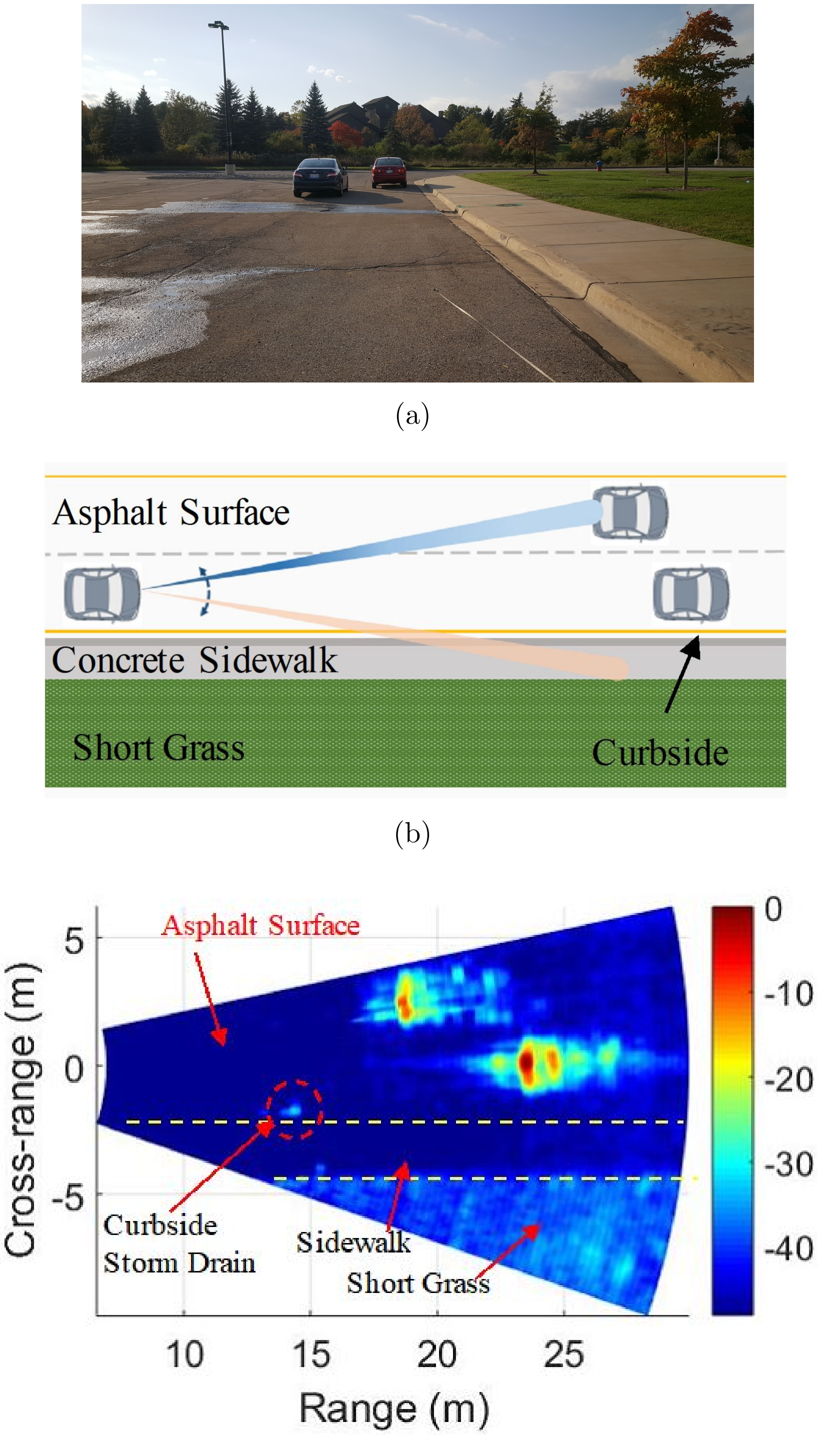

(a)

(b)

(c)

Figure 1.6: Radar backscatter response of a typical road scene measured at 222 GHz: (a) a photo taken for the scene from the radar viewing position (b) road scene illustration – top view and (b) real-aperture radar image of normalized RCS. Image is created by mechanically scanning the road scene using an instrumentation radar with 1^o effective antenna beamwidth and 2-GHz signal bandwidth (7.5 cm in range-resolution).

incidence angle θ_{az} results in fluctuations in the strength and phase of the backscattered fields from the different scattering phase centers on the vehicle. While the reflected radar signal from a vehicle may appear to be randomly fluctuating as the relative orientation angle of the vehicle is changed, the statistics of this signal is not random and it depends on the vehicle's physical and scattering properties. As a result, the statistics of the total backscattered response of the vehicle is important for detection and classification. The experimental results are used to determine the statistics of the vehicle's radar return.

The instrumentation radars used in this research, and the experimental setup are presented in Chapter II. Since isolating the sources of scattering from vehicles requires high-resolution capabilities in both range and cross-range, details on how the radar is used in short-range real-aperture imaging mode and how it is adapted for use in synthetic aperture radar (SAR) mode are presented in this chapter. Chapter III includes detailed description of the measurement approach, the measured data using both the real-aperture and SAR imaging modes are described with discussion of the radar scattering phase centers and sources of scattering of the selected vehicles. Finally, the statistics associated with scattering from vehicles along with the study methodology are presented with some other observations.

Radar Backscatter Responses from Road Surfaces

As previously stated, the optimum operation of radars necessitates a thorough understanding of responses of the objects encountered in the environment. A large portion of this research involves the characterization and modeling of various targets. As it was shown in Fig.1.6, a considerable radar signal is reflected by various distributed targets like concrete and asphalt surfaces and grass. Characterizing the radar response behavior of such surfaces in the road environment is the subject of another study. When a specific object is to be detected or observed, the signal reflected by these surfaces is sometimes considered background clutter. As a result, the expected level of radar signal from these surfaces is critical. Furthermore, the signals from these surfaces provide extremely useful information for safely navigating the road. The polarimetric response from road surfaces, particularly at near-grazing incidence angles (between 80 and 88^o), is examined. Asphalt in both new and weathered conditions, concrete, dirt roads, and short grass are among the surfaces investigated in this study. Some of these surfaces were measured in both dry and wet conditions, as well as when they were covered in snow or ice. Using the knowledge gained from this study, radar sensors would be able to map the road, identify its lanes and boundaries, and detect any changes in the way to avoid debris, defects, or slippery patches on the road.

Even though surfaces of the same type may have minor variations due to aging, weather conditions, or construction procedures, they rarely alter dramatically. Some of the physical characteristics that influence the response must be recognized, either through theoretical understanding or through comprehensive measurements. This will enable the development of a model that takes these variations into account and is thus relevant to all surfaces with similar physical features. Many studies on the use of radars in road assessment and recognition rely solely on the statistical and machine learning methods [76, 77, 78, 79, 80, 81]. Not only are these methods computationally intensive, but they also lack assurance, making decisions based on a single sensor unreliable. This research is conducted with the goal of developing a solid theoretical knowledge of radar backscattering from road surfaces, and developing a mean of numerical models for estimating the road responses to a high level of reliability.

Chapter IV is dedicated to the discussion of backscatter responses from road surfaces which begin with the theoretical principles of radar backscattering, which will be based on theories that was found to be the most accurate in describing the scattering at this frequency. Based on experimental data, both forms of scattering should be considered, volume and surface scatterings. In addition, Chapter IV includes reports on the experimental data of various measurements of polarimetric radar responses.

The Polarimetric Radar Backscatter Response of Human Bodies

Human safety as passengers or pedestrians has always been atop issue by car manufacturers and proponents of autonomous vehicles. Detection and identification of such subjects should be robust and could consist of multi-layer algorithms to ensure high level of reliability. In Chapter V, some of the detection techniques that will boost the reliability of radar identification of human subjects are discussed. The investigation in this chapter provides the first base of knowledge for some possible detection and identification algorithms of human subjects using J-band radars. The first straightforward method of detection is based on human RCS data. This method is discussed along with its shortcomings and how it could narrow the possibilities of the target estimation, resulting in a considerable identification accuracy. In addition, the use of radar polarimetry is discussed and experimental results are presented. Unlike point targets where the scattering mechanism is deterministic, physically complex and large targets have rather complicated scattering phenomenon which suggests a statistical approach in identification. A full statistical study based on set of measurements is presented in Chapter V.

Another distinct feature of humans as regards to radar detection is the measurements of micro-Doppler spectrum of the radar return for a walking human subject. Many studies at lower MMW frequencies have shown that moving pedestrians can be identified very accurately using their mciro-Doppler signatures. This feature is also investigated at 230 GHz. Based on many measurements that were performed on vehicles, only single Doppler component is usually observed. On the contrary, Doppler measurements of a moving person show many Doppler components due to different speeds of body parts, particularly the limbs. The Doppler spectrum of a moving body can be used by automotive radars to recognize pedestrians from other objects of comparable radar cross section. In the second half of Chapter V, many measurements of a moving person at different speeds are reported and discussed.

At the end of the dissertation, the conclusion and recommended feature works are outlined in Chapter VI.

CHAPTER II

Description of J-Band Instrumentation Radar Systems

This section describes two polarimetric instrumentation radars that were used in conducting studies in Chapters III through V. The experimental setups, challenges, and limitations are discussed for each system and for various operation modes. In addition, the utilization of the two radars to perform real-aperture and synthetic aperture radar imaging, Doppler measurements, and mechanical scanning are described.

2.1 VNA- Based J-Band Instrumentation Radar

The first of two radars used to conduct this research is fully-polarimetric Vector Network Analyzer (VNA) based radar. It operates at a center frequency of 222 GHz with bandwidth of 2 GHz. Fig.2.1 shows the block-diagram of the RF-frontend of the radar. The radar operates in a stepped-frequency mode, whereby the VNA steps over equally-spaced set of frequency points spanning the desired radar bandwidth. At each step, the VNA generates a continuous-wave signal at the corresponding intermediate frequency (IF). Then, the IF signal is up-converted, transmitted, received, and down-converted by the RF frontend section of the radar and then returned back to the VNA for coherent detection. The total transmitted power is on order of -13.5 dBm. The overall noise figure of the receiver is about 6 dB and the dynamic range is more than 100 dB. The transmit and receive antennas are Gaussian

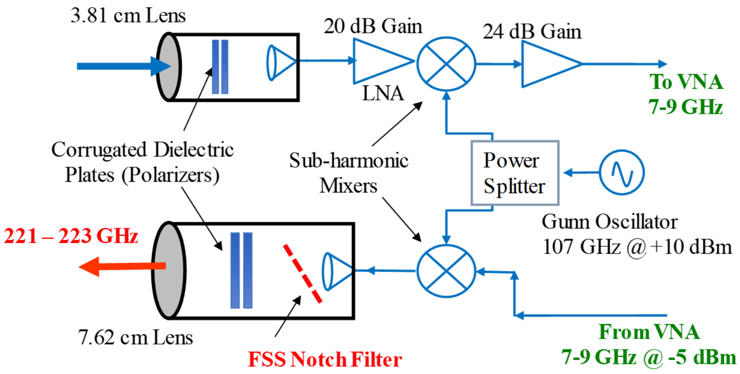

Figure 2.1: Block-diagram of the 222 GHz fully-polarimetric VNA-based instrumentation radar.

optic lens antennas of diameters 7.6-cm and 3.8-cm and their beamwidths are 1.1° and 2°, respectively. The effective real-aperture cross-range (angular) resolution of this radar is 1°. The polarization of each antenna is established using two cascaded quarter-wave corrugated dielectric plates inserted between the lens and the feed horn. The dielectric plates are rotated together to generate Horizontal (H) or Vertical (V) polarizations [82]. Polarization isolation of this radar is on the order of 25-dB. Table.3.1 summarizes the main specifications of the instrumentation radar. A more detailed description of the radar design, hardware characteristics, and calibration procedure can be found in [70].

2.1.1 Real-Aperture Imaging Setup and Processing

In real-aperture imaging mode, the radar's narrow beam is used to scan the target area and create a radar image. While range-resolution in this case is determined by the bandwidth of the radar signal and is independent of the distance to the target, the cross-range resolution on the other hand is dependent on both the effective antenna beamwidths in elevation and azimuth and on the distance to the target.

To operate the 222 GHz instrumentation radar in real-aperture imaging mode, the radar was mounted on a precise, computer-controlled turntable to enable scanning of the radar

Table 2.1: List of Main Specifications of The 222 GHz Instrumentation Radar.

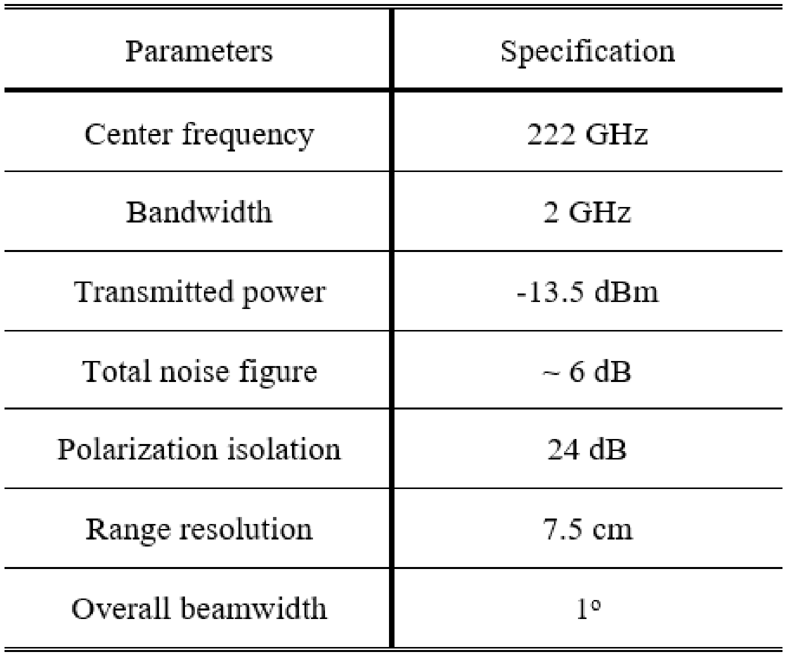

Parameters	Specification
Center frequency	222 GHz
Bandwidth	2 GHz
Transmitted power	-13.5 dBm
Total noise figure	~ 6 dB
Polarization isolation	24 dB
Range resolution	7.5 cm
Overall beamwidth	1°

scene with angular accuracy better than 0.1° and over wide angular range spanning ±90° in azimuth. At a standoff range of 10 m, this setup results in a radar spot diameter of 18 cm based on the 1° overall radar's antenna beamwidth which defines the resolution in both elevation and azimuth directions, and in a 7.5 cm resolution in range by employing the 2 GHz bandwidth. The hardware setup and scanning mechanism are illustrated in Fig.2.2. Example for the result of such imaging was presented in Section. 1.4. During measurements, the radar is rotated horizontally to scan the scene and measurements are taken at 0.5° steps. Then, the elevation angle is adjusted manually if another height sector of the target to be imaged. To images vehicles, radar responses of 13 to 14 different elevation angles and 25 azimuth angles are collected to generate real-aperture image of the whole vehicle. The collected data is then processed and combined to generate a 3D map of the vehicle. The radar returns might be calibrated using a calibration target with a known radar cross section (RCS), usually a 2-inch metallic sphere, to obtain scattering maps of extended targets.

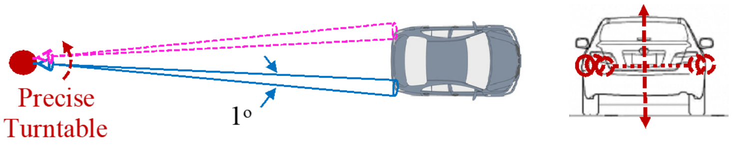

Figure 2.2: Illustration for the setup of a radar mechanically scanning its narrow beam in 2-D to generate a 3-D scattering cloud of the vehicle.

2.1.2 Synthetic-Aperture Radar Imaging Setup and Processing

As stated in the previous section, the 222 GHz instrumentation radar has an effective beamwidth of 1°. Note that the minimum distance allowed between the radar and any target is 10 m. This minimum distance is set by the far-field criterion for radar's antennas. At a distance of 10 m, the effective radar spot size is on the order of 18 cm in diameter, which is much higher than the desired cross-range resolution for radar imaging. For example, at most 5 cm resolution is needed to isolate different scattering phase-centers on vehicles. It can be shown that in order to achieve a 3-cm in cross-range resolution at 10 m distance using a real-aperture radar, the required antenna beamwidth is 0.17°, which translates to having a prohibitively large antenna size of 0.45 m (this can be calculated using the following relation $l_h = \lambda/\beta_h$, with l_h , β_h , and λ referring to the antenna's physical width, its beamwidth, and the radar's wavelength, respectively). Alternatively, high cross-range resolution on the order of 3-cm can be achieved using synthetic aperture radar (SAR). In this approach, a radar with small size antenna is placed on a linear stage and measurements of the target are repeated as the radar is moved along the stage at equal increments. The data is then processed using the back-projection technique [83] to create the desired cross-range resolution.

It can be demonstrated that the best cross-range resolution is achieved when the length of synthetic aperture is set equal to the antenna's spot width at the target's range [83]. In this case, the cross-range resolution is on the order of $D/2$, where D is the width of the actual radar antenna. The resulting radar images are referred to as fully-focused SAR images. To achieve a fully focused SAR image at every point on a target, the length of the synthetic aperture must exceed the width of the target. For example, to perform SAR image of a vehicle and since the typical width of a full-size passenger car is about 2 m, then a linear stage of at least 2 m in length is needed to enable a fully focused SAR image of a vehicle. A 2 m long linear stage with movement precision on the order of few micrometers is prohibitively expensive equipment. An alternative approach is pursued based on the fact that a SAR image with high cross-range resolution can be achieved using a smaller linear stage on the condition that the entire width of the vehicle is illuminated by the radar at every point of the smaller synthetic aperture. This can be accomplished by reducing the widths of the actual antenna apertures in the instrumentation radar which results in wider antenna beamwidths. In this case, the processed SAR image will not have the cross-range resolution that a fully focused SAR will produce; however, with proper selection of the distance to the vehicle, the desired cross-range resolution can still be attained.

To widen the azimuth beamwidth of the instrumentation radar while keeping the beamwidth in elevation at its original value of 1°, and without major changes performed to the radar, the two antenna lenses were partially blocked using copper tape except for a vertical slot as can be seen in the inset photograph of Fig.2.3. With the slots' width set to 6.4 mm, the radar's effective beamwidth in azimuth was measured at 6.5° as shown in the radiation pattern in Fig.2.3. Since the length of the slot is equal to the lens original diameter, the altered lenses retained the same beamwidths in elevation, which were verified experimentally to be 1.1° for the transmit antenna and 2° for the receive antenna. It should be noted that the reduction in gain caused by blocking most of the lens is compensated for by the SAR processing gain (i.e. combining many measurements coherently).

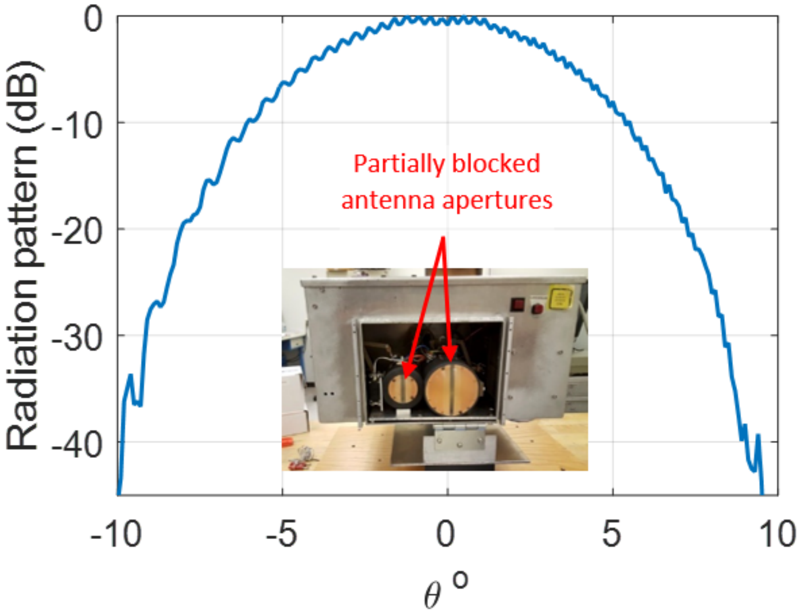

Figure 2.3: The radiation pattern of the partially blocked antennas in order to increase the Beamwidth. Embedded is a photo of the radar shows the antenna.

2.1.3 Measurement Procedure and Indoor Verification of SAR Imaging Mode:

During the SAR imaging measurements, the radar was moved along a linear track perpendicular to the direction of propagation and polarimetric data were taken at prescribed positions along the track. These measurements were then processed to generate the image [83]. The radar was installed on a precise linear stage 80-cm in length, with movement accuracy of about 5 μm. It should be noted that any deviation from the positions at which measurements were taken will generate an error in the phase corresponding to the deviation measured in wavelengths. Since the wavelength at 222 GHz is 1.35 mm, even very small vibrations will cause considerable error in the phase-angle of the measured radar signals at different SAR antenna positions. These un-corrected random phase-angle errors render proper focusing of the SAR data a challenging task. It was observed that small vibrations that normally are not noticed by humans, such as the vibrations in the building due to operating machines and air-conditioning, can affect the SAR imaging results at 222 GHz. To reduce this effect

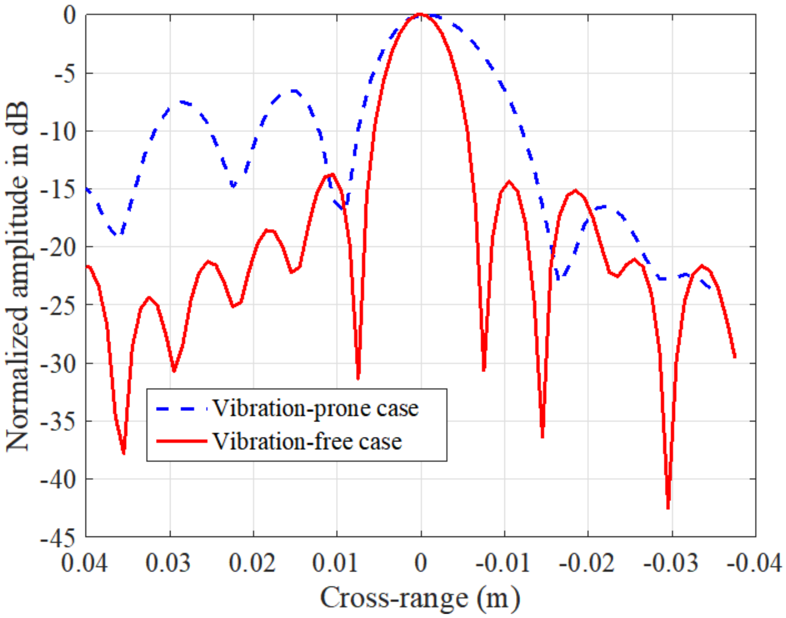

Figure 2.4: Two Cross-range responses of a point target to illustrate the effect of vibration in on the processed SAR data.

during indoor testing of the system, both the platform holding the linear stage and radar, and the point target under test were placed on shock-absorbing structures; hence decoupling the experimental setup from the rest of the building. To illustrate the effect of vibrations, Fig.2.4 shows the cross-range response of a single trihedral being distorted due to vibrations and the response for the same target after the decoupling process. In the vibration-prone case, cross-range response of the target is poorly focused with energy leaking into the side-lobes and creating fake targets, while in the vibration-free case, the cross-range response is in very good agreement with the expected theoretical cross-range response of a point target.

The 2-D resolution of a SAR image is determined by both the range resolution which is the dimension along the propagation direction and the cross-range resolution which is the orthogonal dimension. The former is set by the radar signal bandwidth which is 2 GHz, resulting in 7.5-cm in range resolution, and the latter is determined mainly by the length of the synthetic aperture and the range to the target. An experiment was performed using four small corner reflectors as targets to verify the resolution capabilities of the SAR system. The

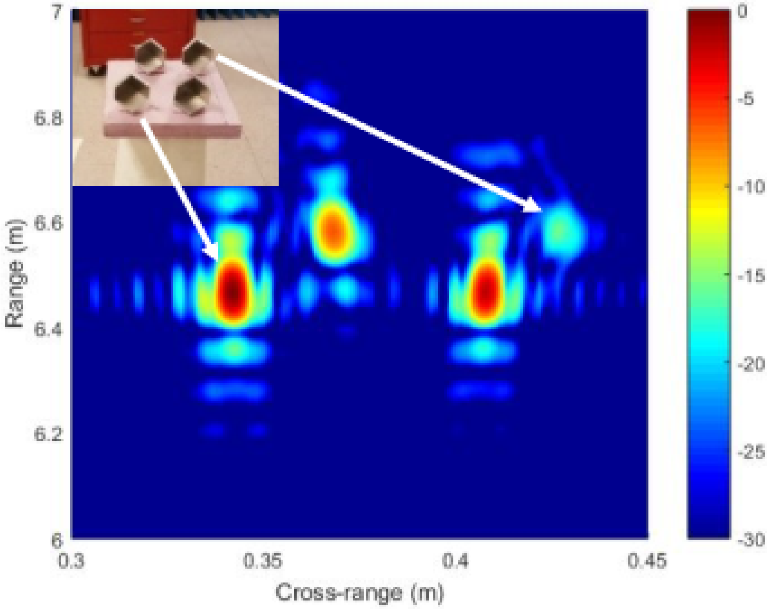

Figure 2.5: Processed SAR image of four closely packed corner reflectors measured indoors at 222 GHz. Inset is a photographic picture of the targets.

corner reflectors were 2.5 cm in size and placed close to each other in the arrangement shown in the inset photo in Fig.2.5. The separation between the two reflectors in each row is 6.5 cm and the two rows are separated by 11 cm. The reflectors and the radar were placed at the same height above ground. As a result, substantial shadowing was casted by the reflectors in the front row on those in the back row. Nevertheless, the radar responses of all targets were captured in the processed SAR image of Fig.2.5 albeit with the reflectors in the back row having weaker responses. The image in 2.5 demonstrates the ability of the radar system to create high resolution SAR images of closely packed targets, both in range and cross-range. The cross-resolution achieved indoors was better than 1 cm at a distance 10-m away from the radar.

2.2 Frequency-Modulated Continuous-Wave J-Band Radar System

Another system that was built to support this work was a polarimetric frequency-modulated contentious-wave (FMCW) radar. This instrument provides very fast measurements that allow reliable phase coherence of consecutive measurements, hence very suitable for fully-polarimetric scattering matrix and Doppler measurements. In addition, the FMCW system has two receivers dedicated to each orthogonal polarization. The received vertical and horizontal polarizations are separated using a wire grid that ensures high isolation. Instead of the up-conversion mixers in the transmitter that was employed in the first system, a series of frequency active multipliers are used in the current instrument, which permits the generation of higher transmit power of about 5 dBm. Also, the switching between polarizations in the transmitter is performed through an electronic RF single pole double throw (SPDT) switch rather than the mechanical switches in the VNA-based system. Electronic switching enables fast polarization shifting between consecutive chirps (sweeps). Therefore two chirps are sufficient to measure the full scattering matrix of a target in as short as 40 μsec. The switching is performed at an intermediate frequency (around 75 GHz) between two active multiplication stages. The FMCW signal is generated at S-band using a customized phase-locked loop (PLL) circuit. Moreover, the detection is performed using an available commercialized sampling circuit that has up to 500 MHz sampling frequency. The block diagram of the instrument is displayed in Fig.2.6.

The system's operating frequency is from 221.4 to 228 GHz (up to 6.6 GHz bandwidth). The FMCW waveform is generated anywhere over the range from 3.150 to 3.700 GHz using a programmable direct digital synthesizer (DDS) and a PLL circuit with sweeping times between 10 μs to 10 ms. This provides flexibility in the design of the FMCW chirps for different purposes and modes. Two Gaussian optics lens antennas are utilized for transmitting and receiving in a mono-static configuration, as shown in Fig.2.6. Each antenna has

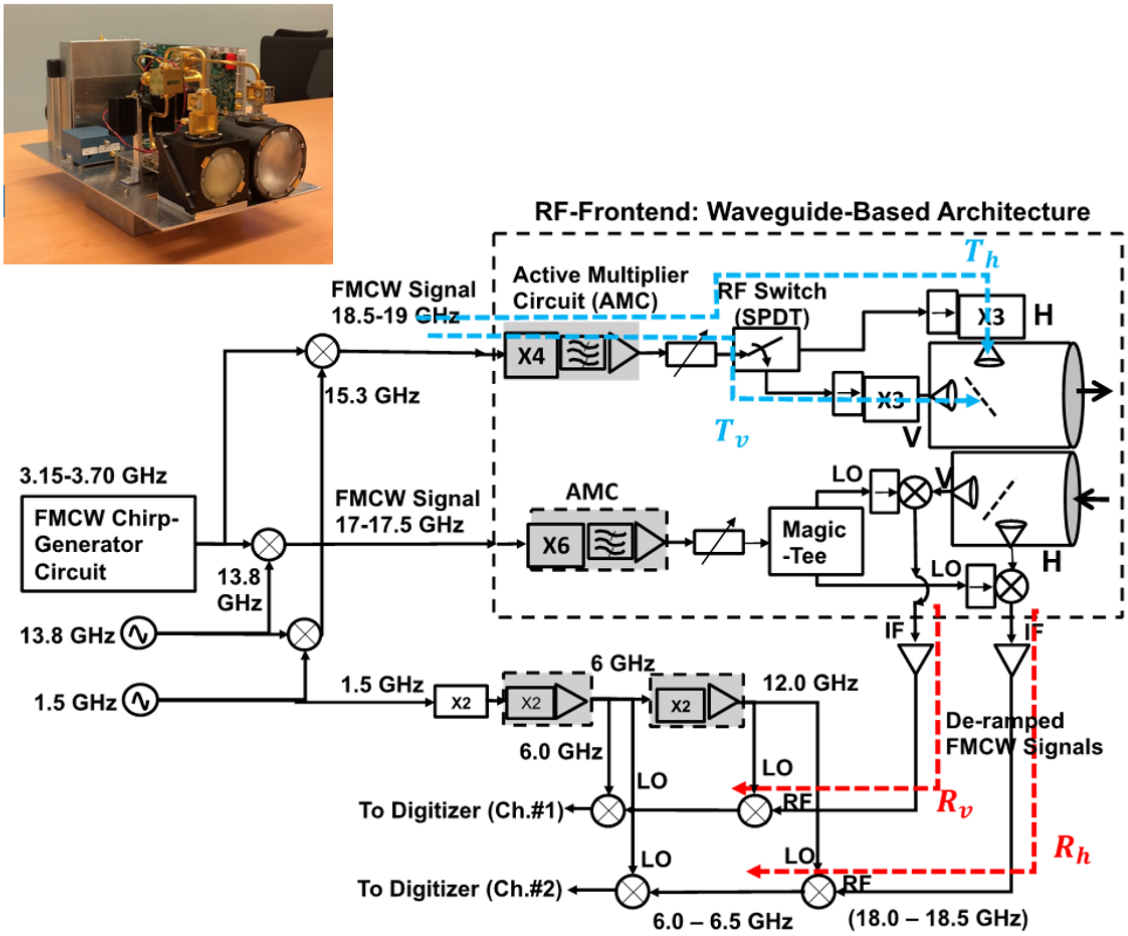

Figure 2.6: Block diagram of the J-band FMCW polarimetric instrumentation radar. A photo taken for the radar without its housing cover is included.

Table 2.2: Technical Specifications of the FMCW J-Band Instrumentation Radar.

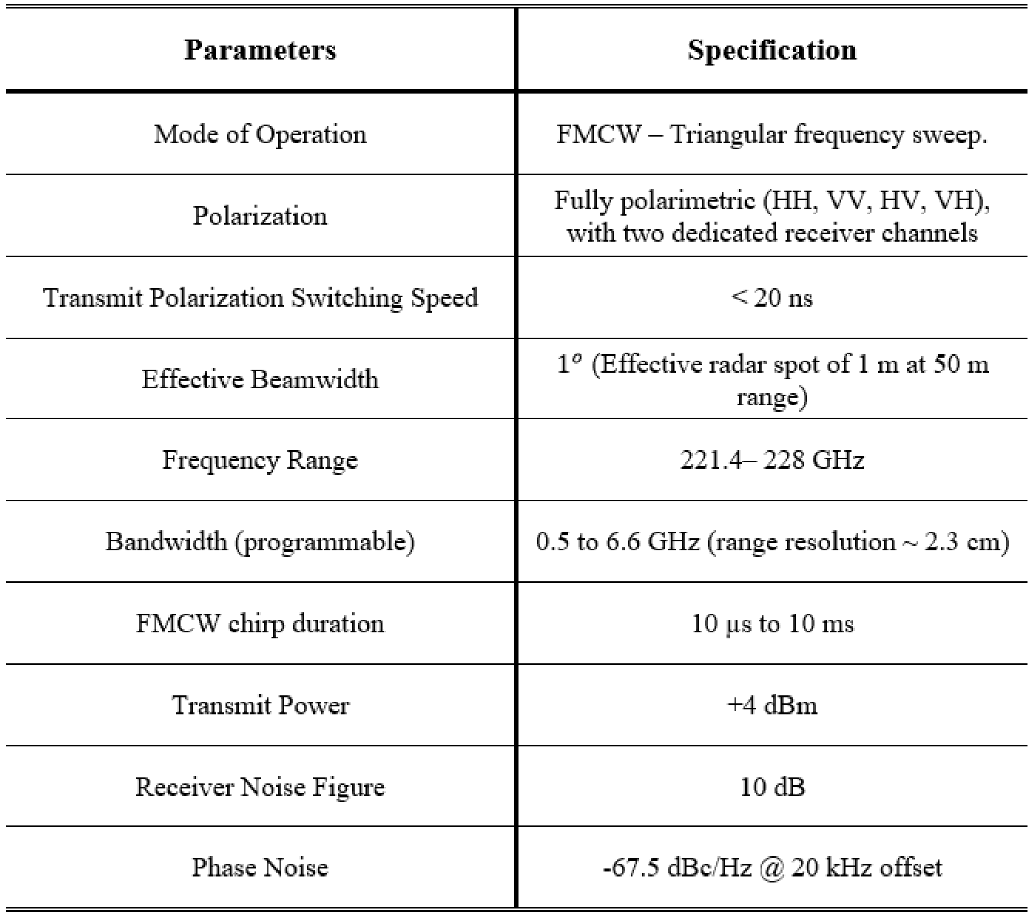

Parameters	Specification
Mode of Operation	FMCW – Triangular frequency sweep.
Polarization	Fully polarimetric (HH, VV, HV, VH), with two dedicated receiver channels
Transmit Polarization Switching Speed	< 20 ns
Effective Beamwidth	1° (Effective radar spot of 1 m at 50 m range)
Frequency Range	221.4– 228 GHz
Bandwidth (programmable)	0.5 to 6.6 GHz (range resolution ~ 2.3 cm)
FMCW chirp duration	10 μs to 10 ms
Transmit Power	+4 dBm
Receiver Noise Figure	10 dB
Phase Noise	-67.5 dBc/Hz @ 20 kHz offset

dual corrugated feed horns for V- and H-polarization channels. The two polarizations are separated using a wire grid in each antenna system with 40-dB polarization isolation. The transmit antenna has a 3-inch lens with 1.2° 3-dB beamwidth and 42.3 dBi gain, and the receive antenna has a 2-inch lens with 1.6° in beamwidth and 38.5 dBi gain. Overall, the effective system beamwidth is 1°. Some technical specifications of the radar are listed in Table.2.2, and the reader is referred to [84] for more details regarding the system.

2.2.1 High-Resolution 360° Imaging of Traffic Scenes

The J-band radar was used to demonstrate the feasibility of performing continuous high-resolution imaging of a vehicle's surroundings, as depicted in Fig.2.7a. The instrumentation system was configured as shown in Fig. 2.7b and placed on a flatbed truck for actual complex traffic scenes imaging. In this configuration, the instrumentation radar was placed vertically while its antennas were illuminating a 45° tilted metallic flat plate. The titled plate acts as a mirror at J-band frequencies and is connected to a motor to enable its continuous rotation around the motor's axis. The result is a continuously rotating radar beam in azimuth. The motor is equipped with a digital encoder to read the instantaneous look angle of the radar. The radar was set to transmit continuous FMCW chirps with 500 MHz bandwidth and chirp time duration of $T_{chirp} = 102\mu sec$. The mirror was rotated at 240 RPM (4 revolutions/s). Hence, at the end of each data collection (chirp duration) the mirror would have moved 0.15° in azimuth.

The radar was used to image a large parking lot on the University of Michigan campus. The location and size of all objects were documented during the measurement, including a large building next to the lot, fences, trees, parked cars, and trailers. The radar returns from multiple 360° mirror rotations at multiple positions along a straight path are collected. Figure.2.8 shows all objects plotted on a scene map with reflections received at each radar position color-coded. It is observed that the radar was able to detect all objects in the radar scene, including vehicles, trailers, trees, the building, light poles, and metallic fences, except for those shadowed by other large objects in the signal path. In addition, some reflections were detected at locations where no vehicles or objects were present. These ghost targets can be attributed to multiple reflections between trailers and vehicles. Moreover, certain vehicles were obscured by other vehicles in front of them, hence, there was no return from these vehicles.

In another experiment, the radar remained fixed while individual vehicles were driven in the scene, as depicted in Fig.2.9. One car was driven away from the radar at 25 mile/hr

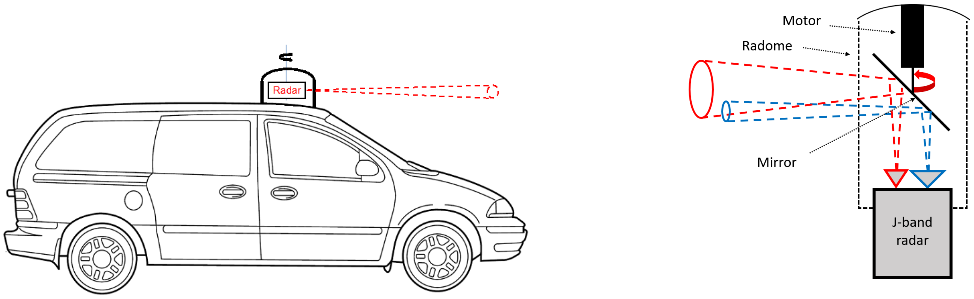

(a) (b)

Figure 2.7: Envisioned use of compact FMCW radar at J-band for continuous imaging of the surrounding of an autonomous vehicle (a) placement on vehicle and (b) configuration using the current instrumentation radar.

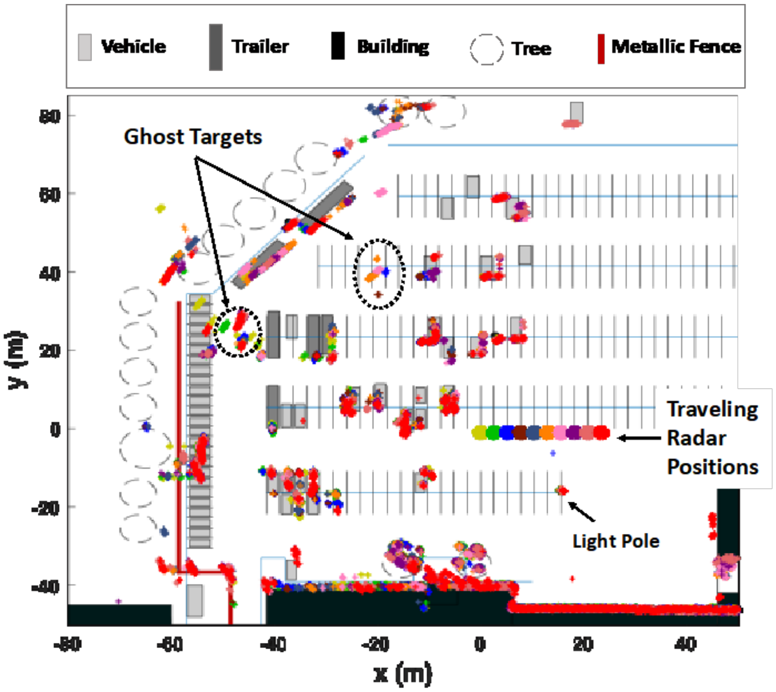

Figure 2.8: Azimuth imaging of the parking lot where all objects are stationary and the radar is moved along a straight line. Radar reflections are shown due to finite set of discrete radar positions. Each radar position has its own color to facilitate distinction of the different radar reflections.

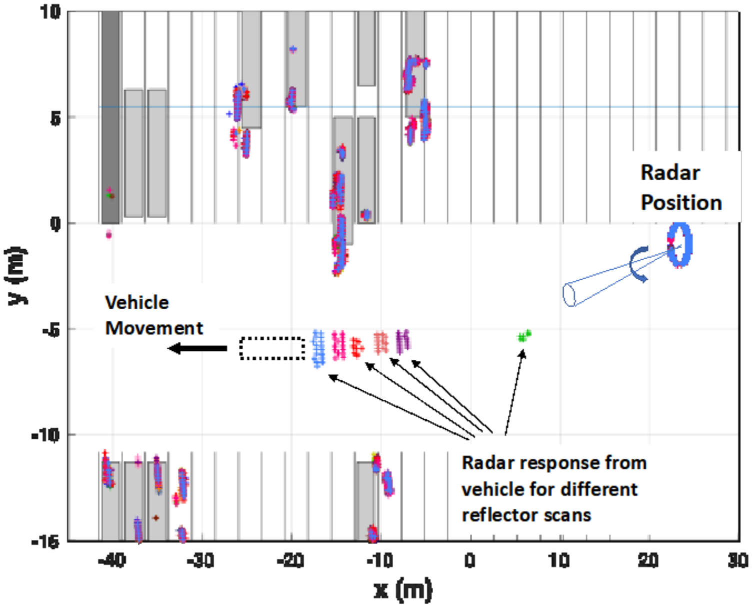

Figure 2.9: Azimuth imaging of the parking lot where a vehicle is moving at 25 mile/hr away from the J-band radar placed at a fixed position. Radar reflections that correspond to a single mirror rotation have the same distinct color.

speed. Since the radar beam is narrow in elevation, the car was not detected until a specific distance after it passed the radar. In Fig.2.9, radar reflections of various mirror rotations were given distinct colors. It can be observed that reflections are from many spots on the vehicle, and the response spreads as it moves further. This spread is due to the increasing spot size with distance.

CHAPTER III

Experimental Characterization of Multi-Polarization Radar Backscatter Response of Vehicles at J -Band

3.1 Introduction

There are no reported studies in open literature on the nature of radar response of vehicles at J-band. Specifically, sources of radar scattering from vehicles, their location and strengths, as well as the statistical nature of the total radar return from vehicles have not been determined. This chapter addresses the aforementioned issues by reporting on a series of controlled polarimetric radar backscatter measurements at 222 GHz of a selected set of vehicles. As such, the reported results are of the "discovery" type and are by no means comprehensive. A detailed description of the measurement approach and the experimental setup is provided in Section 2 of this chapter. Since isolating the sources of scattering from vehicles requires high-resolution capabilities in both range and cross-range, vehicles were imaged using short-range real-aperture imaging mode and synthetic aperture radar (SAR) mode to identify their scattering phase-centers. The measured data using both the real-aperture and SAR imaging modes are presented in Section 3.3. The section also includes a discussion of the radar scattering phase-centers and sources of scattering of the selected vehicles. The statistics associated with scattering from vehicles and other observations are presented in

Section 3.4.

3.2 Measurement Approach and Experimental Setup

Isolating the scattering phase-centers on vehicles requires having a sensor with high range and cross-range resolutions. It is expected that the bulk of the radar return will be from the outer surfaces of the vehicle, primarily surfaces that are facing the automotive radar. In typical automotive radar operation, the primary scattering surfaces are the back of the vehicle (outgoing traffic) and the front of the vehicle (incoming, or opposite traffic). There are many fixtures on these surfaces that may contribute to the radar backscatter, such as the taillights, bumper, hood edges, license plate and its mount, front-lights, traffic signals, Grill, etc. The radar return from these fixtures is function of their material composition, electrical sizes, position, and orientation relative to the radar's line-of-sight. It has been decided in this paper that measuring the radar backscatter response of the vehicle with resolution that is better than $10cm \times 5cm$ in range and azimuth resolutions, respectively, is sufficient to isolate the scattering phase-centers on the vehicle. The instrument used in this study in the VNA-based J-band radar introduced in Section 2.1. This system was used for imaging vehicles in real-aperture more as described in Section 2.1.1. In addition, SAR mode was used to create images with finer cross-range resolution.

For Outdoor SAR measurements the 222 GHz instrumentation radar was placed atop the 80 cm long precise linear stage, which was in turn installed inside a test vehicle for protection against direct sun and wind, as shown in Fig.3.1b. The test vehicle was mounted on fixed jacks above ground and the radar's height above ground was set to 20 cm above the vehicle's bumper. This height mimics the height above ground chosen by car manufacturers to install the 77-GHz collision warning radars on present-day vehicles. To ensure that the entire car is illuminated by the radar beam of 6.5° beamwidth as the radar is moved across the synthetic aperture (which is determined by the length of the linear stage of 80 cm), the imaged vehicle had to be placed 27 m away from the radar.

Radar measurements were collected along the linear stage at equally spaced points with spacing equal to $2\lambda \approxeq 2.7$ mm. In effect, 297 radar measurements of the target scene were collected and used to generate each SAR image. Corner reflectors were placed on both sides of the vehicle at a slightly closer range to ensure that the radar is pointed at the vehicle and that the center of the vehicle is aligned with the center of the linear stage. It should be noted that the resolution in elevation is based on the elevational beamwidth of the radar, which is about 45 cm at the distance to the vehicle. In addition, the resolution in azimuth is based on the length of the synthetic aperture which translates to 3 cm in cross-range resolution at the target's range. Moreover, the resolution in range is based on the 2 GHz in radar signal bandwith which translates to 7.5 cm in range resolution. Hence, the resolution cells in the created 2-D SAR image are 3 cm × 7.5 cm in size. However, each cell stores the response of a volume who's dimensions are 3 cm × 7.5 cm × 45 cm. Measurements in SAR imaging mode had to be performed at 3 to 4 different height cuts in order to examine the entire vehicle. The experimental setup used for outdoor SAR measurements at 222 GHz is depicted in Fig.3.1.

3.3 Radar Scattering Phase-Centers on Vehicles

The instrumentation radar was used outdoors to image stationary vehicles while operating in real-aperture and in SAR imaging modes. Four different target vehicles are used in this study. Table.**??** lists the vehicles used along with their overall dimensions.

3.3.1 High Azimuth Resolution Images of Vehicles

Two-dimensional (2-D) high-resolution images of the target vehicles were generated using the SAR measurement technique described in the previous section. At the measurement stand-off range of 27 m, the image resolution was on the order of 7.5 cm in range and

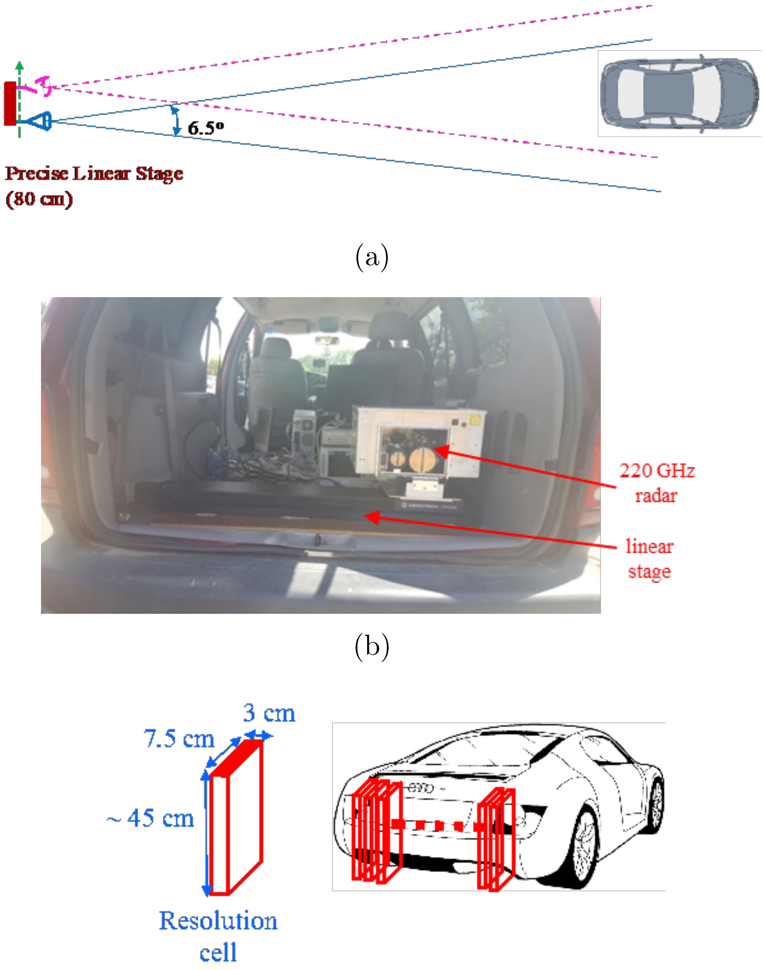

(a)

(b)

(c)

Figure 3.1: Outdoor SAR measurement setup (a) top-view of experimental setup and target scene, (b) photographic picture of the radar installed atop a precise linear stage 20 cm above the vehicle's bumper inside a mini-van, and (c) equivalent resolution cells of the SAR image.

Table 3.1: List of Target Vehicles Used in the Experimental Studies along with their Overall Dimensions.

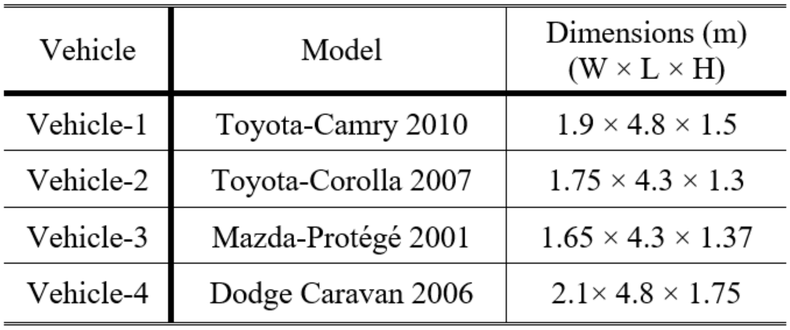

Vehicle	Model	Dimensions (m) (W × L × H)
Vehicle-1	Toyota-Camry 2010	1.9 × 4.8 × 1.5
Vehicle-2	Toyota-Corolla 2007	1.75 × 4.3 × 1.3
Vehicle-3	Mazda-Protégé 2001	1.65 × 4.3 × 1.37
Vehicle-4	Dodge Caravan 2006	2.1× 4.8 × 1.75

3-cm in cross-range (azimuth). The HH-polarized SAR images of Vehicle-1 at three different elevation cuts are shown in Fig.3.2. These images provide accurately the location, in azimuth and in range, of the scattering phase-centers on the vehicle at different elevational cuts. It is observed that no significant scattering occurs from inside the passenger cabin of the vehicle. This can be attributed to the fact that no direct signal path exists between the radar and major structures in the vehicle's interior, such as the steering wheel, the dashboard, and the front-row seats, due to the low height placement of the radar compared to the vehicle's windows. Contrary to conventional wisdom that strong and sustained scattering over wide angular ranges is expected from tail lights that act as corner reflectors, the actual strongest returns came from the back of the vehicle, primarily from the trunk and bumper areas as evident from the images in Fig.3.2. For this particular vehicle, other scattering phase-centers occur at the two exhaust outlets, along the back of the vehicle, and other corners of the vehicle. Since the strongest scattering is the specular reflection from the flat area around the license plate, then strong dependence on the look angle is expected which will be further examined in the next section.

The SAR images of Vehicle-2 are reported in Fig.3.3 and Fig.3.4 for HH- and VH- polarizations responses, respectively. The images show that the scattering phase-centers are due to fixtures similar to those found in Vehicle-1. In addition, a strong backscatter response is observed coming from underneath Vehicle-2. This can be clearly observed in the SAR image of the bottom cut (see Fig.3.3(b)) about 1-m into the vehicle behind the scattering phase-centers of the bumper/trunk region. The source of this strong backscatter response is the rear-axle of Vehicle-2. In this configuration, the radar signal bounces off the asphalt surface near or underneath the vehicle, backscatters from the rear-axle structure, and once again bounces off the asphalt surface and back to the radar. Since this specular reflection off of the asphalt surface occurs at near-grazing incidence, with the magnitude of surface reflection coefficient approaching unity, the reflected signal remains coherent and strong backscatter response from the axle is observed. Scattering from the bottom of the vehicle is stronger in the case of Vehicle-2 compared to Vehicle-1 because of the larger bumper height from the ground in the former and therefore the more exposure to the radar signal. Another experiment was performed to image the front of a vehicle is shown in Fig.3.5. The image shows major scattering due to the headlights, the Grill area, and the front bumper of the vehicle. The asymmetry in the image, where the scattering from the headlight on one side is weaker than the other side by about 7 dB, can be attributed to the small angular error in aligning the vehicle with respect to the radar. This observation emphasizes the need for statistical-based target detection, since the radar return is sensitive to the relative orientation angles between the radar and the target vehicle, as well as other factors such as the area of the target vehicle that is illuminated by the radar. The study of the statistical behavior of the backscatter response of vehicles at 222 GHz is deferred to the following section.

3.3.2 Real Aperture Imaging of Vehicles

The generation of the SAR images of vehicles in the previous section has enabled the detection and isolation of different scattering phase-centers along both range and cross-range (azimuth) dimensions to within 7.5 cm and 3 cm, respectively. However, the actual positions of the scattering phase-centers in elevation are significantly lacking in accuracy due to the coarse elevation resolution afforded by the measurement system (about 45 cm along

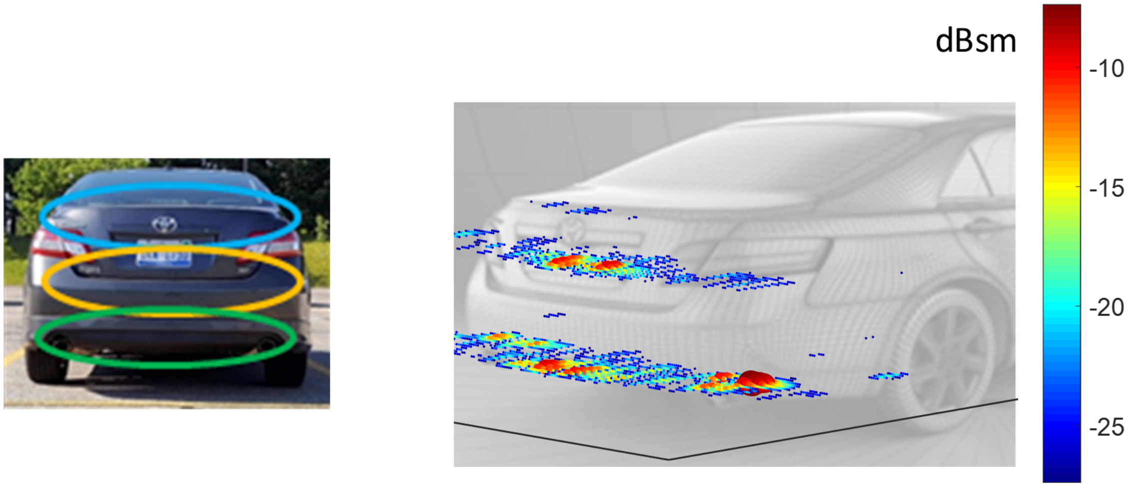

(a)

(b)

Figure 3.2: Processed SAR images of Vehicle-1 measured at HH-polarization: (a) photograph of the measured side of the vehicle (backside) with illustration of the three different elevation cuts, (b) SAR image of the three cuts represented by cloud of dots that are centered at each cut (sizes of dots are proportional to strength of reflection to give the figure more readability).

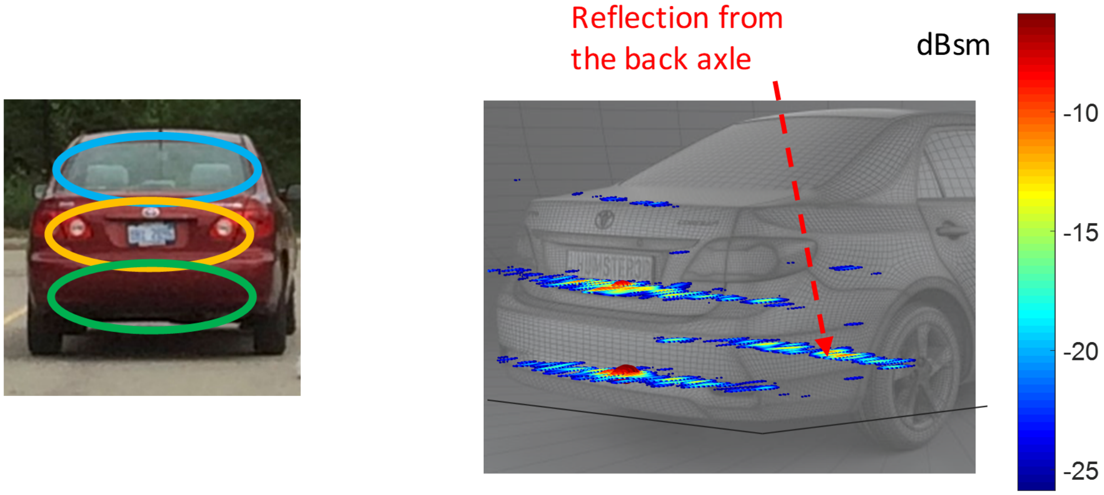

(a)

(b)

Figure 3.3: Processed SAR images of Vehicle-2 measured at HH-polarization: (a) photograph of the measured side of the vehicle (backside) with illustration of the three different elevation cuts, (b) SAR image of the three cuts represented by cloud of dots that are centered at each cut (sizes of dots are proportional to strength of reflection to give the figure more readability).

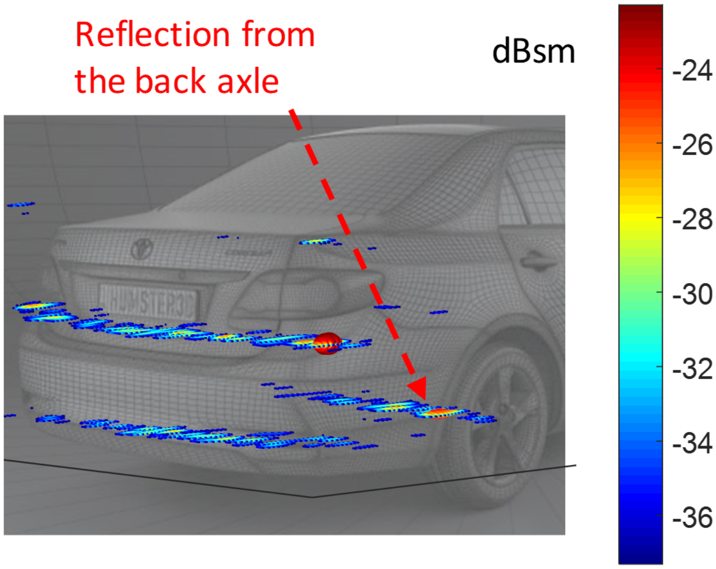

Figure 3.4: Processed SAR images of Vehicle-2 measured at VH-polarization.

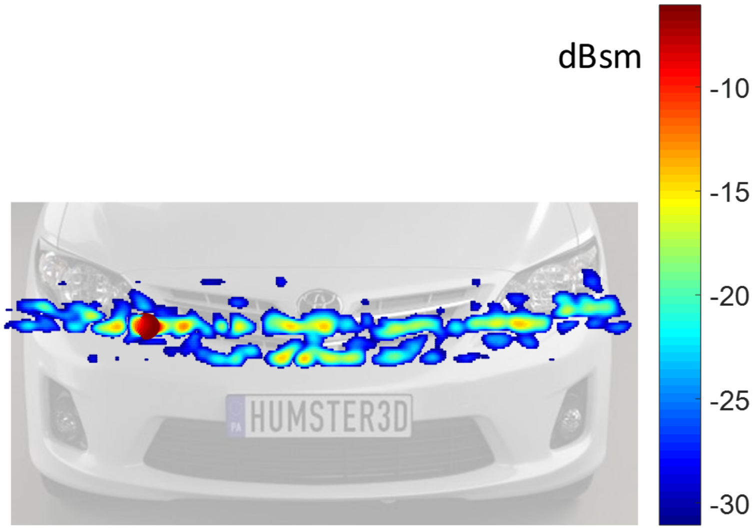

Figure 3.5: Processed SAR image of the front of Vehicle-2 measured at HH-polarization.

the elevation direction). To achieve high resolution in both azimuth and elevation, SAR measurements over 2-D grid of spatial radar positions would be needed, which requires an expensive infrastructure and is time consuming. The alternative approach is to perform the real-aperture imaging of the target vehicle at a shorter range to ensure that a small radar-spot size is illuminating the different parts of the test vehicle. In real-aperture mode, the resolution is proportional directly to the range to the target. However, there is a minimum range that should be maintained to allow the transmit and receive antenna beams to overlap. This minimum range is about 10-m for the 222 GHz instrumentation radar at hand. With the radar placed at 10-m from the target vehicle, the radar resolution is $18cm \times 18cm$ in both azimuth and elevation. As discussed in Section 2.1.1, the target vehicle can be 2-D scanned in real-aperture mode at 0.5° angular increments. A 2-D measurement grid of 25 azimuth angles and 14 elevation angles is needed to complete the measurements. From these measurements, a 3-D map of scattering centers on the target vehicle is generated. The position of each scattering center is calculated using radar's height above ground, the target's range (derived from actual signal round-trip time), and the azimuth and elevation angles of the radar. The 3-D position is resolved within 7.5 cm in range, and 18 cm in cross-range (both elevation and azimuth directions). Operating in real-aperture imaging mode results in a small size data set and shorter measurement time when compared to operating in SAR imaging mode. The real-aperture imaging mode is also less sensitive to errors in phase due to vibration or radar location compared to the SAR imaging mode.

Figure.3.6 shows the HH-polarized 3-D real-aperture maps of scattering phase-centers of Vehicle-1 overlaid on a computer-aided design (CAD) model of the vehicle. The data are projected onto the top, side, and back views of the vehicle with the strength of the backscattered response represented in terms of both the scaled color and the size of its corresponding dot. The radar data in the 3-D maps have been calibrated against the response of a 2-inch metallic sphere that is measured at the same range. It is evident from Fig.3.6 that –similar to what was observed in the SAR images- the strongest return comes from the back of the vehicle; primarily from the trunk and bumper area. Similar scattering strengths of the SAR images are observed here, but with more accurate determination of the source of scattering in elevation. For example, radar backscatter responses of the exhaust outlets were isolated from the backscatter response of the bumper (was not possible to isolate in elevation when the SAR imaging mode was used). This of course is achieved at the expense of degraded azimuth resolution (18 cm for real-aperture as opposed to 3 cm for SAR imaging mode). Another observation worth noting is the backscatter response occurring from the bottom of the vehicle as shown in Fig.3.6(d). These radar returns appear only when the real-aperture radar (with 18 cm radar spot size) was pointed at the asphalt surface before or underneath the vehicle's bumper. These radar returns disappear when the vehicle is removed, suggesting that the cause of these radar returns is not deep within the asphalt surface (skin depth of asphalt is on the order of fraction of millimeter at 222 GHz), rather it is due to the radar signal bouncing off of the asphalt surface and reflecting from the bottom structures of the vehicle. This confirms the similar observations noted earlier in the SAR images.

The resulting map for the same vehicle, Vehicle-1, measured using VH-polarization is shown in Fig.3.7. It is observed that different major scattering phase-centers are observed for the cross-polarized returns when compared to the co-polarized case. For example, the strongest depolarization in Vehicle-1 is due to the two exhaust outlets with depolarization of about -9 dB. The scattering maps for Vehicles-2, -3, and -4, are reported in Fig.3.8 through Fig.3.10, respectively, for both HH- and VH-polarizations. It can be concluded from these figures that a major reflection always comes from the trunk and around the license plate areas, but many different weaker reflections are observed due to other fixtures on the vehicles. On the other hand, the results reveal distinct contrast between cross-polarization signatures of the different vehicles.

Another test was performed to observe the impact of the radar look angle on the strength and distribution of the scattering phase-centers. In this experiment, the angle between the

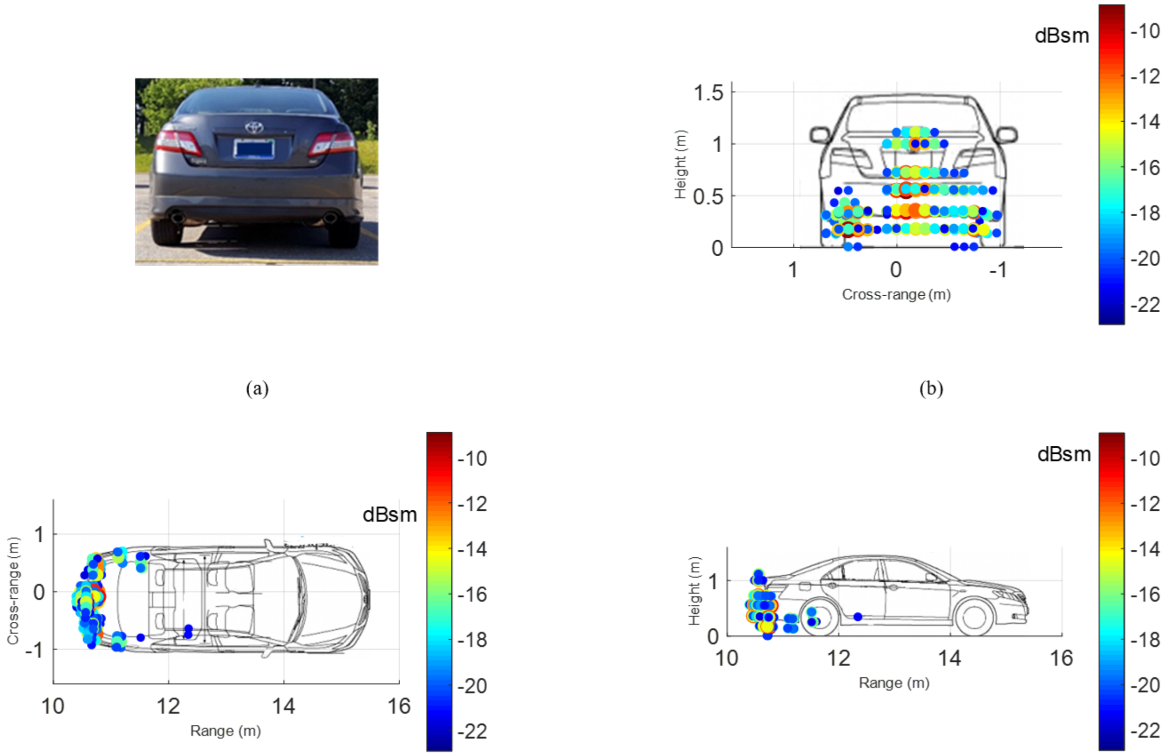

(a)

(b)

(c)

(d)

Figure 3.6: The scattering map of Vehicle-1 at HH-polarization (a) photo of the vehicle, (b) back view (c) top view, and (d) side view.

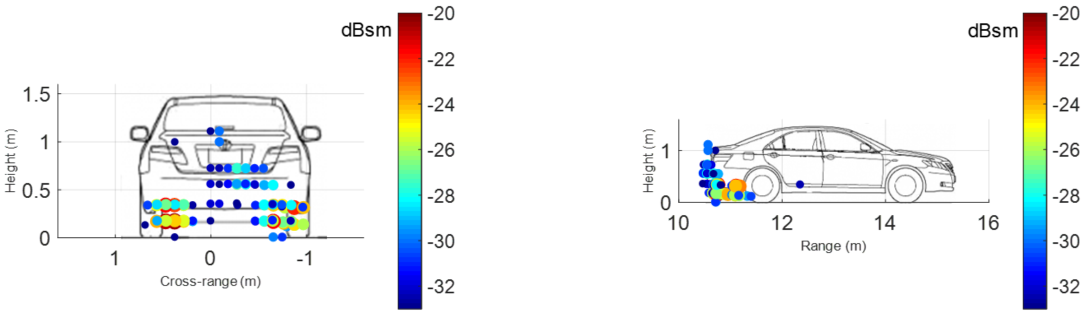

(a)

(b)

Figure 3.7: The scattering map of Vehicle-1 at VH-polarization (a) back view, and (b) side view.

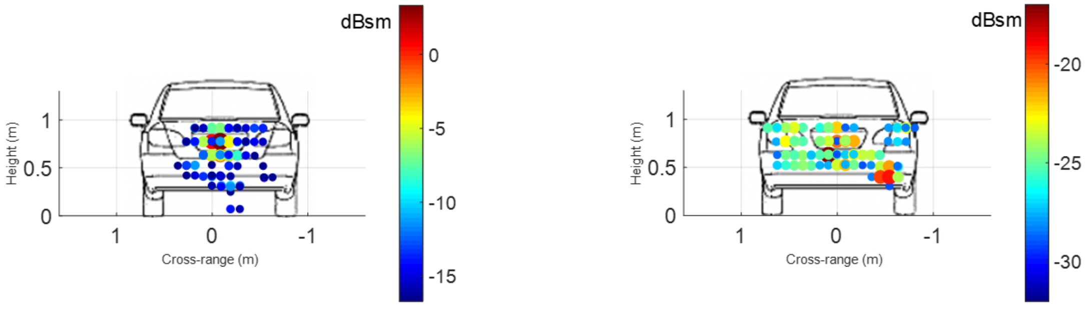

(a) (b)

Figure 3.8: The scattering map of Vehicle-2 at (a) HH-polarization, and (b) VH-polarization.

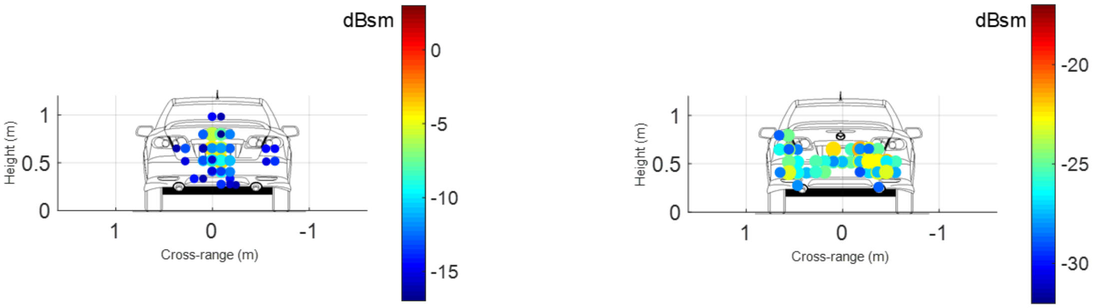

(a) (b)

Figure 3.9: The scattering map of Vehicle-3 at (a) HH-polarization, and (b) VH-polarization.

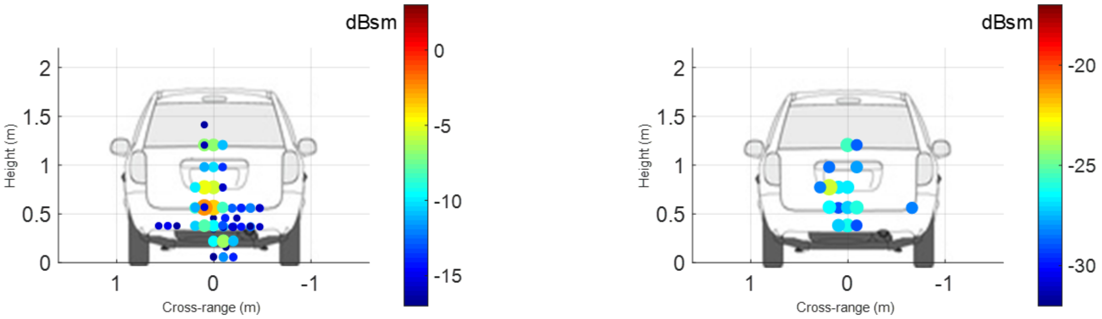

(a) (b)

Figure 3.10: The scattering map of Vehicle-4 (a) HH-polarization, and (b) VH-polarization.

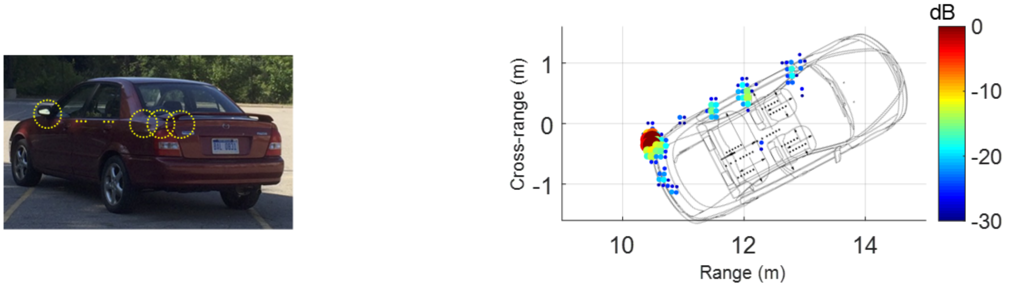

(a)

(b)

Figure 3.11: The scattering centers on Vehicle-3 when the vehicle is oriented at 30° relative to the radar (a) photo of the vehicle with signs on the scattering centers, (b) the scattering map measured using HH-polarization.

radar look direction in azimuth and the normal to the back of target Vehicle-3 was set to 30° as shown in Fig.3.11. The resulting real-aperture radar map in Fig.3.11 shows completely different scattering centers as a result of changing the vehicle orientation with respect to the radar when compared to the data for the same vehicle measured at 0° look angle (shown in Fig.3.9). The dominant scattering center when the look angle was set to 0° was at the license plate area (as shown in Fig.3.9). However, the scattering phase center moved to the corner of the vehicle when the look angle was set to 30° (as shown in Fig.3.11). In addition, radar returns from other parts of the vehicle such as the side mirror and door-handles were observed when the look angle was set to 30° that would have been shadowed by the back of the vehicles otherwise. It is expected that vehicles in different lanes or at different orientations to present different scattering centers depending on the look angle.

3.4 Statistics of Radar Backscattering Response of Vehicles

The high-resolution SAR images of vehicles that were reported in the previous section (e.g. Fig.3.2) indicate the presence of scattering phase-centers with strong radar backscatter responses. These centers are located primarily on the outer surface of the vehicle. The strength of the backscatter response of a given scattering phase-center depends on its dimensions, shape, material composition, and the relative orientation angle between fixtures comprising this scattering phase-center and the radar's line-of-sight direction. The large dimensions of some of these fixtures compared to the signal wavelength at 222 GHz (1.35 mm) makes their backscatter response strongly-dependent on the local incidence angle. The high-resolution images also reveal that in addition to the few scattering phase-centers with strong backscatter response, there are many more scattering phase-centers with weak backscatter response. In a realistic traffic scene scenario, whereby a real-aperture radar is used to scan the traffic scene, the received radar signal at any instant of time is the coherent sum of the scattered fields from all scattering phase-centers (both weak and strong) on the vehicle that have been illuminated by the radar. The radar cross-section at a given range-bin, σ, can be expressed as

$$\begin{aligned} \sigma\left(\theta_{az}\right) &= 4\pi\left|s_{total}\left(\theta_{az}\right)\right|^2 \\ &= 4\pi\left|\sum\nolimits_m s_m\left(\theta_{az}\right)e^{j2k_o\widehat{k_i}\left(\theta_{az}\right)\cdot\overline{r_m}}\right|^2 \end{aligned} \tag{1}$$

here s_m is the strength of the scattered field from the m-th scattering phase-center, $\overline{r_m}$ is a vector representing the location of the center, $\widehat{k_i}$ is a unit vector describing the direction of propagation of the radar signal, k_o is the propagation constant, and θ_{az} is the angle in azimuth between $\widehat{k_i}$ and the normal to the vehicle's surface $\hat{n}$. It is expected that for any given target vehicle, the radar backscatter response will fluctuate randomly as the relative orientation angle (θ_{az}) between the target vehicle and the radar's line-of-sight is varied. A cartoon sketch of phase-centers on the back of a vehicle being illuminated by a plane wave is shown in Fig.3.12. Changes in the local incidence angle θ_{az} results in fluctuations in the strength of the radar backscattered fields from the different scattering phase-centers ($s_m\left(\theta_{az}\right)$) as well as changes in the phase angles of the scattered fields from the different phase-centers due

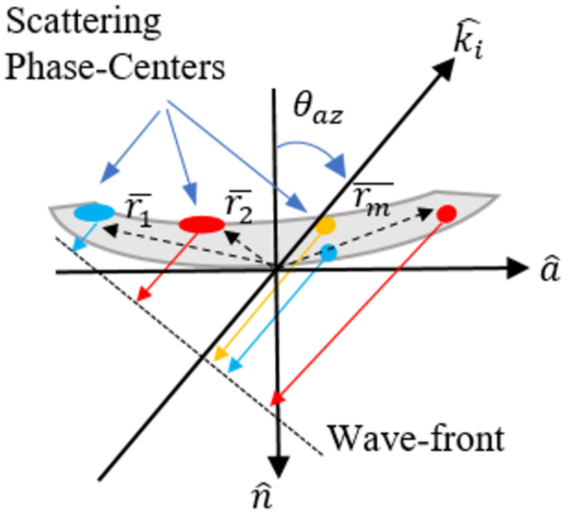

Figure 3.12: Cartoon sketch of scattering phase-centers randomly located on the back of a vehicle being illuminated by an incident plane wave at a relative angle θ_{az} from normal incidence (different colors represent different scattering strengths levels).

to changes in the relative distances between the radar and the phase-centers. While the reflected radar signal from a vehicle may appear to be randomly fluctuating as the relative orientation angle of the vehicle is changed, the statistics of this signal are not random and they depend on the vehicle's physical and scattering properties. As a result, the statistics of the total backscattered response of the vehicle is important for detection and classification.

In this study, the radar backscatter statistics of target vehicles is examined for two distinct traffic scenarios: 1- fully illuminated vehicle, and 2- partially-illuminated vehicle as depicted in Fig.3.13. In the fully-illuminated scenario, the entire vehicle is enclosed by the radar beam. Typically, this is the case when the radar is operating at mid to long-range from the vehicle. In the partially-illuminated scenario, the radar beam is only illuminating a small portion of the vehicle, which is the case when the distance between the radar and the vehicle is small. In this case, only few scattering phase-centers may contribute to the radar backscatter response.

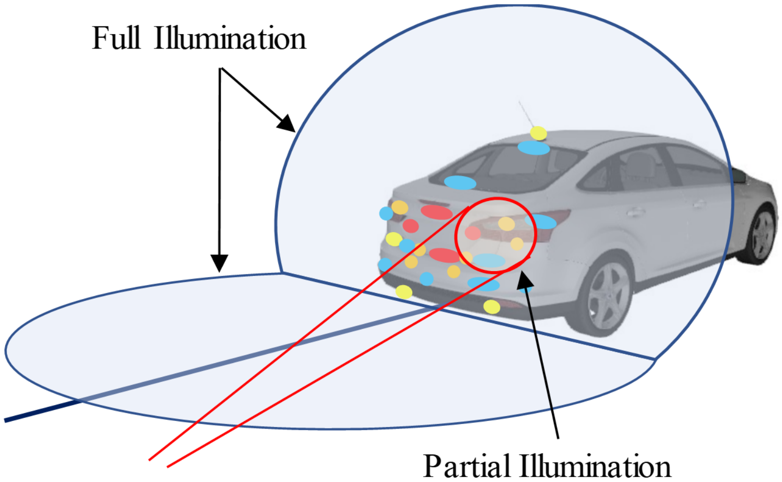

Figure 3.13: Selected road scene scenarios: fully-illuminated and partially-illuminated target vehicle by the radar's antenna beam. Scattering phase-centers are displayed as colored dots. Their color and placement in this figure are just to illustrate the concept and do not reflect an actual measurement.

3.4.1 Commonly Used Statistical RCS Models

Commonly used probability density functions (PDF) for describing RCS fluctuations include the Exponential, Rician, Lognormal, Weibull, Chi-square, and the K-distribution PDFs [85]. The exponential PDF has been used successfully to model the RCS statistics of random, uniformly distributed clutter, such as road surfaces, grass fields, snow, etc. [86]. For this type of clutter, the radar return is due to scattering from a large number of scatterers with comparable scattering strength but with random locations. When the amplitude of the scattered field (as opposed to its power) is detected for the same ensemble of randomly located scatterers, the resulting statistics follow the Rayleigh PDF. Historically, these scatterers have been referred to as Rayleigh scatterers [87]. The other PDFs (e.g. Rician, Weibull, and K-distribution) have been used to model the RCS statistics of complex targets. These targets consist of a constant dominant scatterer and a collection of weak Rayleigh scatterers. Sea echo statistics as well as some land clutter have been modeled using these PDFs [85, 86, 87]. In the case of scattering from vehicles, it was shown in previous section that major specular reflections are observed (which are very sensitive to the relative look angle) and other weaker, yet considerable reflections, are present too. Therefore, the aforementioned PDFs have been considered in this investigation for modeling the RCS statistics of the measured vehicles. Of particular interest is the Weibull and K-distribution, as they have shown to provide best fits to data.

The PDF of Weibull distribution is given by:

$$f\left(x;\beta,\lambda\right)=\frac{\beta}{\lambda}\left(\frac{x}{\lambda}\right)^{\beta-1}e^{-\left(\frac{x}{\lambda}\right)^{\beta}}\quad x\geq 0 \tag{2}$$

where β is the shape parameter and λ is a scaling factor. The exponential distribution is a special case of the Weibull distribution when β=1. It has been reported that for many types of clutter, best fit between the Weibull distribution and measured data occurs for β ranging between 0.3 and 1.0 [85]. Figure.3.14 shows a plot of Weibull PDF function for three different values of β.

As mentioned earlier, the K-distribution has been used for a long time to represent the statistics of radar scattering from ocean waves and other random medias [88, 89]. The PDF of K-distribution has close resemblance to Weibull distribution but it requires more involved computations. The PDF of K-distribution is given by

$$g\left(x;\alpha,\lambda\right)=\frac{4}{\sqrt{\lambda}\Gamma\left(\alpha\right)}\left(\frac{x}{\sqrt{\lambda}}\right)^{\alpha}K_{\alpha-1}\left(\frac{2x}{\sqrt{\lambda}}\right)\quad x\geq 0, \tag{3}$$

where α is the shape parameter, λ is some scaling factor, $\Gamma(\cdot)$ is the gamma function and $K_{\alpha-1}(\cdot)$ is the modified Bessel function of the second kind and the $(\alpha-1)$th order. In order to identify the PDF that best fits the data, the Kolmogorov-Smirnov (KS) test is used to measure the goodness-of-fit. The KS test is a measure of the distance between the Empirical Cumulative Density Function (ECDF) of the measured data and the Cumulative Density Function (CDF) of the proposed PDF with best fitting parameters [90]. To find the best fitting parameters, the maximum likelihood estimation is used. The PDF with smallest KS

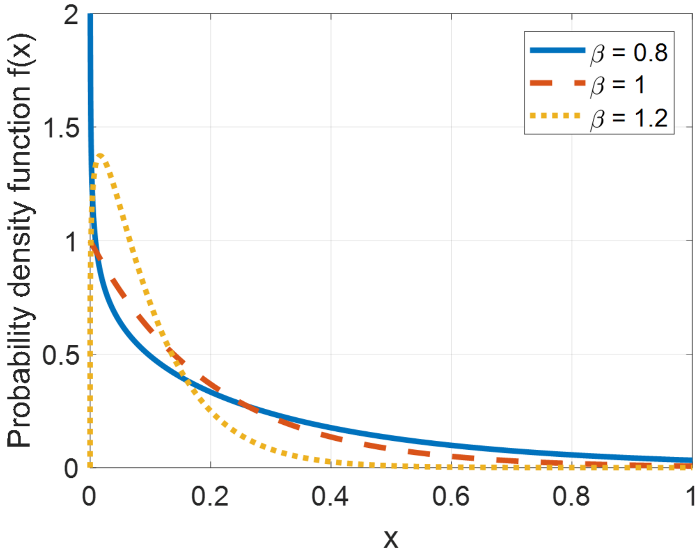

Figure 3.14: The PDF function of Weibull distribution for three different values of β.

statistic is considered as the best fitting PDF [91].

3.4.2 Statistical Model of Fully-illuminated Vehicles

As mentioned before, the instrumentation radar illuminated the entire vehicle all the time as it was translated over the linear stage during the SAR measurements. This resulted in a large data set of fully-illuminated vehicles that can be used to extract the PDF. Here, the data is re-purposed (no SAR image formation is performed on the data) and used as real-aperture data. The collected data at each position are treated as independent samples and the PDF is calculated after isolating the response of the vehicle from other signals using an appropriate software range-gating. The aspect angle of all measurements is small and is within $\pm 1^\circ$. As was shown in Section 3.3, the back of the vehicle is responsible for the observed strong return. It was also shown that other significant response that is delayed in range can be attributed to signals reflecting from underneath the car (axle) after bouncing off by the road surface. This response alters in strength form vehicle to vehicle and may not show up in the measured response. This reflection is expected to impact the statistical response and therefore in order to study the effect of this reflection, the statistics for different height levels of the vehicle are treated separately. Fig.3.15 shows a comparison between the ECDF of the measured RCS with the standard fitted CDF functions for K-, Weibull, and Lognormal distributions. The used data is for the middle height cut of Vehicle-2 at HH-polarization (see Fig.3.3). The CDFs for both K- and Weibull distributions provide good fit for the data. However, it was found for other data sets that the fluctuations in RCS data follow the Lognormal or Exponential distributions more closely. The comparison between how well do these PDF functions match the measured data is performed by calculating the KS statistic for every proposed PDF that is found to have similar shape to the measured data. The computed KS values for the Weibull, K-, and Lognormal distributions in Fig.3.15 are 0.03104, 0.03159, and 0.03669, respectively, where the value $KS = 0$ corresponds to a perfect fit. A complete study of the goodness-of-fit for the Gamma, Weibull, K-, Lognormal and Exponential distributions has been conducted on the available measurement data. The results show that Weibull provides better fit as the scattering from underneath the vehicle increases (in the bottom cut measurements). It should also be noted that the best fit for the measured data using the Weibull distribution is obtained when β is in the range $0.89 \sim 0.99$ as listed in Table.3.2. On the other hand, the best fit of the K-distribution to the measured data is when α is in the range $0.45 \sim 0.51$. In conclusion, even though other distributions seem to provide good fit in some cases, Weibull distribution provides more robust fit for different cuts of the vehicle and with less sensitivity to the source of the backscattering.

3.4.3 Statistical Model of Partially-illuminated Vehicles

A narrow beam scanning radar operating at close range from a vehicle will illuminate a portion of the vehicle at any instant of time, as depicted in Fig.3.13. As a result, the vehicle's radar response will be observed over a wide angular scan in azimuth. Furthermore, it is expected that the statistics of the measured signals over wide variation of the aspect angle will no longer be dominated by the specular reflections off of the vehicle surface, and therefore

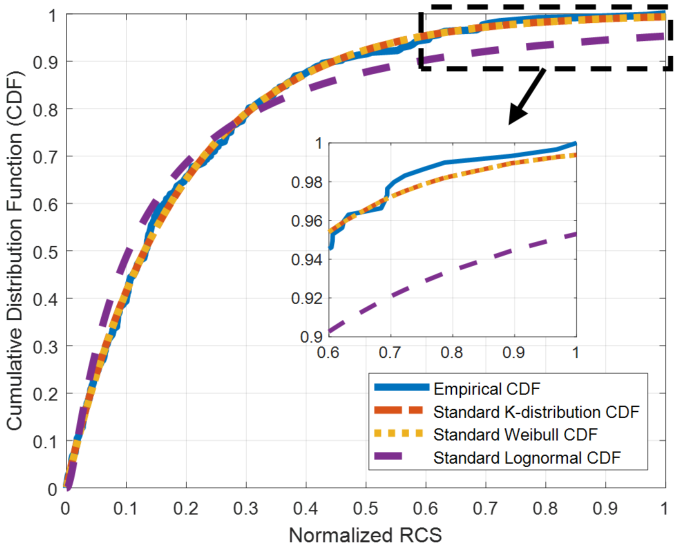

Figure 3.15: Comparison between the ECDF of the measured RCS with the standard CDF functions for different distributions.

Table 3.2: The shape parameter β for the best fit of Weibull PDF to the measured data (fully illuminated vehicle).

Vehicle	β	
	Bottom cut	Middle cut
Vehicle-1	0.986	0.924
Vehicle-2 (cpol)	0.943	0.976
Vehicle-2 (xpol)	0.887	0.956

different RCS statistics are expected. The real-aperture data reported in Section 3.3.2, are used to generate the RCS statistics. Upon comparing the ECDF of the measured RCS of partially-illuminated vehicles with the CDFs of the Gamma, Weibull, K-, and Lognormal distributions using the KS statistic, it was determined that the Weibull distribution provides the best fit to the measured data. In addition, this best fit was achieved at β values between 0.31 and 0.36 in co-polarization case and between 0.39 and 0.5 in the cross-polarization case as listed in Table.3.3.

It can be concluded that the statistics of the RCS of both the fully-illuminated and the partially-illuminated vehicles can be characterized as being Weibull-distributed, albeit with significantly different values of the shape parameter β.

As expressed in (1), the total received radar signal is the coherent sum of the scattered fields from all scattering phase-centers illuminated by the radar. It is expected that as the illuminated area of the vehicle is increased, more scattering phase-centers will contribute to the total radar response and as the number of phase-centers becomes large (e.g. case of fully-illuminated vehicle), the statistics of the RCS will approach that of the Exponential distribution (or equivalently the Weibull distribution with β set to 1). This observation suggests that the statistics of RCS, for cases where the illuminated area of the vehicle is larger than 18 cm × 18 cm, can be derived from the statistics of the partially-illuminated case, which was shown to follow the Weibull distribution with $\beta\ approx 0.3$. Let the RCS of a wide-area illuminated vehicle be $\widetilde{F_w}$. Then, $\widetilde{F_w}$ can be expressed as

$$\widetilde{F_w} = \left| \sum_{m=1}^{M} \sqrt{\widetilde{F_p}(m)} e^{j\widetilde{\phi}(m)} \right|^2 \tag{4}$$

where $\widetilde{F_p}$ is the RCS of the partially-illuminated case (Weibull distributed with $\beta \approx 0.3$), $\widetilde{\phi}$ is uniformly distributed random phase, M is the number of partially-illuminated areas A_p within the total illuminated area A_w (i.e. $M = A_w/A_p$). To test the proposed model proposed in (4), the RCS statistics of the fully-illuminated vehicle case were calculated. Here $\widetilde{F_p}$ was set as random variable following Weibull distribution with $\beta = 0.33$. The full-illumination case when predicted from the partial-illumination resulted in $\widetilde{F_w}$ that had Weibull distribution with β in the range $0.88 \sim 1.0$, which is consistent with the experimental observations reported in Section 3.4.2. Figure3.16 shows the predicted ECDF resulting from 1000 trials while using $M = 35$ (the ratio of the full-illumination to the partial-illumination areas) along with the theoretical CDF of the Weibull distribution with $\beta = 0.918$. The result

Table 3.3: The shape parameter β for the best fit of the Weibull PDF to the measured data (partially-illuminated vehicle).

Vehicle	β	
	Co-pol	Cross-pol
Vehicle-1	0.3139	0.4060
Vehicle-2	0.3091	0.3938
Vehicle-3	0.3557	0.4154
Vehicle-4	0.3170	0.5018

shows that the statistical model of the fully-illuminated vehicle was accurately predicted using the model of partially-illuminated vehicle. Based on this result, the statistical model of any size illumination can be predicted. Similar simulation experiment has been performed for different illuminations in order to predict the shape parameter of the statistical model as the illumination size varies and the result is shown in Fig.3.17.

3.5 Conclusion

The phenomenology of polarimetric radar backscatter from vehicles was investigated at 222 GHz. Specific attention was devoted to the identifying sources of scattering from vehicles at this frequency along with the statistical properties of the backscattered return. High resolution outdoor measurements of stationary vehicles were performed using the synthetic aperture radar imaging technique. Additional complimentary measurements of the same targets were performed at close range and 3-D images were constructed with the radar operating in real-aperture mode. A fully polarimetric instrumentation radar operating at 222 GHz was successfully adapted for SAR imaging. It enabled 2-D imaging of vehicles with 7.5 cm × 3 cm in range and cross-range resolution. It was found that the major scattering is

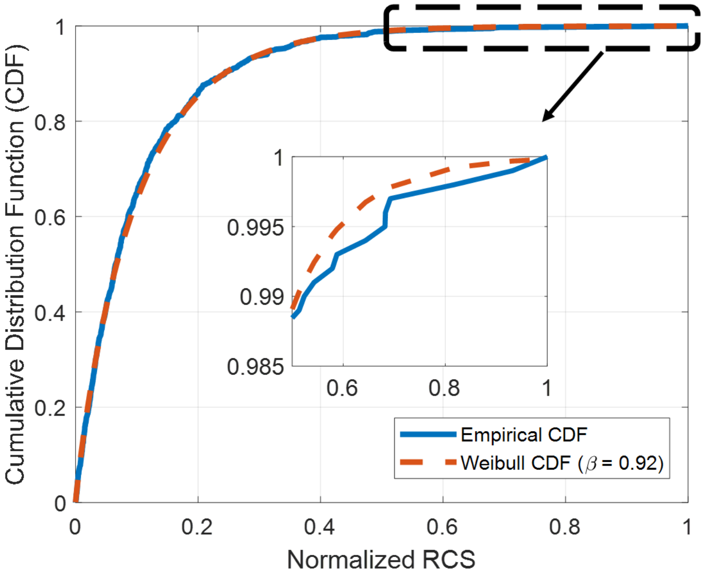

Figure 3.16: Comparison between the predicted ECDF using (4) with the standard CDF of Weibull function with $\beta = 0.918$. The fit is with $KS = 0.0279$.

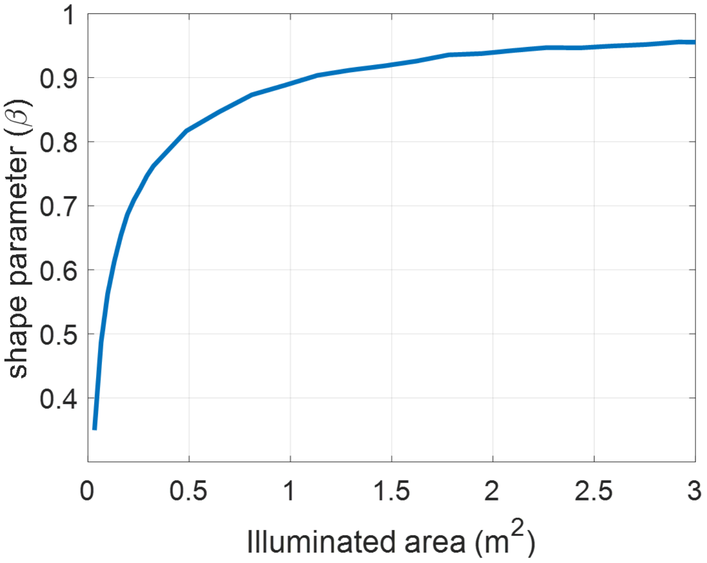

Figure 3.17: The estimated shape parameter (β) of the Weibull distribution as the statistical model of scattering from vehicles at different illumination sizes.

from a limited number of strong scattering phase-centers whose location and strength varied based on both polarization and relative look angle. Most of the scattering is from the outer surfaces of the vehicles facing the radar, and some scattering appears to be from the bottom surface of the vehicle after it undergoes specular reflections off of the road surface. In the experiments reported in this chapter, no scattering from the interior of vehicles was observed. For the co-polarized response, specular reflections were dominating and therefore they were sensitive to the relative look angle. At near 0° look-angle the scattering phase-centers were almost the same for all vehicles that were examined. However, they were different from one vehicle to another for the cross-polarized case. The statistics associated with scattering from vehicles are function of both the relative look angle and the illuminated area of the vehicle at any instant of time. However, it was found that the Weibull distribution was able to fit the measured data in most cases with a shape parameter that varies with the illuminated spot size of the vehicle. The results should provide useful information for the designers of radar sensors for autonomous vehicles at higher MMW frequencies.

CHAPTER IV

Road Surfaces Response to Automotive Radars Operating at Sub-Millimeter Wave Frequencies

4.1 Introduction

The radar function goes beyond detecting a target and measuring its distance to estimating the target's speed based on the frequency Doppler shift, recognizing some targets based on previously known specified features, and in some circumstances determining target qualities such as orientation. The knowledge required to phenomenologically examine and model common objects requires a thorough examination and modeling of these targets. Vehicles are the most obvious targets, as they must be identified, located, and assessed for qualities such as speed, orientation, and space occupied. The previous chapter was dedicated for this target class. The work presented in the this chapter focuses on the reflections from common surfaces encountered in road environments. When a specific object is to be detected or observed, the signal reflected by these surfaces is sometimes considered background clutter. As a result, the expected level of radar signal from these surfaces is critical. Furthermore, the signals from these surfaces provide extremely useful information for safely navigating the road. Asphalt in both new and old weathered conditions, concrete, dirt roads, and short grass are among the surfaces investigated in this study. And some of these surfaces were measured in both dry and wet conditions, as well as when they were covered in snow or ice. The radar sensor would be able to map the road, identify its lanes and boundaries, and detect any changes in the way to avoid debris, defects, or slippery places provided each surface and case were precisely characterized.

Even though surfaces of the same type may have minor variations due to aging, weather conditions, or construction procedures, they rarely alter dramatically. Some of the physical characteristics that influence the response must be recognized, either through theoretical understanding or through comprehensive measurements. This will enable the development of a model that takes these variations into account and is thus relevant to all surfaces with similar physical features. Many studies on the use of radars in road assessment and recognition rely solely on statistical and machine learning methods [76, 77, 78, 79, 80, 81]. Not only are these methods computationally intensive, but they also lack assurance, making decisions based on a single sensor unreliable. This research should result in a solid theoretical knowledge of radar backscattering from road surfaces, as well as a numerical method for estimating the response to a high level of reliability.

This chapter begins with the theoretical principles of radar backscattering, which will be based on theories that was found to be the most accurate in describing the scattering at this frequency. The measurements efforts, as well as the systems employed in this investigation, will be explained in Section 4.3. Algorithms, signal processing approaches, and calibration procedures will all be discussed as well. Then, the experimental results along with the modeling of various surfaces, in dry, wet or icy conditions, will be presented in sections 4.4 and 4.5.

4.2 Theoretical Models

Radars looking at the road ahead of the vehicle observe some backscattered signals from the road surface. This backscattered signal depends on numerous factors, such as surface roughness and density. Some of the radar signals might also penetrate the surface and scatter back due to the inhomogeneity of the material (asphalt or concrete). Volume scattering is the term used to describe radar scattering caused by propagation in inhomogeneous material. Surface scattering, on the other hand, refers to the scattering at the interface between two mediums. As opposed to planner interfaces where reflections only in the forward direction occur, when the interface has some irregularities, scattering in all directions might be encountered. In the following subsections, models for both types of scattering will be discussed.

4.2.1 Volume scattering

An inhomogeneous medium is composed of more than one material with different dielectric constants. Such medium can be considered a homogeneous medium with a single effective dielectric constant that contains some particles with different dielectric constants [83]. Examples of such medium are asphalt, concrete and snow. Many factors determine the radar scattering by a non-homogeneous medium. The size of the particles relative to the wavelength, their shape, orientation, density and distribution as well as the dielectric constant of each are all determining factors. Many studies have attempted to model the backscattering based on theoretical principles linked to these characteristics. And because of the complexity of practical problems solutions are usually based on some assumptions and approximations. One common approximation is the assumption of simple shapes for the particles, usually spherical, which holds quiet well when the particles are much smaller than the wavelength. Another assumption that simplifies problems is assuming no correlation between the particles and their positions, allowing the addition of their scattered power independently. Some of these solutions are based on the field equations and they involve Born approximation [92, 93]. This approach assumes one intact medium with fluctuations in the dielectric constant. The assumption of a spherical shape would greatly simplify the problem. However when the size become comparable with the wavelength this does not hold. Also, the assumption of spherical shapes cannot explain any depolarization unless solved for higher orders, which will further complicates the problem [94, 95]. Another theory that has been been used successfully in modeling volume scattering of different mediums is the radiative transfer (RT) theory [96, 97, 98, 99, 100]. The absence of correlation between different scatterers inside the medium usually is assumed in the mentioned works. And the majority of the research attempts to formulate the scattering in terms of the physical characteristics of the scatterers. This simplification would not be applicable to applications in the higher frequency range. Other empirical approaches are based on either measurements or numerical simulations were also used in many applications [101, 102, 103]. A method that combines the two approaches, has also been used especially when the numerical approximation restrictions and computational capabilities are exceeded, as is the case at higher MMW frequencies. This method was used successfully to model scattering from both road surfaces in [71, 72, 104] and snow in [105, 106, 107, 108, 109]. These studies employed the radiative transfer theory to create their models, but instead of relating the model inputs to the physical and statistical parameters of the medium, measurements were used to obtain such parameters. This last approach will be adopted in this study to model the backscattering response from various surfaces in this paper. The advantage of this method is that it does not require precise physical dimensions, and it does not assume that the particles are significantly smaller than the wavelength. However the characterization could be susceptible to any measurement errors and hence verification and close attention is necessary.

The vector radiative transfer equation is

$$\frac{d}{ds}\boldsymbol{I}(\hat{s},\boldsymbol{r}) = -\boldsymbol{\kappa}\,\boldsymbol{I}(\hat{s},\boldsymbol{r}) + \iint_{4\pi} \boldsymbol{P}(\hat{s},\hat{s}')\,\boldsymbol{I}(\hat{s}',\mathbf{r})\,d\Omega' \tag{4.1}$$

where $\boldsymbol{I}(\hat{s},\boldsymbol{r})$ is Stokes vector defined at $\boldsymbol{r}$ and propagating in the direction $\hat{s}$. $\boldsymbol{I}$ is a 4×1 vector whose components are: $I_v = |E_v|^2/\eta$, $I_h = |E_h|^2/\eta$, $U = 2\,\Re(E_v E_h^*)/\eta$, $V = 2\,\Im(E_v E_h^*)/\eta$, where E is the electric field, subscripts v and h stand for horizontal and vertical polarizations, respectively. $\boldsymbol{\kappa}$ is the extinction matrix, which accounts for intensity decays due to scattering and absorption ($\boldsymbol{\kappa} = \boldsymbol{\kappa}_s + \boldsymbol{\kappa}_a$). The assumption of an isotropic medium where no specific orientation has higher extinction rate reduces the extinction matrix to a scalar factor κ. This assumption is valid given the statistical symmetry of the medium [71]. The phase matrix $\boldsymbol{P}(\hat{s}, \hat{s}')$ is a 4×4 matrix that relates the scattered intensities from all directions $\hat{s}'$ to the direction $\hat{s}$. Basically, the radiatve transfer equation states that the intensity goes under a decay by absorption and scattering of the material where it propagates through, and it gains some power that is scattered toward the direction where it propagates.

The problem of interest is depicted in Fig. 4.1, where the incident and scattered specific intensities are defined in region-0 ($z > d$), a thin layer of a homogeneous medium occupies region-1 ($0 < z < d$), and the random medium is the semi-infinite region-2. The middle layer is added to represent water or ice if present, and will be used to model any surface irregularity. The RT equation needs to be solved for a downward directed specific intensity along $\hat{s}^-$ (with $ds^- = dz/\cos(\pi - \theta) = -dz/\psi$), which starts with the incident field in the upper half space, and for an upward going specific intensity along $\hat{s}^+$ (with $ds^+ = dz/\cos\theta = dz/\psi$), which subsequently will lead to the scattered field. $\psi = \cos\theta$. With this definition the limits of θ should be 0 to $\pi/2$. Also $d\psi = -\sin\theta\, d\theta$ with ψ's limits are 1 to 0. Therefore the upward and downward equations become:

$$\frac{d}{dz}\boldsymbol{I}^+(\psi, \phi, z) = -\frac{\kappa}{\psi}\boldsymbol{I}^+(\psi, \phi, z) + \boldsymbol{F}^+(\psi, \phi, z) \tag{4.2}$$

$$-\frac{d}{dz}\boldsymbol{I}^-(-\psi, \phi, z) = -\frac{\kappa}{\psi}\boldsymbol{I}^-(-\psi, \phi, z) + \boldsymbol{F}^-(-\psi, \phi, z) \tag{4.3}$$

where $\boldsymbol{F}^+(\psi, \phi, z)$ and $\boldsymbol{F}^-(-\psi, \phi, z)$ are the directing functions for both upward and downward intensities defined as

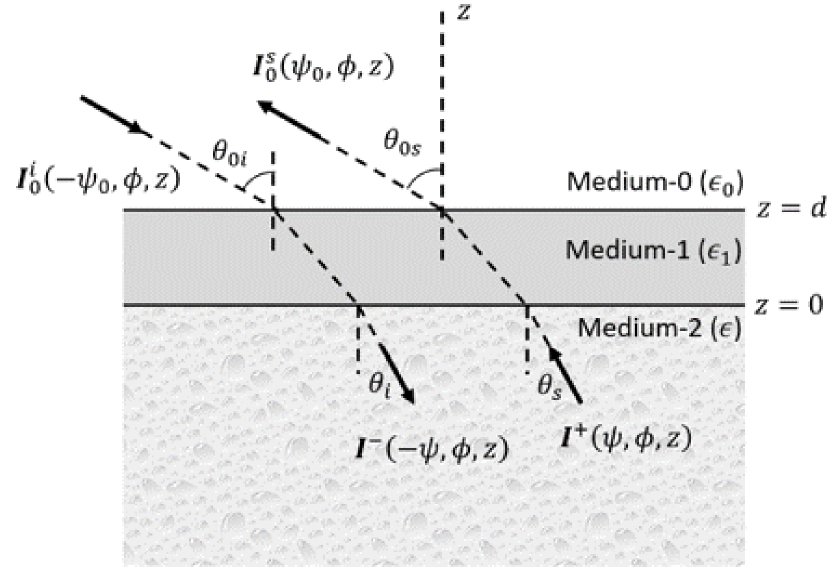

Figure 4.1: Illustration for the problem of volume scattering. Incident and scattered intensities are defined in region-0. The random medium is the bottom semi-infinite region-2. And the two regions are separated by a thin layer of a homogeneous medium of thickness d.

$$\boldsymbol{F}^+(\psi, \phi, z) = \frac{1}{\psi}\int_0^{2\pi}\int_0^1 [\,\boldsymbol{P}(\psi, \phi; \psi', \phi')\,\boldsymbol{I}^+(\psi', \phi', z) \\ +\ \boldsymbol{P}(\psi, \phi; -\psi', \phi')\,\boldsymbol{I}^-(-\psi', \phi', z)\,]\,d\psi' d\phi' \quad (4.4)$$

and $-\boldsymbol{F}^-(-\psi, \phi, z)$ has a similar form as (4.4) with replacing ψ by $-\psi$.

Without going through the detailed steps, the solution to these integro-differential equations can be found by multiplying (4.2) and (4.3) when in terms of z' by $e^{\kappa z'/\psi}$ and $e^{-\kappa z'/\psi}$, respectively, collecting the terms with $\boldsymbol{I}'s$ to represent the derivative of $\boldsymbol{I}$ multiplied by the exponent, and then integrating with respect to z' from $-\infty$ to z for the upward equation and from z to 0 for the downward equation to find the solutions:

$$\boldsymbol{I}^+(\psi, \phi, z) = \int_{-\infty}^{z} e^{-\kappa(z-z')/\psi}\,\boldsymbol{F}^+(\psi, \phi, z')\,dz' \quad (4.5)$$

$$\boldsymbol{I}^{-}(-\psi,\phi,z) = e^{\kappa z/\psi}\,\boldsymbol{I}^{-}(-\psi,\phi,0) \,+\, \int_{z}^{0} e^{\kappa(z-z')/\psi}\,\boldsymbol{F}^{-}(-\psi,\phi,z')\,dz' \tag{4.6}$$

the first order solution representing single scattering is the dominant and sufficient to represent the scattering. Giving this, the second term on the right side of (4.6) is ignored as with single scattering only the one global incident intensity is the local incident intensity, that is giving raise to one scattered intensity component per direction. Also, Only the second term inside the integral of (4.4) is attained, and by substituting (4.6) in (4.4) and then (4.4) in (4.5), we get the first order solution:

$$\begin{aligned}\boldsymbol{I}^{+}(\psi,\phi,z) = \int_{-\infty}^{z} & e^{-\kappa(z-z')/\psi}\,\frac{1}{\psi}\cdot \\ & \int_{0}^{2\pi}\int_{0}^{1} \boldsymbol{P}(\psi,\phi;-\psi',\phi')\,e^{\kappa z'/\psi'}\,\boldsymbol{I}^{-}(-\psi',\phi',0)\;d\psi' d\phi'\;dz'\end{aligned} \tag{4.7}$$

All the variables and equations above are defined in the non-homogeneous random medium (region-2), while the incident and scattered fields are defined in air (medium-0). Therefore, the problem should be subject to some boundary conditions at $z = 0$ (Fig. 4.1). Region-2 is assumed to be semi-infinite with no bottom boundary which is justified by the relatively small penetration depth at high frequencies. The boundary conditions to be satisfied at the interface are [110] (subscripts will be omitted for quantities in medium-2 while attained for those i medium-0):

$$\boldsymbol{I}^{-}(-\psi,\phi,0^{-}) = \boldsymbol{T}_{02}(\psi_0)\,\boldsymbol{I}_0^{i}(-\psi_0,\phi,0^{+}) = \boldsymbol{T}_{02}(\psi_0)\,\boldsymbol{I}_0^{i}\,\delta(\psi_0-\psi_{0i})\,\delta(\phi_0-\phi_{0i}) \tag{4.8}$$

$$\boldsymbol{I}_0^s(\psi_0, \phi, 0^+) = \boldsymbol{T}_{20}(\psi)\, \boldsymbol{I}^+(\psi, \phi, 0^-) \tag{4.9}$$

where $\boldsymbol{T}$ in the transmissivity matrix of a layered media. Using these boundary conditions in (4.7) at $z = 0$ yields:

$$\begin{aligned}\boldsymbol{I}_0^s(\psi_0, \phi, 0^+) = \boldsymbol{T}_{20}(\psi) \ \int_{-\infty}^{0} e^{\kappa z'/\psi}\, \frac{1}{\psi} \int_0^{2\pi} \int_0^1 \boldsymbol{P}(\psi, \phi; -\psi', \phi') e^{\kappa z'/\psi'}\, \boldsymbol{T}_{02}(\psi_0')\, \boldsymbol{I}_0^i \\ \delta(\psi_0' - \psi_{0i}')\, \delta(\phi_0' - \phi_{0i}')\, d\psi' d\phi' \ dz'\end{aligned} \tag{4.10}$$

In order to preform the integration, all arguments should match the integration variable. ψ_0 is the absolute independent variable, and ψ is determined from Snell's law. $\phi = \phi_0$. $\sqrt{\epsilon}\, \sin\theta = \sqrt{\epsilon_0}\, \sin\theta_0$ and $\sqrt{\epsilon}\, \cos\theta\, d\theta/d\theta_0 = \sqrt{\epsilon_0}\, \cos\theta_0$ and multiplying each side by its correspondent one in Snell's law: $\sqrt{\epsilon}\, \cos\theta\, \sqrt{\epsilon}\, \sin\theta\, d\theta = \sqrt{\epsilon_0}\, \cos\theta_0\, \sqrt{\epsilon_0}\, \sin\theta_0\, d\theta_0$ or $\epsilon\, \psi\, d\psi = \epsilon_0\, \psi_0\, d\psi_0$.

$$\begin{aligned}\boldsymbol{I}_0^s(\psi_0, \phi, 0^+) &= \boldsymbol{T}_{20}(\psi) \ \int_{-\infty}^{0} e^{\kappa z'/\psi}\, \frac{1}{\psi} \int_0^{2\pi} \int_0^1 \ \boldsymbol{P}(\psi, \phi; -\psi(\psi_0'), \phi_0')\, e^{\kappa z'/\psi(\psi_0')}\, \boldsymbol{T}_{02}(\psi_0')\, \boldsymbol{I}_0^i \\ &\qquad \delta(\psi_0' - \psi_{0i})\, \delta(\phi_0' - \phi_{0i})\, \frac{\epsilon_0\, \psi_0'}{\epsilon\, \psi(\psi_0')'}\, d\psi_0' d\phi_0' \ dz' \\ &= \boldsymbol{T}_{20}(\psi) \ \int_{-\infty}^{0} e^{\kappa z'/\psi} \frac{1}{\psi} \boldsymbol{P}(\psi, \phi; -\psi_i, \phi_i)\, e^{\kappa z'/\psi_i} \boldsymbol{T}_{02}(\psi_{0i})\, \boldsymbol{I}_0^i\, \frac{\epsilon_0\, \psi_{0i}}{\epsilon\, \psi_i} \ dz' \\ &= \boldsymbol{T}_{20}(\psi) \ \frac{\epsilon_0\, \psi_{0i}}{\epsilon\, \psi_i} \ \frac{1/\psi}{1/\psi + 1/\psi_i}\, \frac{1}{\kappa} \cdot \ \boldsymbol{P}(\psi, \phi; -\psi_i, \phi_i)\, \boldsymbol{T}_{02}(\psi_{0i})\, \boldsymbol{I}_0^i\end{aligned} \tag{4.11}$$

The case of interest is for backscattering where $\psi = \psi_i = \cos\theta_i$, $\psi_0 = \psi_{0i} = \cos\theta_{0i}$, and

$\phi = \phi_i + \pi$. And the intensity becomes independnt of z in the lossless upper half and hence the backscattered intensity becomes:

$$\boldsymbol{I}_0^s(\psi_{0i}, \phi_i + \pi) = \frac{\epsilon_0}{\epsilon}\frac{\psi_{0i}}{\psi_i}\frac{1}{2\kappa}\boldsymbol{T}_{20}(\psi_i)\,\boldsymbol{P}(\psi_i, \phi_i + \pi; -\psi_i, \phi_i)\,\boldsymbol{T}_{02}(\psi_{0i})\,\boldsymbol{I}_0^i \quad (4.12)$$

The phase matrix in the backscattering direction with the assumption of a statistically symmetric random medium takes the following form [106]:

$$\boldsymbol{P}(\psi_i, \phi_i + \pi; -\psi_i, \phi_i) = \begin{bmatrix} p_1 & p_2 & 0 & 0 \\ p_2 & p_1 & 0 & 0 \\ 0 & 0 & p_3 + p_2 & -p_4 \\ 0 & 0 & p_4 & p_3 - p_2 \end{bmatrix} \quad (4.13)$$

The entries to the phase matrix can be determined experimentally as it was done in [106]. The transmissivity matrix takes the following form [111]:

$$\boldsymbol{T}_{02} = \frac{\epsilon_2\mu_2\eta_0\cos\theta_2}{\epsilon_0\mu_0\eta_2\cos\theta_0}\begin{bmatrix} |t_{02}^h|^2 & 0 & 0 & 0 \\ 0 & |t_{02}^v|^2 & 0 & 0 \\ 0 & 0 & \Re(t_{02}^v t_{02}^{h*}) & -\Im(t_{02}^v t_{02}^{h*}) \\ 0 & 0 & \Im(t_{02}^v t_{02}^{h*}) & \Re(t_{02}^v t_{02}^{h*}) \end{bmatrix} \quad (4.14)$$

t_{02}^v and t_{02}^h are the filed transmission coefficients through a layered media for v- and h-polarizations. The transmissivity in the upward direction $\boldsymbol{T}_{20}$ has the same form as in (4.14) with interchanging the subscripts.

The radar scattering coefficient in terms of the incident and scattered intensities for backscattering case is given by [94]:

$$\sigma_{pq}^0(\theta_{0i}, \phi_i + \pi; \pi - \theta_{0i}, \phi_i) = \frac{4\pi\,\cos\theta_{0i}\,I_{0,p}^s(\theta_{0i}, \phi_i + \pi)}{I_{0,q}^i(\pi - \theta_{0i}, \phi_i)} \quad (4.15)$$

for an incidence q and scattered p polarizations. Substituting (4.14) and (4.14) into (4.12) and then using (4.15) the basckscattering coefficients are with omitting the subscripts for incidence are retaining those fir region from now on:

$$\sigma^0_{vv} = 4\pi \, \frac{\epsilon_0}{\epsilon_2} \, \frac{\cos^2\theta_0}{\cos\theta_2} \, |t^v_{20}|^2 \, |t^v_{02}|^2 \, \frac{p_1}{2\kappa} \tag{4.16}$$

$$\sigma^0_{vh} = 4\pi \, \frac{\epsilon_0}{\epsilon_2} \, \frac{\cos^2\theta_0}{\cos\theta_2} \, |t^v_{20}|^2 \, |t^h_{02}|^2 \, \frac{p_2}{2\kappa} \tag{4.17}$$

$$\sigma^0_{hh} = 4\pi \, \frac{\epsilon_0}{\epsilon_2} \, \frac{\cos^2\theta_0}{\cos\theta_2} \, |t^h_{20}|^2 \, |t^h_{02}|^2 \, \frac{p_1}{2\kappa} \tag{4.18}$$

The two factors p_1/κ and p_2/κ are the phase element normalized to the extinction coefficient which can be determined experimentally. These two factor are independent of the incidence angle and the single angle measurement is sufficient to calculate the scattering coefficient in all angle for backscattering setting.

4.2.2 Surface scattering

When the interface between two mediums becomes rough, another type of scattering should be accounted for, namely the surface scattering. Many efforts have been devoted to characterizing the surface scattering from many surfaces whether they were based on analytical, empirical or numerical approaches. Analytical approaches are very useful since they are not susceptible to measurements and simulation errors, however they usually involve some approximation to mediate the mathematical complexity. These approximations limit the validity to a specific range of problems. One of the classical solution is based on the small perturbation method which provide solutions in the low frequency region (or for lightly irregular surfaces). Another classical approach for rougher surfaces is Kirchhoff method [112, 113].

Another approach that came decades after to bridge the gap between these two methods was introduced in [114]. This approach is usually referred to as the integral equation method (IEM). The IEM can be thought of an extension to Kirchhoff method that accounts for some scattering components that otherwise neglected at high frequency regions. Although these models are not simple in their final forms, this still have wide range of applicability, some times beyond the proposed regions by the developers. Empirical models on the other hand provide simpler forms for engineers and researchers to compute, but their applicability region is rather narrow. An example of such empirical models can be found in [115]. This model was developed for incidence angles below 70^o and worked at our frequency as reported in [70]. However for angles beyond 70^o another model that was developed at a lower MMW frequency [86] failed to model the data at our frequency range. Therefore and involved theoretical model such as the IEM is chosen to characterize the surface scattering.

The integral equation method as suggested by its name is a mathematical solution to the well known Stratton-Chu integral. The integral relates the scattered filed to the incident field by:

$$\boldsymbol{E}^s_{qp} = \frac{-jk}{4\pi R}\, e^{-jkr} \iint \hat{q}\cdot\Big[-\hat{k}_i \times \big(\hat{n}\times \boldsymbol{E}_p\big) + \eta\,\big(\hat{n}\times \boldsymbol{H}_p\big)\Big]\, e^{-j\boldsymbol{k}_i.\boldsymbol{r}}\, ds \tag{4.19}$$

where E^s_{qp} is the scattered q-polarized electric field due to a p-polarized incident field. The details of the solution are well outlined in [114] and [116], and the final forms of the scattering coefficients for vv- and hh-polarization are:

$$\sigma^o_{pp} = \frac{k^2}{2}\, e^{-2s^2k_z^2} \sum_{n=1}^{\infty} s^{2n}\big|I^n_{pp}\big|^2\, \frac{W^n(-2k_x,0)}{n!} \tag{4.20}$$

where

$$I^n_{pp} = (2k_z)^n f_{pp}\, e^{-s^2k_z^2} + \frac{k_z^n}{2}\Big[F_{pp}(-k_x,0) + F_{pp}(k_x,0)\Big] \tag{4.21}$$

and W^n is the Fourier transform of the nth power of the surface correlation function $\rho^n(x,y)$

$$W^n(k_{sx}-k_x, k_{sy}-k_y) = \frac{1}{2\pi} \iint \rho^n(x,y)\; e^{j(k_{sx}-k_x)x + j(k_{sy}-k_y)y}\; dx\, dy \tag{4.22}$$

and the factors F_{pp} and f_{pp} are given by the formulas:

$$f_{vv} = 2\, r^v / \cos\theta_0 \tag{4.23}$$

$$f_{hh} = -2\, r^h / \cos\theta_0 \tag{4.24}$$

$$\begin{aligned} F_{vv}(-k_x,0) + F_{vv}(k_x,0) = {} & \frac{2\,\sin^2\theta_0\,(1+r^v)^2}{\cos\theta_0} \\ & \cdot \left[\left(1 - \frac{1}{\epsilon_r}\right) + \frac{\mu_r\epsilon_r - \sin^2\theta_0 - \epsilon_r\,\cos^2\theta_0}{\epsilon_r^2\,\cos^2\theta_0} \right] \end{aligned} \tag{4.25}$$

$$\begin{aligned} F_{hh}(-k_x,0) + F_{hh}(k_x,0) = {} & -\frac{2\,\sin^2\theta_0\,(1+r^h)^2}{\cos\theta_0} \\ & \cdot \left[\left(1 - \frac{1}{\mu_r}\right) + \frac{\mu_r\epsilon_r - \sin^2\theta_0 - \mu_r\,\cos^2\theta_0}{\mu_r^2\,\cos^2\theta_0} \right] \end{aligned} \tag{4.26}$$

r^v is the Fresnel magnetic reflection coefficient for vertical (TM) polarization, and r^h is the Fresnel electric reflection coefficient for horizontal (TE) polarization. For the vertical polarization the difference between the magnetic and electric coefficient is a minus sign which will be refereed to later.

The above solution considers only single scattering. multiple scatterings is negligible when compared to single scattering for co-polarization and hence does not need to be computed. Depolarization however is observed only when more than one bounce by the surface facests occur. Another formula that accounts for multiple scattering is

$$\sigma^o_{vh} = \frac{k^2}{16\pi}\; e^{-2s^2k_z^2}\; \sum_{n=1}^{\infty}\sum_{m=1}^{\infty} \frac{\left(s^2k_z^2\right)^{n+m}}{n!\,m!} \cdot \iint \left[\left|F_{vh}(u,v)\right|^2 + F_{vh}(u,v)\,F^*_{vh}(-u,-v)\right] \cdot W^m(u-k_x,v)\,W^n(u+k_x,v)\;du\,dv \quad (4.27)$$

Even though the summations are infinite, a sum up to 4 should be sufficient. $\sigma^o_{vh} = \sigma^o_{hv}$. And the factor $F_{vh}(u,v)$ is determined by:

$$\begin{aligned} F_{vh}(u,v) = \frac{u\,v}{k_0\cos\theta_0}\Big[& \\ & -\left[\left(1-r^x\right)/w_0 - \left(1+r^x\right)\mu_1/w_1\right]\left(1+r^x\right) \\ & +2\left[\left(1-r^x\right)/w_0 - \left(1+r^x\right)/w_1\right]\left(1-r^x\right) \\ & -\left[\left(1-r^x\right)/w_0 - \left(1+r^x\right)/(\epsilon_1\,w_1)\right]\left(1+r^x\right) \\ & -\left[\left(1+r^x\right)/w_0 - \left(1-r^x\right)\epsilon_1/w_1\right]\left(1-r^x\right) \\ & +2\left[\left(1+r^x\right)/w_0 - \left(1-r^x\right)/w_1\right]\left(1+r^x\right) \\ & -\left[\left(1+r^x\right)/w_0 - \left(1-r^x\right)/(\mu_1\,w_1)\right]\left(1-r^x\right)\Big] \end{aligned} \quad (4.28)$$

where r^x is the difference in Fresnel electric field reflection coefficient between vertical and horizontal polarizations (i.e $r^x = -r^v - r^h$). w_0 and w_1 are the z-components of the interim propagation constant:

$$\begin{aligned} w_0 &= \sqrt{k_0^2 - u^2 - v^2} \\ w_1 &= \sqrt{k_1^2 - u^2 - v^2} \end{aligned} \quad (4.29)$$

Another factor in the solution that should be account for is the shadowing by the roughness of the surface especially at higher incidence angles. The shadowing function $S(\theta_0)$ represent the probability that a point on the rough surface is illuminated by the radar beam. $S(\theta_0)$ can be simply multiplied by the the the scattering coefficient to account for the shadowing. One simple formula for the shadowing is derived in [117] which is given by:

$$\begin{aligned} S(\theta_0) &= \frac{1}{1+\Lambda(\theta_0)} \\ \Lambda(\theta_0) &= \frac{0.5}{\sqrt{\pi}} \frac{e^{-(\cot\theta_0/\sqrt{2}m)^2}}{\cot\theta_0/\sqrt{2}m} - erfc(\frac{\cot\theta_0}{\sqrt{2}m}) \end{aligned} \tag{4.30}$$

where m is the rms slop of the surface which can be approximated by $m = s/l$.

4.2.3 Combination of volume and surface scattering

To account for both volume and surface scattering, the absence of correlation between the two is employed to add the two coefficients. The volume scattering, however, assumes a planner interfaces between the two mediums. If the roughness seen by the radar wavelength along z-direction is small (i.e. $k_z \ll 1$), as it is the case in this study, then the effect of the roughness on the volume scattering is small. To better account for this roughness effect on the transmission between the two layers, a thin homogeneous layer between the two mediums with a dielectric constant that is the average of the two mediums can be assumed. The thickness of the layer can be assumed as double the rms height of the surface s, as depicted in Fig.4.2.

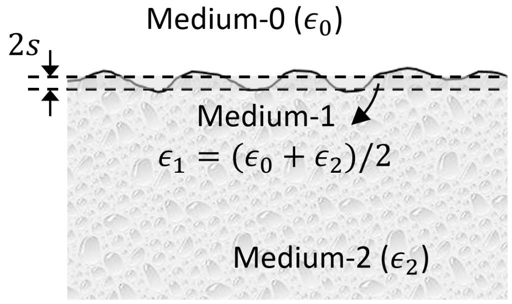

Figure 4.2: A third homogeneous layer is added to replace the roughness for the volume scattering RT based model. The thickness of the layer in double the rms roughness height s and its dielectric constanst is the average of the two layers.

4.3 Instrument Radar, Measurement Procedure, and Data Processing Techniques

Both of the two instrument radar systems introduce in Chapter II were used in this study. They are built to conduct different experiments and their working principles are different. Some measurements reported in this chapter were conducted using both systems and similar results are found proving evidence for the accuracy of the experimental results.

In autonomous vehicles, sensors scanning ahead of vehicles are usually placed on the bumper at a height in the order of 60-cm, resulting in incidence angles in the range between 80^o and 90^o. As it was seen in the theoretical analysis, the incidence angle has significant impact on the response level. Therefore measurements are performed for different angles. Also, the statistical nature of scattering from such randomly shaped surfaces requires acquiring enough samples at each angle in order to observe the behavior. With the help of a motorized 2-D horizontal scanning platform that has gimbals to adjust for the looking angle, at least 40 samples are collected for each angle and polarization. The data is processed afterward to invert for the scattering coefficient. Full polarimetric calibration of the data is performed based on the method in [118] which requires the measurement of a metallic sphere plus any second target with a strong cross-polarized radar cross section.

In order to characterize the profiles of surfaces measured, a laser profilometers is placed on a very precise linear translator to measure the surface heights. Measurements spaced 100 μm over 10 mm lengths are taken at various spots at each site.

4.4 Experimental Results for Bare Road Surfaces

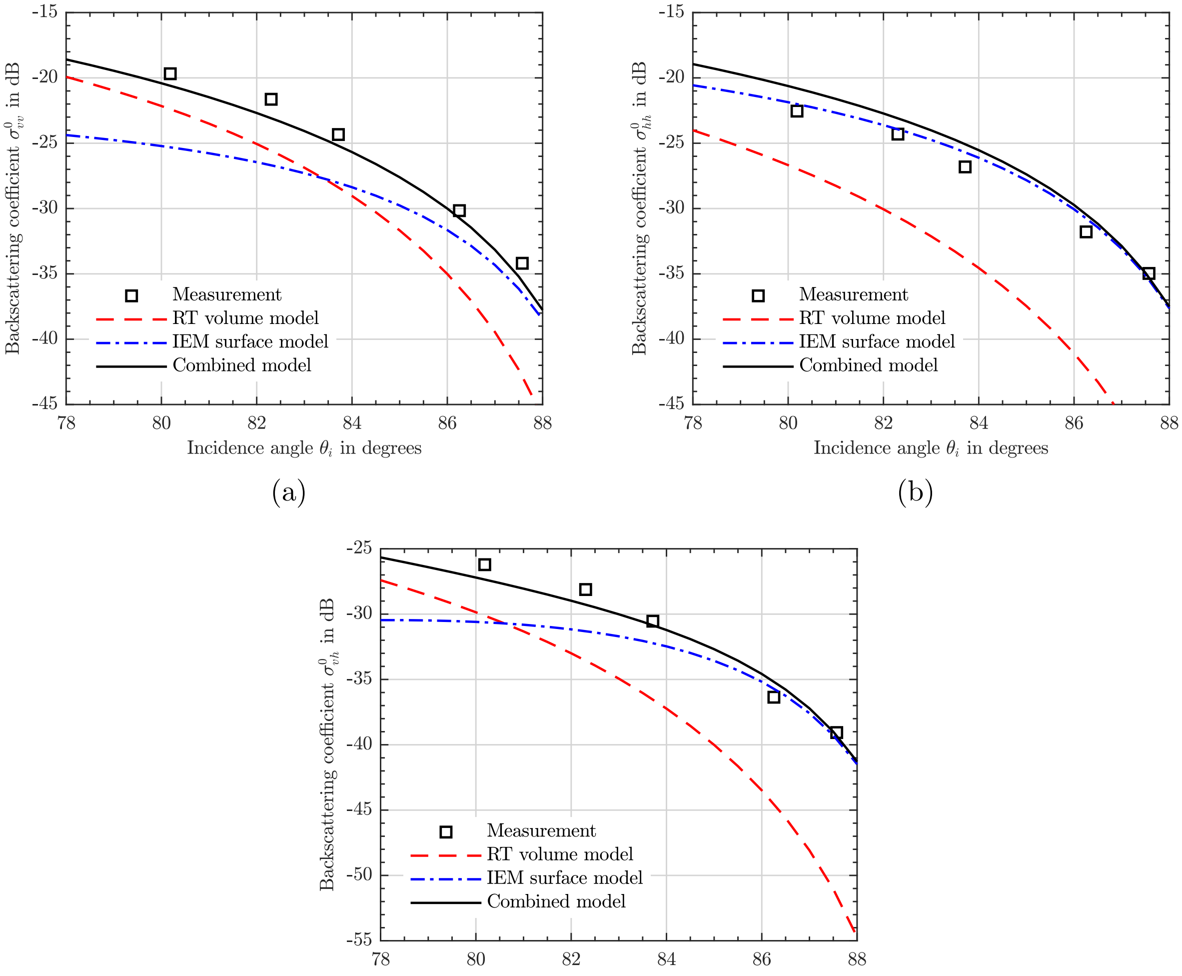

(a)

(b)

(c)

Figure 4.3: The angular response for the baskscattering coefficient of asphalt (site-1). Measured data is plotted vs the proposed model. The two scattering models (volume based on the radiative transfer theory and surface based on integral equation method) are plotted to show each model's contribution. The combined model is the some of the two models. The response are for (a) VV-polarization, (b) HH-polarization and (c) VH-polarization

The term asphalt sometimes used to refer to bitumen which when mixed with aggregate form what scientifically named concrete asphalt and commonly named asphalt or pavement. It is the most common road construction material that when laid in layers and compacted results in most efficient and less noisy roads. The Difference in dielectric constants of bitumen, aggregate, and air gaps causes the volume scattering within the material. Also the top the surface has some textures which is sometimes intentional to reduces slipperiness and could increase intensive use over time, which causes the surface scattering at the interface. In order to model the response from asphalt the effective dielectric constant has to be known. Determining the effective dielectric constant of asphalt theoretically based on its the constitutes can be challenging especially when accurate dielectric constants of its components are not well known. However the radiative transfer model with the approach proposed in this paper requires mainly the real part as it is the dominant part in determining the transmissivity at the interface between asphalt ans air. Fortunately the real part is very weak function of frequency and the closet frequency that it was characterized at is 95 GHz [71] and determined to be $\epsilon'_{asphalt} = 3.18$. This results was verified to be valid at 222 GHz in [70]. Yet the imaginary part at 222 GHz frequency is expected to be higher than the one reported in [71] $\epsilon'' = 0.1$ but it is still expected very low to influence the transmissivity. Based on the measurements performed, the ratio of the phase element to the extinction factor where found for asphalt as listed in Table-4.1. Another factor that affect the response from asphalt is its roughness, which can be sufficiently characterized by the root mean square (rms) height, correlation length and the correlation function of the surface profile [116]. This site has a relatively worn asphalt with rms height $s = 0.36\,mm$, correlation length $l = 2.3\,mm$ and the correlation function falls in between two standard functions namely exponential and x-exponential function with $x = 1.5$. These two function are descried in [116] along with their Fourier transforms. The average of these two functions is used in the surface model.

The measurement results of the backscattering coefficient along with the models for asphalt site-1 are plotted in Fig. 4.3. It is apparent from the results that both volume and

Table 4.1: The Ratio of the Phase Element to Extinction Factor in the Radiative Transfer Model for Asphalt

$p_1/(2\kappa)$	$p_2/(2\kappa)$
0.07	0.02

surface scattering have to be accounted for, however, HH-polarization response seems dominated by surface scattering. On the other hand, VV-polarization response can not be explained by either volume or surface scattering alone, even though the former seems to dominate at incidence angles below 82^o, and the latter is almost the only form for incidence angles very close to grazing. The behavior is predicted as the transmission coefficient decays with increasing the angle of incidence, while the reflection coefficient is the opposite. Cross-polarization comes in between VV- and HH-polarization in term of the volume and surface scattering, a logical expectation. These results emphasize the usefulness of radar polarimetry. Even when the cost or size become obstacle in having full polarimetry in operational radars, the choice of polarization for single polarization radar can be optimized based on the application.

The backscatter response from asphalt was measured in two other sites of different surface profiles. Site-2 has newly constructed asphalt, while Site-3 has almost the same age as site-1 but it seemed to be in better condition due to less intensive use. The roughness data of the three asphalt sites are listed in Table-4.2. Figure. 4.4 shows the response of the second site of asphalt with relatively smoother surface. The results shows less response at HH-polarization as expected from the surface scattering to drop, while the VV-polarization does not seems to depend on the roughness except at higher incidence angles. The volume scattering of all asphalt surfaces is the same making VV-polarization to appear independent of the surface roughness. The results from site-3 are not far from those of site-1 given the close values of roughness parameters as shown in Fig 4.5. Figures. 4.4 and 4.5 show how for a rough surface VV and HH responses become very close, while for the smooth case HH drops to be closer

Table 4.2: Roughness Data for the Three Asphalt Sites Where Measurements Were Conducted

Sites	rms height (s)	correlation length (l)
site-1	0.36 mm	2.3 mm
site-2	0.18 mm	.76 mm
site-3	0.35 mm	2.5 mm

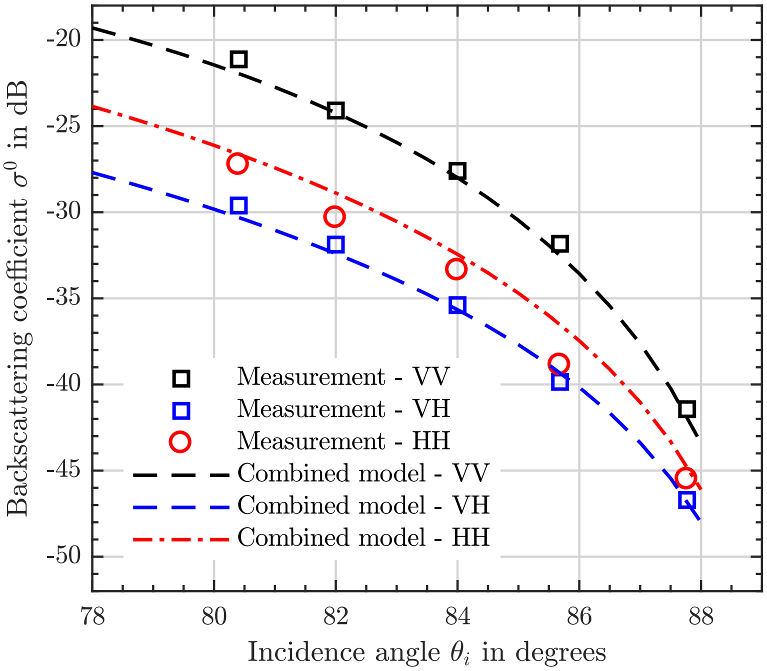

Figure 4.4: The angular response for the baskscattering coefficient of asphalt (site-2). Measured data is plotted vs the proposed model. The parameters of the models are listed in Table-4.1 and 4.2

.

to the cross-polarization response. It should be noted that the jump in the measurement response in cross-polarization in Fig. 4.5 at angle 88^o is due to the very low signal-to-noise ratio (SNR) level and the response might be dominated by noise.

Another material which roads sometimes are constructed with is concrete. Whether it was reinforced with steel or just cement mixture, concrete roads are very durable and have longer live time than asphalt, but despite being less safe than asphalt they are more costly. Even with the texture that usually finished with, concrete is more slippery especially under wet

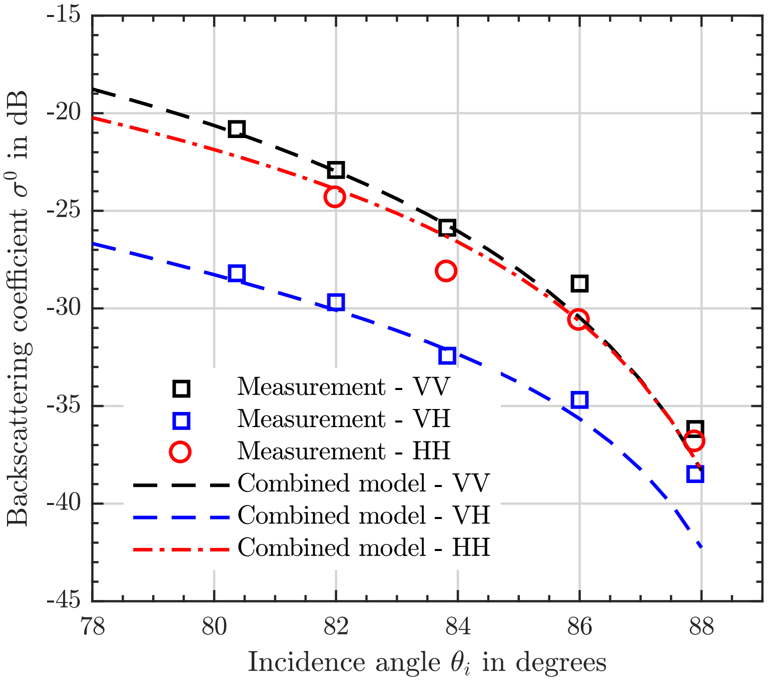

Figure 4.5: The angular response for the baskscattering coefficient of asphalt (site-3). Measured data is plotted vs the proposed model. The parameters of the models are listed in Table-4.1 and 4.2

.

and icy conditions. The response of concrete surface has been measured and modeled and the results are shown in Fig. 4.6. The response is noticeably weaker than asphalt. The surface scattering being weaker in obvious, volume scattering in the other hand is weaker mainly because it has denser mix and therefore closer to a homogeneous medium than asphalt. The effective dielectric constant of concrete is estimated to be about 4.17 [71, 70]. The RT model parameters for concrete are determined from the measurements and listed in Table-4.3. The roughness data for this surface were found to be $s = 0.15\,mm$ and $l = 2.9\,mm$ The deviation between the model and measurement at higher incidence angle of cross-polarization is due to the fact the signal is very weak and could be corrupted by noise.

Third type of surfaces that are usually encountered, especially in rural areas, is unpaved road or as it is usually known for dirt roads. Yet these types of surface are harder to characterized, and they vary greatly depending on their roughness and wetness, an example

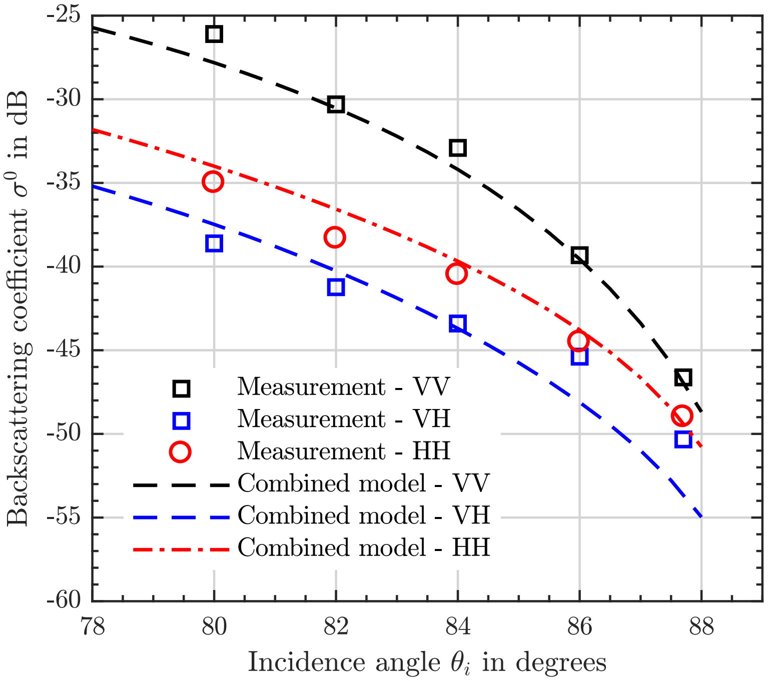

Figure 4.6: The angular response for the baskscattering coefficient of concrete surface. Measured data is plotted vs the proposed model. The parameters of the models are listed in Table-4.3 for the volume RT model, and $s = 0.15\,mm$ and $l = 2.9\,mm$ for the surface IEM model

.

Table 4.3: The Ratio of the Phase Element to Extinction Factor in the Radiative Transfer Model for Concrete

$p_1/(2\kappa)$	$p_2/(2\kappa)$
0.002	0.006

of such surfaces is presented here to show roughly the expected response. The measurements of the backscattering coefficient of an unpaved road surface is shown in Fig. 4.7. The results show that for very rough surfaces VV and HH responses become almost the same. The response from the side of the road is of interest sometime to determine the road edges. The unpaved road is similar to the side of regular roads in some cases. Also, a common cover for the road side is grass. The response from grass depends on its size, height and wetness as well as other factor. An example of the response from grass is shown in 4.8. The contrast in

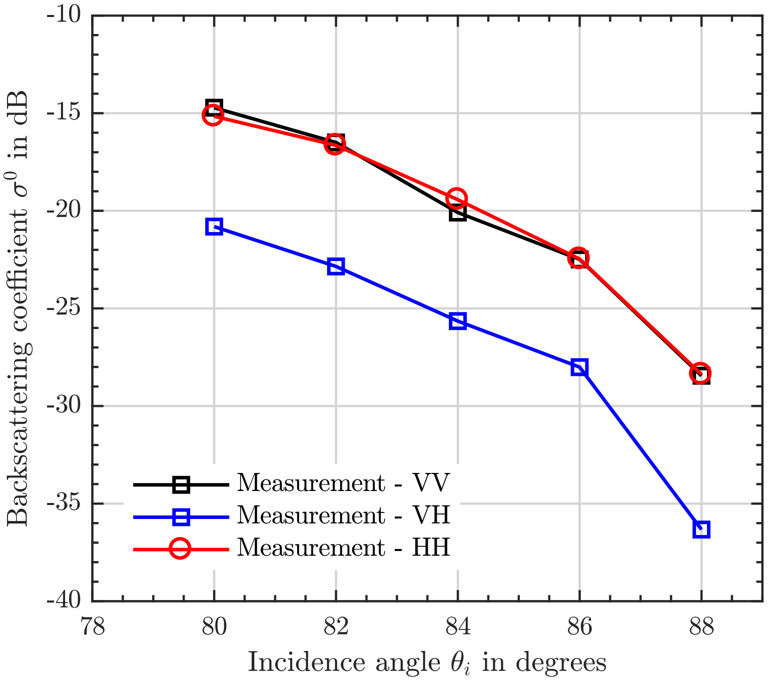

Figure 4.7: The angular response for the baskscattering coefficient of an unpaved road.

the responses of these last two surfaces and others is apparent, an advantage can be used in sensors to determine the road edges very accurately.

4.5 Responses from Snow and Ice-covered Surfaces

Scattering from snow have attracted too much attention due to its complexity and importance. Snow is small particles of ice that can take very wide range of shapes. The interconnection between these particles is one of the characteristics of snow. Temperature is also and important factor since when ice starts to melt, water will be part of the medium which have completely different characteristics. At MMW the size of snow flakes becomes comparable with wavelength making the shape of flakes matters in their responses. Without diving deep into snow characteristics and their relations to its response some measurements are conducted and the RT volume scattering solution is used to model the responses. Deviation in density or any other characteristic in the snow might change the response, however, measurements

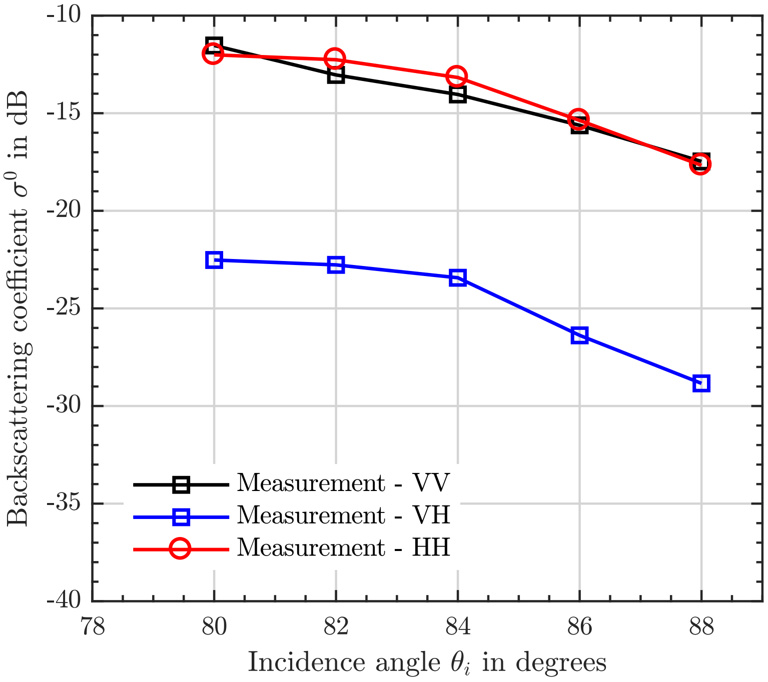

Figure 4.8: The angular response for the baskscattering coefficient of 9-cm long grass.

Table 4.4: The Ratio of the Phase Element to Extinction Factor in the Radiative Transfer Model for snow of 15% density

$p_1/(2\kappa)$	$p_2/(2\kappa)$
0.95	0.2

have shown very narrow range of variation under typical conditions. The effective dielectric constant for snow can be estimated using some mixing formulas like Polder–Van Santen mixing formula. A snow of density 15% and at temperatures well below freezing is estimated to be $\epsilon_{snow} = 1.25 + j0.0012$ given that the dielectric constant of ice is $\epsilon_{ice} = 3.18 + j0.018$.

An example of the measured backscattering response from snow is presented in Fig. 4.9. The density of this snow site was measured to be 15% and it has thickness of about 9-cm. The response is expected to be from the snow only since no signal is expected to penetrate to reach the underlying surface. The snow particles has spectrum of shapes and sizes. spherical, stars and strip shape were all identified, and the sizes ranged from 0.1 to 1 mm. The RT model provides good estimate of the response with the normalized phase elements listed in

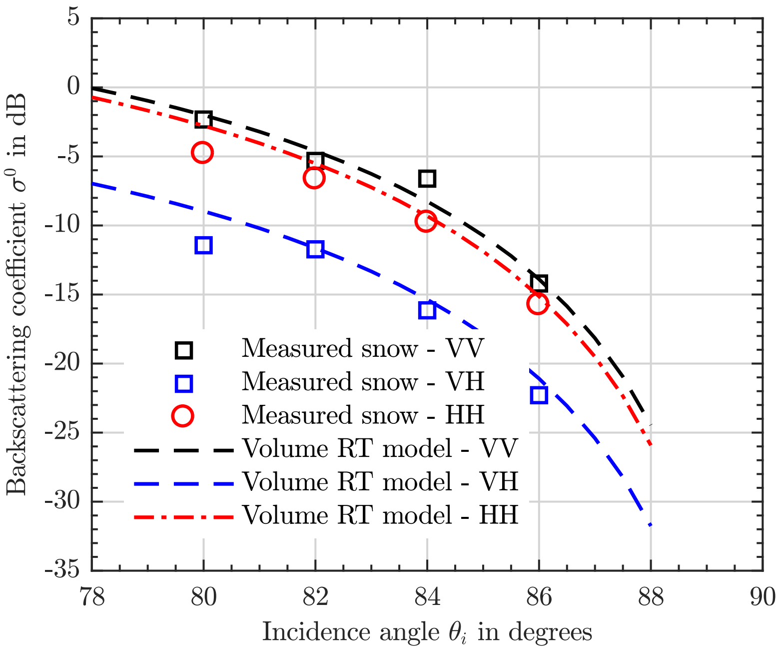

Figure 4.9: The angular response for the baskscattering coefficient of a thick layer of snow.The RT volume model is sufficient to model the response with the parameters in Table-4.4.

Table-4.4.

The presence of a layer of ice over the surface could be very slippery and often considered a danger given its invisibility in most cases. The backscatter response with the presence of such thin layer of ice atop the road surface is expected to change since the penetration through ice would attenuate the signal. This scenario can be formulated using the RT volume model of three layer, the middle layer being the ice. The presence of roughness on the surface requires more careful consideration. However, the dielectric constant of ice ($\epsilon_{ice} = 3.18 + j0.018$) is very close to that of asphalt and since the surface scattering depends on the ratio between the two dielectric constants of the two surfaces, it is expected to be negligible. Two measurements were conducted to verify these assumptions. A thin layer of ice on top of asphalt and on top of concrete are presented in Figs. 4.10 and 4.11. The thickness of the ice layer is 3 mm in both cases and the volume model show very good agreement with measured data.

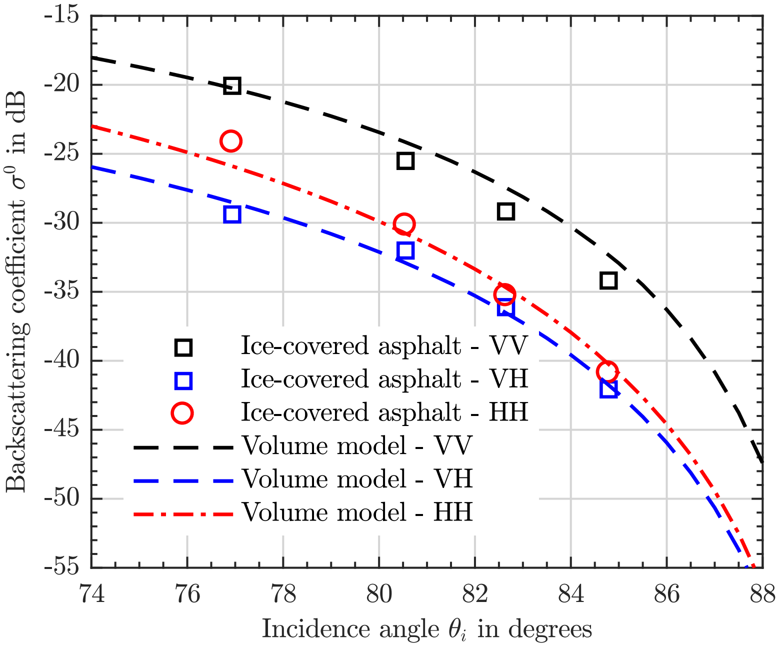

Figure 4.10: The angular response for the baskscattering coefficient of ice- covered asphalt. The ice thickness is 3 mm. The RT volume model is sufficient to model the response.

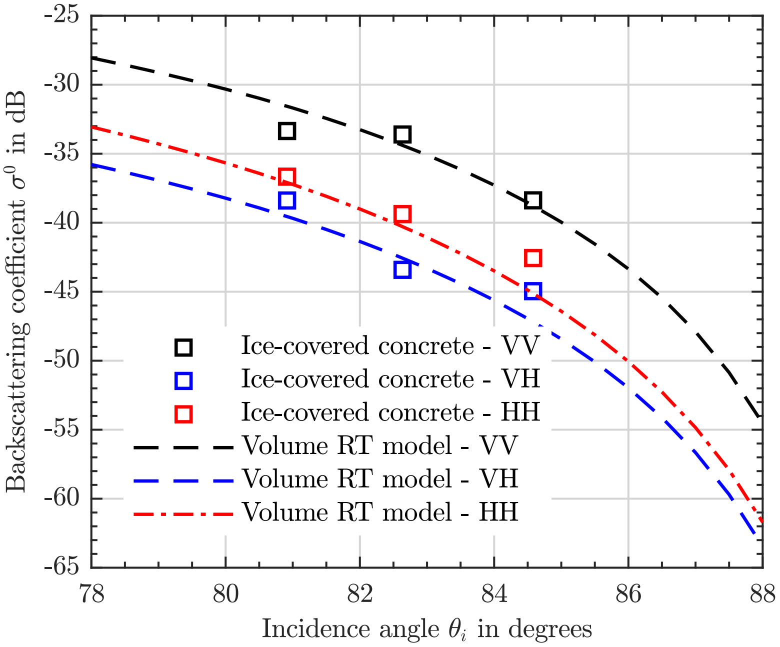

Figure 4.11: The angular response for the baskscattering coefficient of ice- covered concrete. The ice thickness is 3 mm. The RT volume model is sufficient to model the response.

4.6 Conclusions

This Chapter investigated and characterized the radar backscatter response from various road surfaces at J-band. Backscattering models were developed and verified using experimental data that was collected as part of the effort. The polarimetric response from road surfaces at near-grazing (80 to 88^o) incidence angles was examined for applications in road surface recognition. Knowing the expected backscatter signal level is useful in the design of detection algorithms of other objects in the presence of this background. It is also very useful for mapping the road, detecting harmful objects and debris, and assessing the road condition. Surfaces under wet, ice-covered, or snow-covered conditions were also examined and characterized. The radar backscatter response at J-band is explained by a combination of both volume and surface scatterings. The volume scattering was modeled based on the vector radiative transfer theory and simple formulas that estimates the response were derived. The integral equation method (IEM) provided an excellent agreement with experimental data for surface scattering contribution to the overall response.

CHAPTER V

Characterization of the Response from Human Subjects at J-Band.

Human safety as passengers or pedestrians has always been atop issue by car manufacturers and proponents of autonomous vehicles. Detection and identification of such subjects should be robust and could consist of multi-layer algorithms to ensure high level of reliability. Detection and identification of pedestrians should be robust and could consist of multi-layer algorithms to ensure a high level of reliability. In this section, various radar features are examined to better assist the ability of automotive radars to detect and identify human subjects against other objects. These features are examined for the first time at J-band.

5.1 Radar Backscatter Features of Human Subjects

The investigation conducted and discussed in this chapter provides the first knowledge base for four possible detection and identification algorithms for human subjects. The first straightforward detection method is based on the power level of radar backscatter from targets which is related to their RCS values. However, recognizing the source of radar return based on the quantitative measurement value of RCS cab be quite unreliable. That is not only because many objects reflect electromagnetic waves in similar amounts but also because an object reflectively could change dramatically depending on many factors. These factors include shape, orientation, movement, and other conditions such as the target being wet. Also, environmental condition such as the weather can change the wave propagation parameters and influence the level of received power [83]. It is noted that, accurate RCS measurements require frequent calibration for the radar. This process requires extra hardware and cannot easily performed for operational radars since achieving the accuracy required one must operate in controlled environment. Nevertheless, radar backscatter measurement can help narrow down semantic target section estimation.This in combination with some of the novel identification techniques should result in considerable better identification accuracy.

Radar polarimetry provides another degree of freedom since many targets of similar RCS values at a specific polarization could have completely different signatures under another polarization state. RCS is primarily proportional to the target size, shape, and orientation with respect to the transmitted polarization. Conversely, depolarization -for example- depends mainly on the target's intricacy and texture. Therefore, features of radar polarimetry should be apparent and effective in distinguishing specific targets with distinctive details. The human body is an example of a complex target where various body parts have different orientations, and higher order reflections become substantial. In fact, even the simplest objects have distinct polarization signature. The measurement of the polarization signature requires a full-polarimetric radars that are capable of transmitting and receiving coherently two principal polarizations (vertical/horizontal or Left/Right circular polarizations). Such systems might not be cost-effective to be installed on vehicles. However, the knowledge of the polarization signature of an object of interest can be used to choose the appropriate polarization in both transmit and receive antennas of a non-polarimetric radar to increase target identification [74]. This technique has been used successfully in many scenarios to detect targets of weak responses in a very cluttered background [119, 120, 121]. In addition, as discussed in Chapter-I, the advent of MMW ICs permitted radars to increase the number of RF channels and antenna elements to improve resolution and scanning capabilities. Therefore, multiple antennas can combine more than one polarization in automotive radars, providing extra information without adding complexity. Given that, a good understanding of the polarimetric response is essential. A complete study of the polarimetric response of human subjects is performeds, which in turn should enable radars to recognize human radar responses from those of the other objects.

Unlike point targets where the scattering mechanisms are somewhat deterministic, physically complex and large targets with many scattering centers have rather complicated scattering behavior. In such cases, the slightest change in the shape or orientation of the target and/or the radar could result in a substantial difference in response, especially at higher MMW frequencies; therefore a statistical approach must be considered. Since a statistical study requires extensive measurements of the same target, it is impractical to perform such measurements on real people. Hence these experiments are mostly performed on a mannequin that showed a similar response to a real human. Once fluctuations in the response are statistically modeled, measurements can be linked based on their correlation to the model for accurately detecting human subjects [122, 123].

One great advantage of operating at higher frequencies is the fine measurement of Doppler frequency since it has inverse proportionality to the wavelength. Based on many measurements performed on driving vehicles, only a single Doppler component is usually observed, despite the existence of other motions like rotating tires. On the contrary, Doppler measurements of a moving person show many Doppler components due to the oscillating motion of limbs. The Doppler spectrum of a moving body can be used by automotive radars to recognize pedestrians from other objects that may be in the same range bin and are of comparable radar cross-section. Many studies at lower MMW frequencies have shown that moving pedestrians can be identified accurately using their micro-Doppler signatures [124]. This feature is also investigated at 230 GHz. In this work, many measurements of a moving person at different speeds are measured, and the spectrum of the Doppler frequency components is isolated from the measurement background. Different features of typical periodical variations of the Doppler velocity under various movement speeds (walking, running, and jogging) are examined. The aim is to identify the spectrum signature of a moving human body at different states and as observed from different directions.

Automated vehicles with multi-layer identification algorithms incorporating some or all of the mentioned features would improve pedestrians' safety and enhance the driving safety for everyone.

5.2 Radar Backscatter Examination of Human Subjects

The human body is somewhat complex due to its size compared with the wavelength of MMW frequencies. Unlike the torso, which represents the body's biggest and most straightforward part, the limbs are far more complicated despite the expected lower response they present compared to that of the torso. Their movement with respect to the torso could change the overall response significantly. Due to the complex nature of radar response, it is required to perform an experimental-based study to examine the backscatter response accurately. Moreover, the orientation and aspect angle of the radar with respect to the body would change the scattering mechanism completely. Therefore, in the experimental study, 360 degrees measurements of the radar response are performed for each case to capture the angular variation of the response. Given the fine resolution (1.1-degree effective HPBW) for the available radar, only a limited height portion of the body is illuminated and measured in each horizontal sweep. Also, given the need to measure most accurately by placing the target inside an anechoic chamber and at a reasonable stand-by distance from the radar to maintain acceptable power levels, all these factors raise the importance of the consistency between different measurements. It should be noted here that our aim is consistency rather than repeatability since the latter is nearly impossible at such short wavelength frequencies. Therefore, a mannequin designed to mimic the human having skin reflectivity and size and figure similar to live humans is used to conduct most of the measurements. The mannequin's resemblance to human properties is verified at lower microwave frequencies; therefore, the measurements in some cases are performed on real humans to compare their response with that of the mannequin. Figure.5.1 conceptually shows the setup with an illustration of directing the radar beam focus on different height sections of the mannequin, along with a captured photo of the setup while the measurement is underway. Full polarimetric measurement is taken in azimuth at 1-degree increments, and the pointing is adjusted to perform the same at each height. The illuminated area on the mannequin is about 31 cm in diameter, and the distance between the radar and the object under measurement is 15m. The FMCW experimentation radar introduced in Chapter II is the system used in these experiments. The operating frequency was around 226.3 GHz and over 1 GHz bandwidth.

5.3 Experimental Results and Observations of Human RCS

The RCS variation over the 360 degrees rotation for the case where the radar is looking at the chest level are presented in Fig.5.2, for VV-, HH-, and cross-polarization (HV). The radar is polarimetrically calibrated using a 2-inch metallic sphere and a dihedral which has a significant depolarization level based on the method in [118]. It should also be noted that cross-polarization here could mean both HV- and VH-polarizations since they are essentially the same in the backscattering scenario except for small measurement uncertainty and the noise. The noise level after full calibration averages around -55 dBsm; hence at least 25 dB signal-to-noise ratio (SNR) is retained for cross-polarization measurements. The backscattering map shows higher RCS values in both VV- and HH-polarizations from the back side of the mannequin, as compared with the front side, which still exhibits stronger response than the left and right sides. On the other hand, the two sides show a comparable cross-polarization level with the back. All these observations will be displayed more explicitly later in the section. Algorithms for detection and identification based on polarimetric radar signature usually deals with ratios between different polarizations rather than the absolute value of each. The co-polarization ratio is defined as the ratio of the RCS value at HH- to VV-polarizations ($p = \sigma_{hh}/\sigma_{vv}$). And the cross-polarization ratio is defined here as ($\chi = \sigma_{hv}/\sigma_{vv}$) rather than the most general definition ($\chi = (\sigma_{hv} + \sigma_{vh})/(\sigma_{vv} + \sigma_{hh})$), and that is to ensure accurate reference of cross-polarization to co-polarization, as the HH-polarization is measured at different instants and things might have already changed with rotation [125]. Fig.5.3 shows these polarimetric ratios for the same case in Fig.5.2. It can be observed from Fig.5.3 that backscattering is slightly higher in HH case than in VV case for most of the azimuth angles. It can also be seen that the back side has the least cross-polarization ratio when compared with the other sides of the mannequin. The averages of RCS measurements for each side and as well as for the full horizontal rotation at different height sections, namely the head, chest, stomach, thighs, and legs, are tabulated in Table. 5.1. These sections are illustrated in Fig.5.1a. It seems from the measurement sets that we have a very consistent pattern which can be summarized as 1) an RCS value between -16 and -9 dBsm from the trunk of the body is expected at VV. 2) HH response tends to be slightly higher than VV by an average of 1.4 dB. And 3- Cross-polarization is significant (-9 to -15 below co-polarization), which is more apparent from the two sides than it is in the front and back. Also, the cross-polarization level shows a strong dependence on the relative position of the body limbs during the measurement.

The reported measurements in Fig.5.2 and in Tables.5.3 and 5.1 are performed on a mannequin which should represent a good model of the human body at microwave frequencies. To exemplify the reflectivity of human skin, the mannequin was painted with a resistive layer which was then tested at microwave frequencies [126]. In order to verify this validity at MMW frequencies, one measurement was performed on a real person while the radar was pointed at the chest level. The results from this experiment are shown in Table.5.2. The averages of RCS values are off by 4 to 6 dB compared to those from the mannequin; nonetheless, the polarization ratios seem to follow the same behavior for both the mannequin and real person. The difference in RCS values between the two could be explained by the resistive

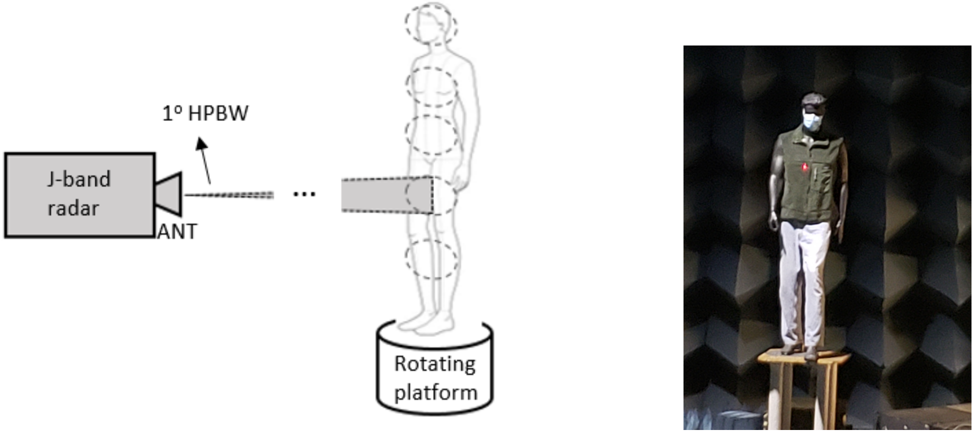

(a) (b)

Figure 5.1: Illustration of the setup for RCS measurements of the mannequin. The radar is placed at 15 m stand by distance from the rotating platform inside anechoic chamber. (a) a sketch to show the measurement setup and where the radar antennas are pointed, different antenna footprints on the mannequin for different experiments are shown. (b) a photo of the mannequin while placed on the rotating platform with the laser is used to guide the radar pointing.

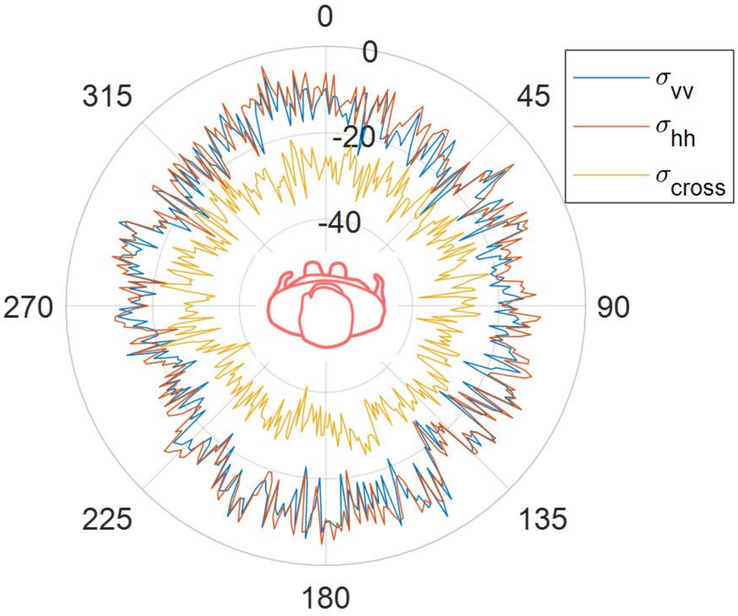

Figure 5.2: Measured radar cross section (RCS) of the mannequin (in dBsm) with the antenna pointed at the chest area and with a beam spot of 31-cm radius. Measurement is taken over the 360 azimuthal angles at 1-degree increment.

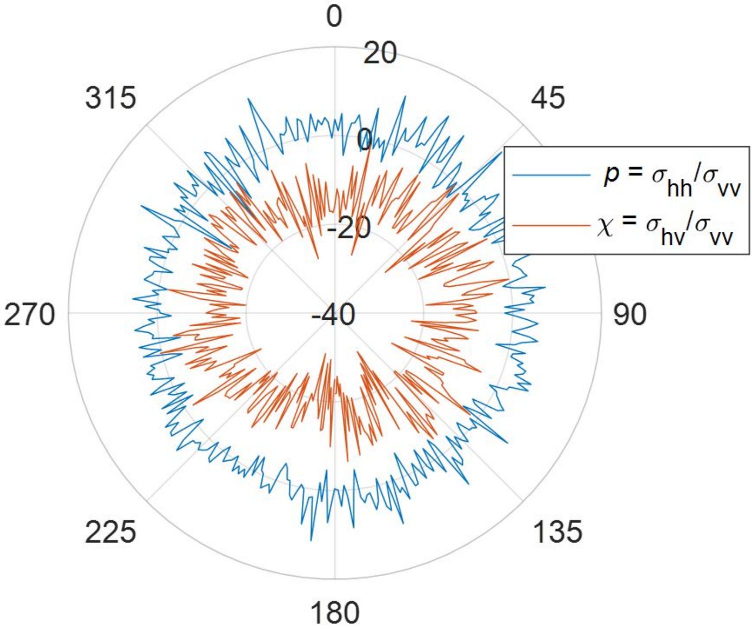

Figure 5.3: Co- and cross-polarization ratio of the backscattering from the mannequin with the antenna pointed at the chest area.

paint's reflectivity being higher than human skin at high MMW frequencies. Also, another factor could be the rather big size of the mannequin that might only represent people in the higher percentile. The dielectric constant of human skin experiences a strong variation across the frequency band and also shows dependence on the human and the location of the body [127]. The quantification of the dielectric constant is not the focus of this study since it is not the only factor determining the RCS values. The reader is referred to a study on the dielectric constant of human skin and various fabric materials in [128]. Nevertheless, besides the RCS level, all other scattering features have shown good agreement between the mannequin and the person.

Another observation from the experiments conducted was that clothes impact the backscatter response. The mannequin's response without clothes was found to have a significantly weaker cross-polarized backscatter signal compared with the clothed case. Several additional measurements were conducted to examine and interpret the effect of clothes on the response. Figure.5.4 shows the cross-polarization ratio (χ) of the backscatter from a

Table 5.1: Polarimetric RCS Measured Values of the Mannequin at Different Heights

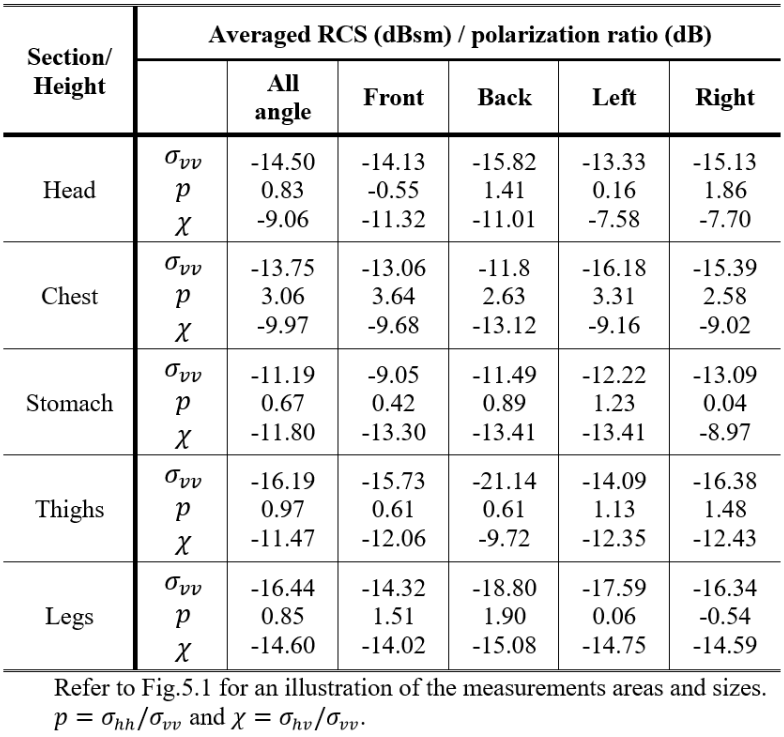

Section/ Height		Averaged RCS (dBsm) / polarization ratio (dB)				
		All angle	Front	Back	Left	Right
Head	σ_{vv}	-14.50	-14.13	-15.82	-13.33	-15.13
	p	0.83	-0.55	1.41	0.16	1.86
	χ	-9.06	-11.32	-11.01	-7.58	-7.70
Chest	σ_{vv}	-13.75	-13.06	-11.8	-16.18	-15.39
	p	3.06	3.64	2.63	3.31	2.58
	χ	-9.97	-9.68	-13.12	-9.16	-9.02
Stomach	σ_{vv}	-11.19	-9.05	-11.49	-12.22	-13.09
	p	0.67	0.42	0.89	1.23	0.04
	χ	-11.80	-13.30	-13.41	-13.41	-8.97
Thighs	σ_{vv}	-16.19	-15.73	-21.14	-14.09	-16.38
	p	0.97	0.61	0.61	1.13	1.48
	χ	-11.47	-12.06	-9.72	-12.35	-12.43
Legs	σ_{vv}	-16.44	-14.32	-18.80	-17.59	-16.34
	p	0.85	1.51	1.90	0.06	-0.54
	χ	-14.60	-14.02	-15.08	-14.75	-14.59

Refer to Fig.5.1 for an illustration of the measurements areas and sizes.
$p = \sigma_{hh}/\sigma_{vv}$ and $\chi = \sigma_{hv}/\sigma_{vv}$.

Table 5.2: Polarimetric RCS Measured Values of a Real Person at the chest Level

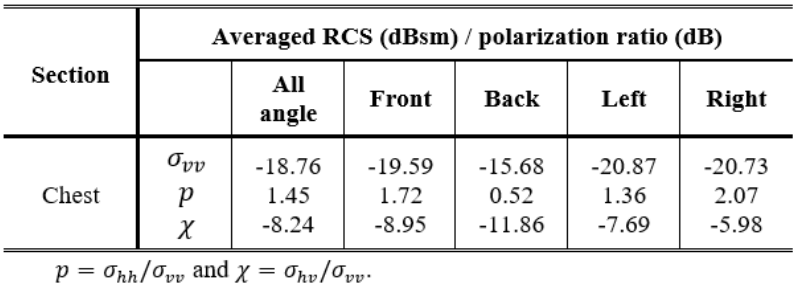

Section		Averaged RCS (dBsm) / polarization ratio (dB)				
		All angle	Front	Back	Left	Right
Chest	σ_{vv}	-18.76	-19.59	-15.68	-20.87	-20.73
	p	1.45	1.72	0.52	1.36	2.07
	χ	-8.24	-8.95	-11.86	-7.69	-5.98

$p = \sigma_{hh}/\sigma_{vv}$ and $\chi = \sigma_{hv}/\sigma_{vv}$.

clothed and unclothed mannequin, in addition to that of a real person. Table-5.3 lists the numeric data of the un-clothed mannequin's response. It is apparent from comparing these results with their counterpart in Table-5.1 (Chest section in the second row) that clothes play an essential role in depolarization. Clothes made from various fabrics were tested, and

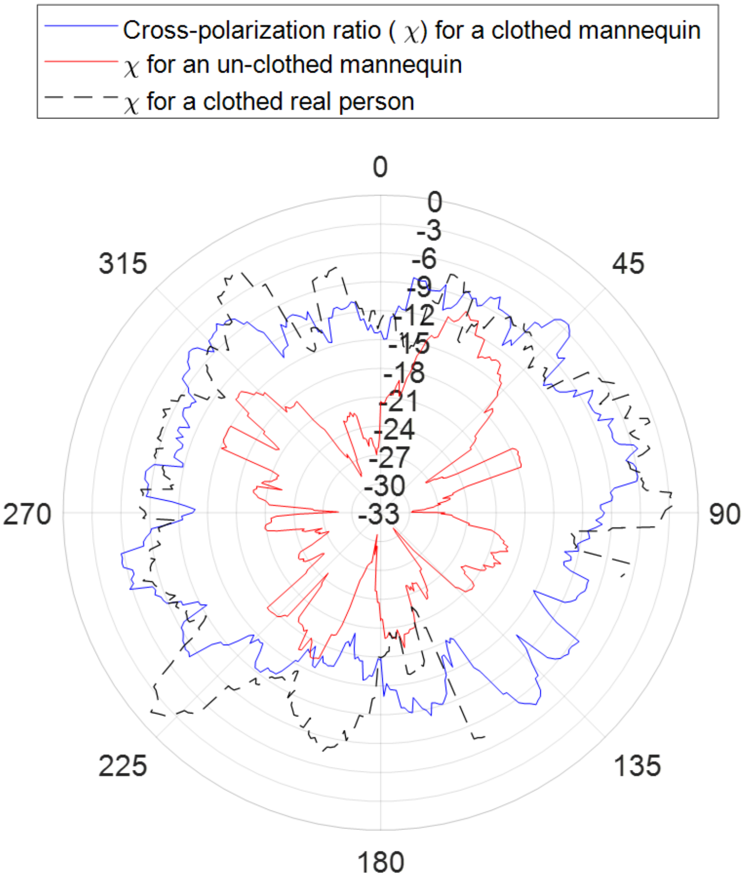

Figure 5.4: Cross-polarization ratio of the backscattering from the mannequin in case of fully clothed and without clothes, and the ratio for real person while clothed.

the range of variation of depolarized RCS is found to be within a 6-dB range. Fabrics of thicker structure and coarser threads showed more substantial depolarization than those with smoother textures. It was also observed that the responses of VV and HH depend on the orientation of fabric threads. This is explained by the threads acting like a grid that affects polarization of the propagating signal. The threads in some cases are spaced by about 1 mm, which is comparable to the wavelength ($\lambda = 1.35mm$); hence, these features are observable. In conclusion, the depolarization level in the response from a dressed human is considerable, a feature that has not been observed in any other targets. This feature can be useful in recognizing the presence of a person in the scene.

The comparative rather than quantitative measurement of the response in radar polarime-

Table 5.3: Polarimetric RCS Measured Values of the Mannequin without clothes.

Case	Averaged RCS (dBsm) / polarization ratio (dB)					
		All angle	Front	Back	Left	Right
Manikin without clothes	σ_{vv}	-11.54	-9.80	-11.06	-13.27	-12.99
	p	0.68	2.85	-0.31	0.10	-0.98
	χ	-18.96	-16.34	-21.49	-18.89	-21.14

try is less prone to signal alterations by the environment and status of the sensor hardware. Statistical-based detection also has this same advantage without the need for extra circuitry. The scattered signal from human consists of many scatterings from various body parts, and the coherent summation of these scatterings is the overall response. Any slight alteration in the object would change both amplitudes and phases of these scatterings and, therefore, the overall response in a random-like manner. This behavior was apparent in the presented RCS maps for human bodies. The statistical variations in the response depend on the physical object as well as the orientation and distance with respect to the radar. Characterization of the fluctuation in backscattering from an object through a statistical model is a useful tool in the identification of that object [129]. However, the forward backscattering problem to formularize the variation in the response is highly complicated, and the inverse problem of extracting the statistical behavior from measured responses is feasible. Many standard probability density function (PDF) distributions have been used to formularize the RCS fluctuations of different objects, and each of which depends on how many scatterings are contributing to the overall response, their relation, and the weight of each. In order to characterize the response by one of the standard statistical distributions, the empirical cumulative density function (ECDF) for the collected data set is compared with the cumulative density function (CDF) of various standard distributions, and the CDF with minimum error is chosen as described in more details in Chapter-III.

The results of the search show that Lognormal distribution provided the best fit for the collected data with close parameters values for different cases and polarization states. The PDF of the Lognormal distribution is given by the function:

$$f(x;\nu,\tau) = \frac{1}{x\tau\sqrt{2\pi}}\ \exp -(\frac{(\ln x - \nu)^2}{2\tau^2}) \tag{5.1}$$

The random variable $(\ln x)$ is normally distributed with mean and variance ν and τ, respectively, thus the name. For the random variable x denoting RCS values, the mean and variance are given by:

$$mean = e^{\nu+\tau^2/2} \tag{5.2}$$

$$variance = e^{2\nu+\tau^2}\ (e^{\tau^2} - 1) \tag{5.3}$$

The parameter τ is commonly named the shape parameter, while ν is called the scale or location parameter of the PDF [129]. Table-5.4 shows the best-fit parameters for each case of our measurements. To show the usefulness of the statistical characterization of targets, Fig.5.5 shows the distinction in parameters of the Lognormal distribution for vehicles and humans. As presented in Chapter III, it was found that Weibull PDF is better at characterizing vehicles' RCS fluctuation. There, a complete model for Weibull parameters was presented based on the distance to the vehicle or the size of the spot on the vehicle illuminated by the radar. Lognormal also came relatively close to some of the data sets collected for vehicles (Fig. 3.15). Here for the purpose of comparison, backscattering data from both vehicles and humans were both fitted to Lognormal distribution. The vehicle data in Fig.5.5 are chosen for full illumination of the car horizontally and only about 40 cm section in height. This is analogous to the human setup where only a limited height section is illuminated. A closer look into the PDF based on one data set of a human against another of a vehicle is shown in Fig. 5.6. The variation in the RCS of the human in Fig. 5.6 is

Table 5.4: Fitted Lognormal Distribution Paramaters for Different Data Sets.

Measurements	**PDF parameters**	**Polarization**		
		VV	**HH**	**HV**
Real person Chest level	ν	-4.91	-4.95	-7.79
	τ	1.05	1.07	1.05
Manikin Head	ν	-3.86	-4.04	-6.79
	τ	1.03	0.96	0.93
Manikin Chest	ν	-3.71	-3.35	-6.82
	τ	1.08	1.06	0.89
Manikin Stomach	ν	-3.04	-3.18	-6.61
	τ	0.98	1.03	0.92
Manikin Thighs	ν	-4.32	-4.42	-7.65
	τ	1.10	1.15	0.91
Manikin Legs	ν	-4.41	-4.59	-8.44
	τ	0.98	0.92	0.81
Manikin without clothes - Chest	ν	-3.39	-3.58	-8.93
	τ	1.30	1.24	0.95

modeled by a Lognormal distribution ($\nu = -3.71, \tau = 1.08$), while the vehicle's variations follow Weibull distribution ($\lambda = 6.58, \beta = 0.98$). A simulation based on these parameters is carried out to examine the number of independent measurements needed to identify a human from a vehicle based on statistics of the variation in the response of each. With only ten measurements of a vehicle it is possible to identify it with a success rate better than 98%. While a perfect identification of a human against a car was possible with only five independent measurements. The ability to distinguish between responses of vehicles from those of humans shows good potential for identification based on statistical characterization of the backscatter response in more complex scenarios.

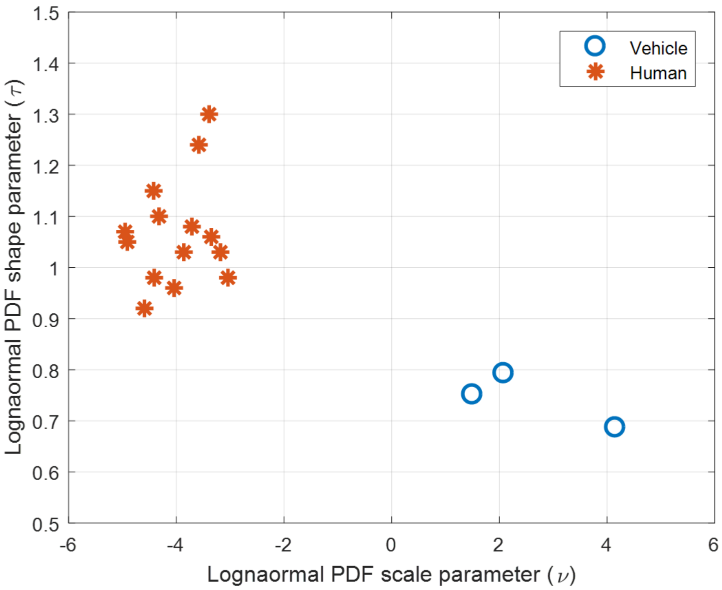

Figure 5.5: Comparison between the parameters of Lognormal distribution characterizing the response from vehicles and human subjects. The data for vehicles were collected with full horizontal radar illumination and 35-cm in vertical. It should also be noted that human data were collected from all directions while vehicles were only observed from the back.

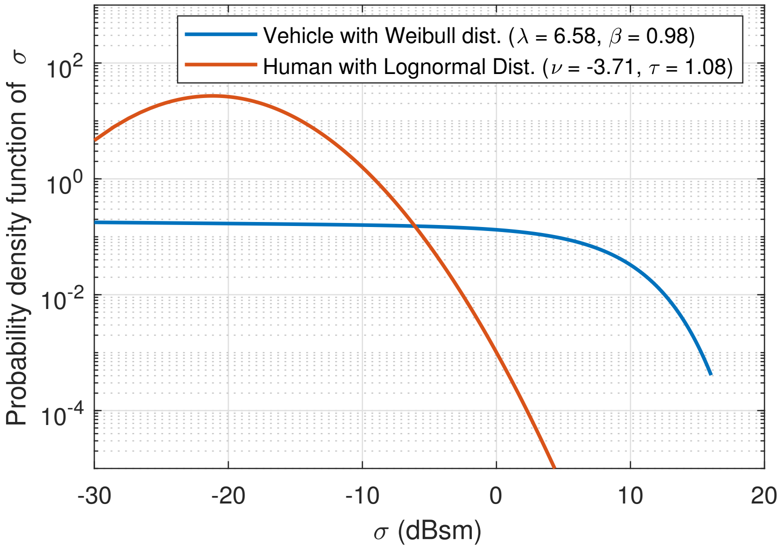

Figure 5.6: Probability density function (PDF) of the variation in RCS measurements in one data set of a human and another of a vehicle. The data of a human is modeled by a Lognormal distribution, while the vehicle's variations follow Weibull distribution.

5.4 Micro-Doppler Spectrum of Moving Humans at J-Band

The experimental characterization of the micro-Doppler signature of humans is discussed in this section. The term micro-Doppler is usually referred to the components of the Doppler frequency spectrum due to the movements of various parts of the target of interest. For example, the swinging arms and alternating feet result in many micro-Doppler components with specific features. These features are unique and distinct not only from the Doppler response of a rigid moving object (like a car) but even from the motion response of a quadruped, for instance. In order to experimentally characterize the motion response of humans, the FMCW radar instrument is utilized. To achieve a high resolution for Doppler frequency measurement, multiple FMCW waveforms are employed to extract the spectrum. Doppler information is embedded in the phase progression over many consecutive FMCW chirps. Therefore, observing over a more extended chirp sequence provides finer resolution. To illustrate the process of extracting the Doppler spectrum of a target, Fig.?? shows different steps for the generation of what is called the Range-Doppler map. In the receiver of FMCW radars, the received signal is essentially a delayed and scaled version of the transmitted signal at that instant [130]. When a sample of the latter is mixed with the received signal, the result is the beat signal which has a frequency proportional to the delay time (and the range to the target). Measurement of the radar return of a single FMCW chirp is sufficient to extract the range through Fourier transformation of the beat signal to the frequency domain. The response in the frequency domain is a single component at the beat frequency which is related to the range to the target by:

$$r = \frac{T_{chirp}}{BW}\ \frac{c}{4} f_{beat} \tag{5.4}$$

Where r is the one-way distance to the target, T_{chirp} is the time for frequency sweep (up and down), BW is the sweeping frequency bandwidth, f_{beat} is the beat frequency, and c is the

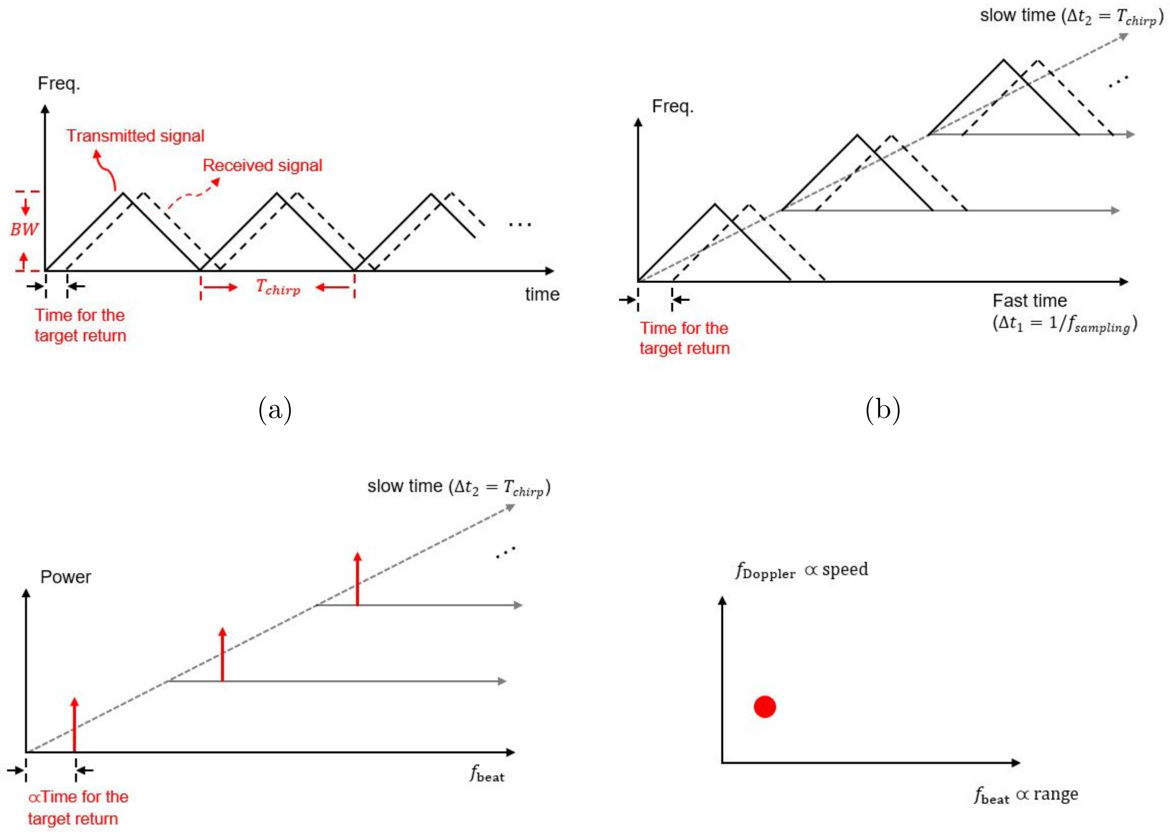

(a) (b)

(c) (d)

Figure 5.7: Processing steps of a sequence of radar FMCW waveforms for Range-Doppler map. (a) The received and transmitted signals. (b) Introducing a third dimension (slow-time) represented by various chirps. (c) Information of the range are extracted from the beat signal resulted from mixing the received signal with a sample of the transmitted signal. (d) Performing Fourier transformation over the slow time for each range cell results in the Doppler spectrum at that range.

speed of light. Any motion in the target will also embed the frequency Doppler shift in the beat frequency, but however, for our purpose and with a short chirp time, this has negligible effect. By employing a sequence of FMCW waveforms as a third dimension, as shown in Fig.?? (b) and (c), the Fourier transformation over the new time domain (commonly named slow-time domain) provides the Doppler response across each range cell. This transformation has the following properties: 1) the phase progression of a moving target along the slow-time domain (t_2) is

$$\phi_n = k(2vt_2) = 2(\frac{2\pi}{\lambda})nT_{chirp}v \tag{5.5}$$

Where $k = 2\pi/\lambda$ is the propagation constant, v denotes speed components of the target, n is the index of the FMCW chirp. 2) the phase relationship above shows the characteristics of the Fourier transformation pair between speed and slow-time domains which has maximum unambiguous speed:

$$v_{max} = \frac{\lambda}{2}\,\frac{1}{2\,T_{chirp}} \tag{5.6}$$

3) the resolution of speed is inversely proportional to the time of measurement:

$$\Delta v = \frac{1}{N\,T_{chirp}} = \frac{1}{T_{measurement}} \tag{5.7}$$

Operating at the higher MMW band has very Doppler frequency sensitivity knowing that ($f_{Doppler} = 2v/\lambda$). In addition, such frequencies offer the very desirable narrow beamwidth with a reasonable size of the antenna. However, the narrow beamwidth necessitates performing the measurements at a longer stand-by distance from the radar to ensure full illumination and hence capture the response of the whole body. The micro-Doppler spectrum of a moving human and its various properties was examined experimentally using the FMCW instrument. This system has a narrow beamwidth (1 degree), and for the antenna beam to illuminate an average human body, it has to be about 100 meters away. Measurement at such a large

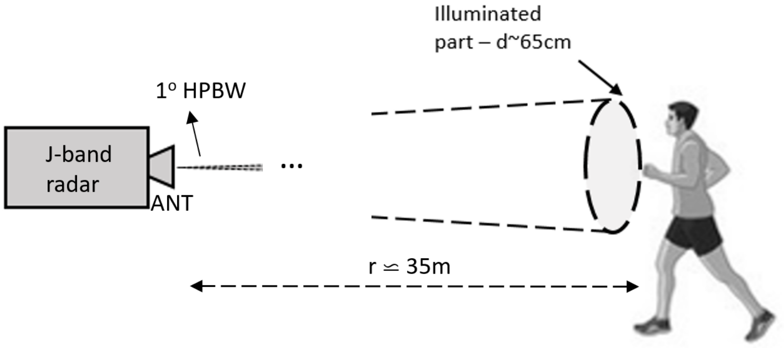

Figure 5.8: Illustration of the measurements setup of the Doppler spectrum of a moving person. The distance to the radar is about 35-meters and the radar beam has a radius of 65-cm. Only the upper half of the person is observed.

distance has limited SNR, especially with conducting short chirps. In addition, ensuring that the person under measurement is within the antenna beam at that long distance and with his movement is quite challenging. Therefore, it is decided to focus on the upper part of the body. At a measurement distance of 35 meters, the radar beam size has a radius of about 65 cm, which is more than the width of an average person, including his arms' movement. Figure.5.8 shows the measurement setup. Another key element in the Doppler measurement is the chirp time. To acquire higher speed components unambiguously, chirp time should be minimized, as indicated in (5.6). Practically, the issue of linearity usually sets a minimum bound for the chirp time. In the measurements performed, the chirp-up time was set to be 12.9 microseconds. This permits measuring speeds up to pm 12.86 m/s (46.3 km/hour). Also, (5.7) indicates that the Doppler measurement resolution is determined by the number of chirps collected given a predetermined chirp time. As long as the challenging task of maintaining coherence in the system is met, the memory available to store data is what limits the measurement time. In the experiments conducted, 4000 chirps are collected coherently, achieving a Doppler frequency resolution of 9.7 Hz, equivalent to a speed resolution of 0.0064 m/s.

The micro-Doppler response of a running person is shown in the range-Doppler map in Fig.5.9(a). The extension of the response over a wide Doppler (speed) spectrum range contains information specific to the movement. In Fig.5.9(b), where the data for a cut across the Doppler spectrum at the person's range is shown, the micro-Doppler response and the levels of various components can be observed. It can be seen that the average speed is 3.4 m/s; however, the micro-Doppler components expand over a 2.25 m/s span (equivalent to 3.4 kHz bandwidth). The micro-Doppler response for cross-polarization for the same measurement is presented in Fig.5.10. When compared with Fig.5.9(b), aside from the lower response level around the center of the response, which is primarily due to the body's trunk, the response is less sharper than that of like-polarization. The micro-Doppler response at cross-polarization shows distinct features around its spectrum edges, for which the person's limbs are responsible. This observation agrees with the finding in section 5.3 and shows more advantages of cross-polarization when the detection of humans is concerned. The example shown is for a running person; similar features were found in the case of a walking person with a slightly narrower spectrum given the more settled movements in that case.

Micro-Doppler signature-based recognition and identification is the topic for many research efforts [131, 132, 133, 134, 135, 136]. Many approaches have been proposed for the identification that includes extracting various features in the response and associating them with the physical movement. The periodical micro-Doppler response of a human gait can be visually interpreted, and its mono-components can be linked to the actual physical movements [137]. However, performing this interpretation computationally is more challenging. One of the most promising techniques is exploring the periodical response to extract its statistical information. In this section, an initial study is presented while the effort is expected to be continued pending some upgrades to the instrumentation system, which will be discussed shortly. The micro-Doppler response change over the short period of measurement time for the same experiment presented in Figs. 5.9 and 5.10 is shown in Fig.5.11. This data consists of 20 frames that are 5.2 milliseconds long and thus have about 200 Hz resolution. The overall time of the measurement is 0.12 seconds which is clearly not sufficient to capture

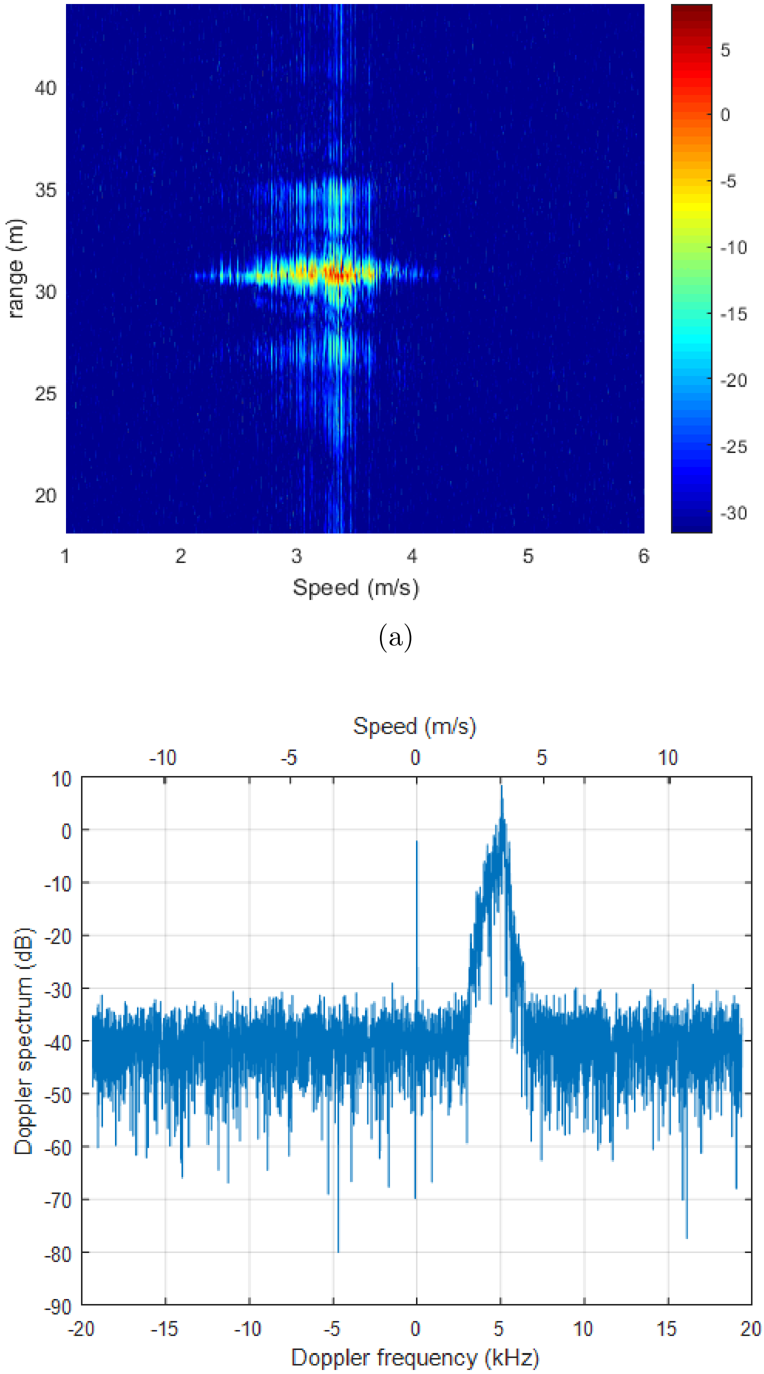

(a)

(b)

Figure 5.9: The micro-Doppler response at VV-polarization for a person running toward the radar. The measurement is performed at 32-m range and only the upper half of the person is observed. (a) The range-Doppler map of the response. (b) cut across the micro-Doppler response at the person's range.

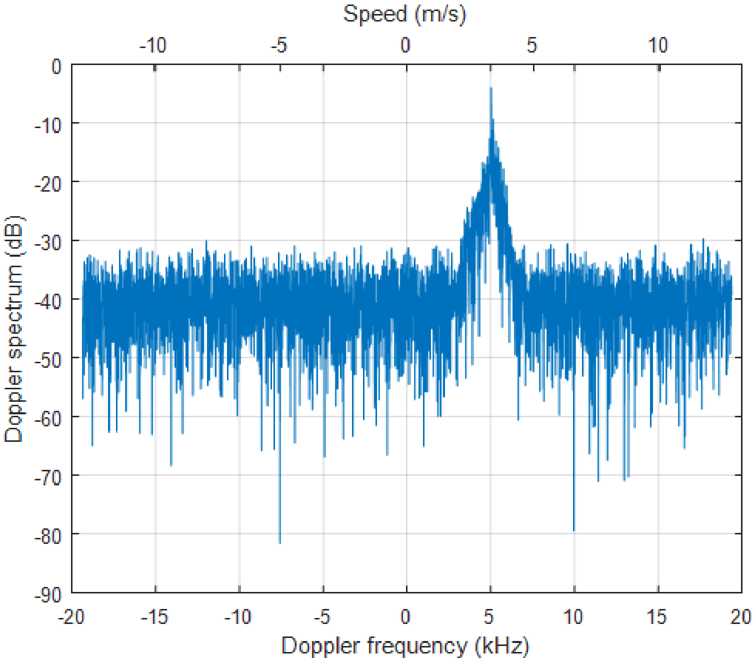

Figure 5.10: The micro-Doppler response at HV-polarization for a person running toward the radar.

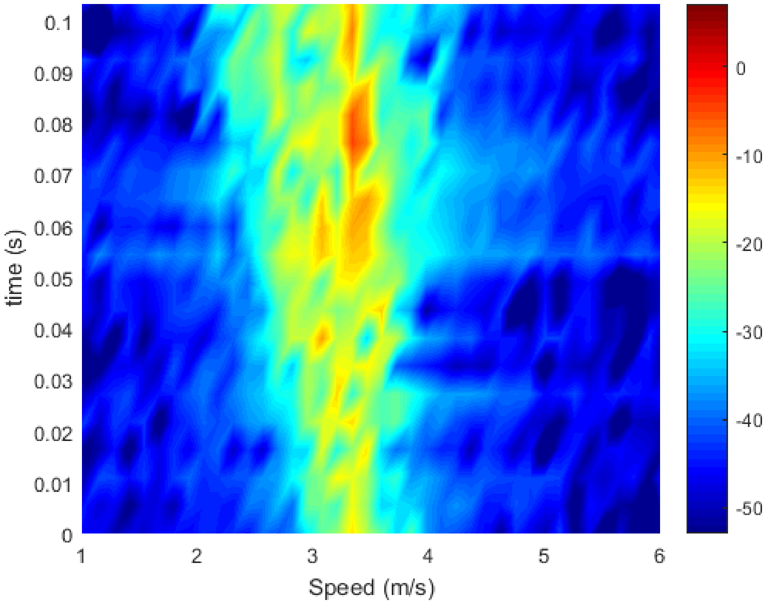

Figure 5.11: Micro-Doppler spectrum of human gait for 20 consecutive frames and overall time of 0.12 seconds (VV-polarization).

even one period of the human gait. However, it is expected from radars to perform detection and identification in at most tens of milliseconds to surpass the human reaction, which is averaged about half a second [138]. Moreover, even over such a short period of time, certain features of the response are apparent and unique to human movements. For example, the data in the Time-Doppler response of Fig.5.11 show a relatively wide spectrum response, therefore the spectrum span (bandwidth), the standard deviation of frequency components, or the power-weighted standard deviation of the micro-Doppler spectrum components in the response can be used to distinguish humans from other targets. The last feature emphasizes the stronger response of the body trunk hence it is more effective for like-polarization, while the other two are more beneficial for cross-polarization where the response is more distributed. A rigid target like a vehicle should have an extremely narrow spectrum span. Measurements over longer times for both a human and a vehicle are shown in Fig. 5.12 and Fig. 5.13 where the distinct in the response is very apparent. A complete study of the human gait features is planned for the future along with examining the micro-Doppler response from a bicycle and other quadrupeds to extract more specific features that permits the identification of each case. At this time, the FMCW system is being upgraded to be able to collect data for longer periods of times, and its antenna is modified sch that multiple size of lenses can be used to adjust the beamwidth. This will permit the illumination of the whole body of the moving person, therefore including more components from the person's legs and bottom half. In addition, the FMCW triangular frequency sweeps will be changed to a saw-tooth shape and thus reducing the chirp time to its half. This will allow capturing double the current maximum speeds.

5.5 Conclusions

This chapter dealt with the radar backscattering from human subjects. The range of RCS values of a person as observed from different look angles and the polarimetry of the scat-

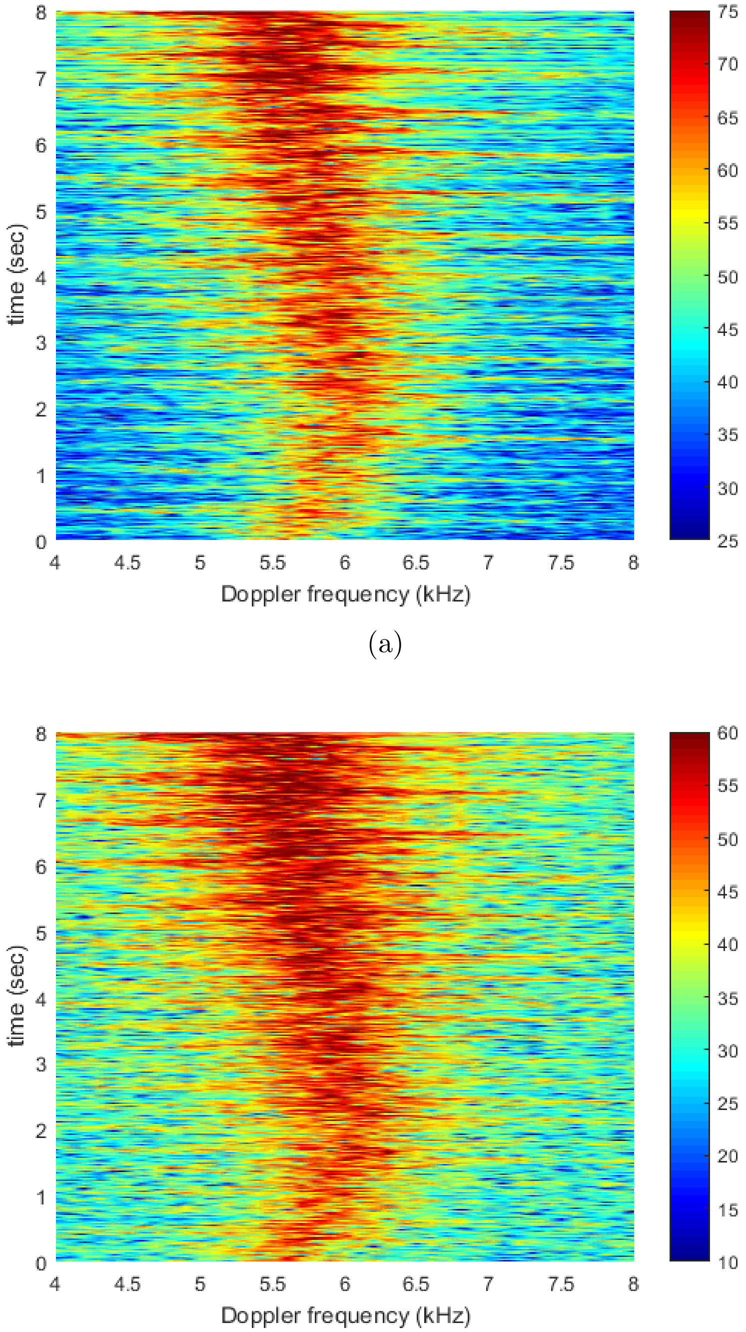

(a)

(b)

Figure 5.12: Micro-Doppler spectrum of human gait for 800 consecutive frames with 10 msec long each and an overall time of 8 seconds (a) VV-polarization and (b) HV-polarization.

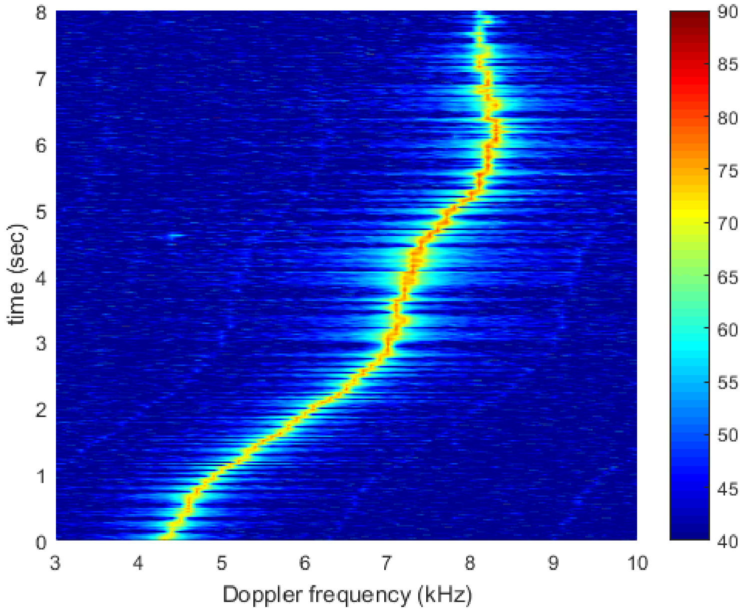

Figure 5.13: Micro-Doppler spectrum of a vehicle for 800 consecutive frames with 10 msec long each and an overall time of 8 seconds (VV-polarization).

tering were both examined and reported. The response from a human was found to have a substantial depolarization level. An investigation found that most of this depolarization is attributed to clothes. In addition, the measured response exhibits a strong variation in response to changing the look angle. This fluctuation in response statistically follows Lognormal distribution with specific parameters. Based on the statistical behavior of the response, simulations showed that a human could be identified against a vehicle with as minimum as five measurements. The micro-Doppler signature of a moving person was also considered for effectively identifying humans from other targets, given their unique response features.

CHAPTER VI

Conclusions and Future Works

This thesis focused on studying the radar backscatter response of typical objects encountered in traffic scenes at J-band frequencies. Identifying various targets on the road is critical for autonomously planning and navigating the driving path. Therefore, characterization of the polarimetric radar backscatter from three important categories is the subject of the dissertation. The thorough studying of the response from vehicles, road surfaces, and human subjects and the examination of various radar features that permits their identification that was reported is essential for optimizing both hardware and algorithms used in automotive sensors operating at J-band.

For vehicles, specific attention was devoted to identifying sources of scattering from vehicles at this frequency, along with the statistical properties of the backscattered return. High-resolution outdoor measurements of stationary vehicles were performed using the synthetic aperture radar imaging technique. Additional complimentary measurements of the same targets were performed at close range, and 3-D images were constructed with the radar operating in real-aperture mode. It was found that the significant scattering is from a limited number of strong scattering phase-centers whose location and strength varied based on both polarization and relative look angle. Most of the scattering is from the outer surfaces of the vehicles facing the radar, and some scattering appears to be from the bottom surface of the vehicle after it undergoes specular reflections off of the road surface. In the experiments reported in Chapter III, no scattering from the interior of vehicles was observed. For the co-polarized response, specular reflections were dominating, and therefore they were sensitive to the relative look angle. At near 0° look-angle the scattering phase-centers were almost the same for all vehicles that were examined. However, they were different from one vehicle to another for the cross-polarized case. The statistics associated with scattering from vehicles are a function of both the relative look angle and the illuminated area of the vehicle at any instant of time. However, it was found that the Weibull distribution was able to fit the measured data in most cases with a shape parameter that varies with the illuminated spot size of the vehicle.

The focus of Chapter IV was on investigating and characterizing the radar backscatter response from various road surfaces at J-band. Scattering models were developed and tested against experimental data that was collected for many road surfaces. The polarimetric response from road surfaces, particularly at near-grazing incidence angles (between 80 and 88^o), is studied for road surface recognition. The knowledge of the expected radar signal level is not only useful to design detection algorithms for other objects in the presence of this background but also for mapping the road, detecting harmful objects and debris, and assessing the road condition. Surfaces that are wet, ice-covered, or snow-covered were also examined and characterized. The backscatter response from road surfaces was explained by a combination of both volume and surface scatterings. To characterize the volume scattering, a model based on the vector radiative transfer theory was formulated. The integral equation method (IEM) provides excellent agreement with experimental data for surface scattering.

Radar backscatter response from human subjects was also examined for its radar cross-section and polarization signature. Some unique features were observed, including a substantial depolarized response from a human. It was found that most of the depolarization is attributed to the clothes as it almost disappears in their absence. The measured response exhibits a strong variation given the immense size compared with the wavelength at J-band. These variations were found to be best statistically modeled by lognormal distribution with specific parameters. The statistical behavior of the response permit identifying a human against a vehicle with only five measurements with nearly a perfect identification success rate. A vehicle can be identified with a success rate better than 98% with as low as ten independent measurements. In addition, an initial study was conducted to observe the micro-Doppler response of a moving person. This effort is expected to continue for a more inclusive analysis and experimentation.

The thesis provided initial studies for effective detection and identification techniques based on various targets' responses and their distinct features.

The radar backscatter responses from various objects discussed in this thesis were examined and tested under controlled experimental setups. In real scenarios, objects might be close in location and speed such that their responses are not easily separable. Moreover, objects on roads are not limited to the three categories discussed in this thesis. Therefore, a more realistic examination of the proposed models and techniques is an expected extension to the studies performed. The response of many other objects is also recommended, including bicycles, traffic signs, traffic signals, light posts, trees, roadside guard rails, and other objects that might be encountered in a road environment. An inclusive study would allow the radar to process the majority of backscatter signals and detect any unusual objects along the road.

BIBLIOGRAPHY

[1] Klaus Bengler, Klaus Dietmayer, Berthold Farber, Markus Maurer, Christoph Stiller, and Hermann Winner. Three decades of driver assistance systems: Review and future perspectives. *IEEE Intelligent Transportation Systems Magazine*, 6(4):6–22, 2014.

[2] SAE International. *Taxonomy and Definitions for Terms Related to Driving Automation Systems for On-Road Motor Vehicles*, 2021.

[3] Makoto Satoh and Shuji Shiraishi. Performance of antilock brakes with simplified control technique. In *SAE International Congress and Exposition*. SAE International, feb 1983.

[4] M. Aga and A. Okada. Analysis of vehicle stability control (vsc)'s effectiveness from accident data. *Proceedings: International Technical Conference on the Enhanced Safety of Vehicles*, 2003:7 p.–7 p., 2003.

[5] MarkVollrath, Susanne Schleicher, and Christhard Gelau. The influence of cruise control and adaptive cruise control on driving behaviour – a driving simulator study. *Accident Analysis and Prevention*, 43(3):1134–1139, 2011.

[6] W.D. Jones. Keeping cars from crashing. *IEEE Spectrum*, 38(9):40–45, 2001.

[7] International Standard Organization. *Intelligent transport systems — Adaptive cruise control systems — Performance requirements and test procedures, 15622 ISO/TC204*, 2018.

[8] Vipin Kumar Kukkala, Jordan Tunnell, Sudeep Pasricha, and Thomas Bradley. Advanced driver-assistance systems: A path toward autonomous vehicles. *IEEE Consumer Electronics Magazine*, 7(5):18–25, 2018.

[9] Azim Eskandarian. *Introduction to Intelligent Vehicles*, pages 1–13. Springer London, London, 2012.

[10] S. Ishida and J.E. Gayko. Development, evaluation and introduction of a lane keeping assistance system. In *IEEE Intelligent Vehicles Symposium, 2004*, pages 943–944, 2004.

[11] André Benine-Neto, Stefano Scalzi, Saïd Mammar, and Mariana Netto. Dynamic controller for lane keeping and obstacle avoidance assistance system. In *13th International IEEE Conference on Intelligent Transportation Systems*, pages 1363–1368, 2010.

[12] Benjamin Ranft and Christoph Stiller. The role of machine vision for intelligent vehicles. *IEEE Transactions on Intelligent Vehicles*, 1(1):8–19, 2016.

[13] Robin Schubert, Karsten Schulze, and Gerd Wanielik. Situation assessment for automatic lane-change maneuvers. *IEEE Transactions on Intelligent Transportation Systems*, 11(3):607–616, 2010.

[14] Muhammad Ishfaq Hussain, Shoaib Azam, Dr. Aasim Rafique, Dr. Ahmad Muqeem Sheri, and Moongu Jeon. Drivable region estimation for self-driving vehicles using radar. *IEEE Transactions on Vehicular Technology*, pages 1–1, 2022.

[15] Khadige Abboud, Hassan Aboubakr Omar, and Weihua Zhuang. Interworking of dsrc and cellular network technologies for v2x communications: A survey. *IEEE Transactions on Vehicular Technology*, 65(12):9457–9470, 2016.

[16] Wenjie Song, Yi Yang, Mengyin Fu, Fan Qiu, and Meiling Wang. Real-time obstacles detection and status classification for collision warning in a vehicle active safety system. *IEEE Transactions on Intelligent Transportation Systems*, 19(3):758–773, 2018.

[17] Xiao Wang, Linhai Xu, Hongbin Sun, Jingmin Xin, and Nanning Zheng. On-road vehicle detection and tracking using mmw radar and monovision fusion. *IEEE Transactions on Intelligent Transportation Systems*, 17(7):2075–2084, 2016.

[18] Zhiqing Wei, Fengkai Zhang, Shuo Chang, Yangyang Liu, Huici Wu, and Zhiyong Feng. Mmwave radar and vision fusion for object detection in autonomous driving: A review. *Sensors*, 22(7), 2022.

[19] Juergen Dickmann, Nils Appenrodt, Jens Klappstein, Hans-Ludwig Bloecher, Marc Muntzinger, Alfons Sailer, Markus Hahn, and Carsten Brenk. Making bertha see even more: Radar contribution. *IEEE Access*, 3:1233–1247, 2015.

[20] Transitioning to tesla vision. Tesla, May 25, 2021 [Online].

[21] Florian Engels, Philipp Heidenreich, Abdelhak M. Zoubir, Friedrich K Jondral, and Markus Wintermantel. Advances in automotive radar: A framework on computationally efficient high-resolution frequency estimation. *IEEE Signal Processing Magazine*, 34(2):36–46, 2017.

[22] M.E. Russell, A. Crain, A. Curran, R.A. Campbell, C.A. Drubin, and W.F. Miccioli. Millimeter-wave radar sensor for automotive intelligent cruise control (icc). *IEEE Transactions on Microwave Theory and Techniques*, 45(12):2444–2453, 1997.

[23] Martin Schneider. Automotive radar: Status and trends. In *In Proceedings of the German Microwave Conference GeMIC 2005*, pages 144–147, 2005.

[24] Kun-Yi Guo, Edward G. Hoare, Donya Jasteh, Xin-Qing Sheng, and Marina Gashinova. Road edge recognition using the stripe hough transform from millimeter-wave radar images. *Trans. Intell. Transport. Sys.*, 16(2):825–833, apr 2015.

[25] Dominik Kellner, Michael Barjenbruch, Jens Klappstein, Jürgen Dickmann, and Klaus Dietmayer. Tracking of extended objects with high-resolution doppler radar. *IEEE Transactions on Intelligent Transportation Systems*, 17(5):1341–1353, 2016.

[26] Jürgen Hasch, Eray Topak, Raik Schnabel, Thomas Zwick, Robert Weigel, and Christian Waldschmidt. Millimeter-wave technology for automotive radar sensors in the 77 ghz frequency band. *IEEE Transactions on Microwave Theory and Techniques*, 60(3):845–860, 2012.

[27] Sujeet Milind Patole, Murat Torlak, Dan Wang, and Murtaza Ali. Automotive radars: A review of signal processing techniques. *IEEE Signal Processing Magazine*, 34(2):22–35, 2017.

[28] Igal Bilik, Oded Bialer, Shahar Villeval, Hasan Sharifi, Keerti Kona, Marcus Pan, Dave Persechini, Marcel Musni, and Kevin Geary. Automotive mimo radar for urban environments. In *2016 IEEE Radar Conference (RadarConf)*, pages 1–6, 2016.

[29] M. Murad, I. Bilik, M. Friesen, J. Nickolaou, J. Salinger, K. Geary, and J. S. Colburn. Requirements for next generation automotive radars. In *2013 IEEE Radar Conference (RadarCon13)*, pages 1–6, 2013.

[30] Shunqiao Sun, Athina P. Petropulu, and H. Vincent Poor. Mimo radar for advanced driver-assistance systems and autonomous driving: Advantages and challenges. *IEEE Signal Processing Magazine*, 37(4):98–117, 2020.

[31] N. Kees, E. Schmidhammer, and J. Detlefsen. Improvement of angular resolution of a millimeterwave imaging system by transmitter location multiplexing. In *IEEE NTC,Conference Proceedings Microwave Systems Conference*, pages 105–108, 1995.

[32] Y. Asano, S. Ohshima, T. Harada, M. Ogawa, and K. Nishikawa. Proposal of millimeter-wave holographic radar with antenna switching. In *2001 IEEE MTT-S International Microwave Sympsoium Digest (Cat. No.01CH37157)*, volume 2, pages 1111–1114 vol.2, 2001.

[33] E. Fishler, A. Haimovich, R. Blum, D. Chizhik, L. Cimini, and R. Valenzuela. Mimo radar: an idea whose time has come. In *Proceedings of the 2004 IEEE Radar Conference (IEEE Cat. No.04CH37509)*, pages 71–78, 2004.

[34] Andreas Stelzer, Reinhard Feger, and Martin Jahn. Highly-integrated multi-channel radar sensors in sige technology for automotive frequencies and beyond. In *2010 Conference Proceedings ICECom, 20th International Conference on Applied Electromagnetics and Communications*, pages 1–11, 2010.

[35] Jürgen Hasch. The rising wave of millimeter-wave sensing. IPCEI on Microelectronics website, October 6, 2020 [Online].

[36] I. Gresham, N. Jain, T. Budka, A. Alexanian, N. Kinayman, B. Ziegner, S. Brown, and P. Staecker. A compact manufacturable 76-77-ghz radar module for commercial acc

applications. *IEEE Transactions on Microwave Theory and Techniques*, 49(1):44–58, 2001.

[37] M. Camiade, D. Domnesque, P.F. Alleaume, A. Mallet, D. Pons, and H. Dambkes. Full mmic millimeter-wave front end for a 76.5 ghz adaptive cruise control car radar. In *1999 IEEE MTT-S International Microwave Symposium Digest (Cat. No.99CH36282)*, volume 4, pages 1489–1492 vol.4, 1999.

[38] Wolfgang Menzel and Arnold Moebius. Antenna concepts for millimeter-wave automotive radar sensors. *Proceedings of the IEEE*, 100(7):2372–2379, 2012.

[39] Christian Waldschmidt, Juergen Hasch, and Wolfgang Menzel. Automotive radar — from first efforts to future systems. *IEEE Journal of Microwaves*, 1(1):135–148, 2021.

[40] Front radar sensor. Bosch, June 8, 2020 [Online].

[41] Claudia Vasanelli, Frank Bögelsack, and Christian Waldschmidt. Reducing the radar cross section of microstrip arrays using amc structures for the vehicle integration of automotive radars. *IEEE Transactions on Antennas and Propagation*, 66(3):1456–1464, 2018.

[42] Front radar premium. Bosch, November 3, 2021 [Online].

[43] Awr1243 sensor: Highly integrated 76–81-ghz radar front-end for emerging adas applications. Texas Instrument, May, 2017 [Online].

[44] Igal Bilik, Shahar Villeval, Daniel Brodeski, Haim Ringel, Oren Longman, Piyali Goswami, Chethan Y. B. Kumar, Sandeep Rao, Pramod Swami, Anshu Jain, Anil Kumar, Shankar Ram, Kedar Chitnis, Yashwant Dutt, Aish Dubey, and Stanley Liu. Automotive multi-mode cascaded radar data processing embedded system. In *2018 IEEE Radar Conference (RadarConf18)*, pages 0372–0376, 2018.

[45] Imaging radar using cascaded mmwave sensor reference design. Texas Instrument, March, 2020 [Online].

[46] Alex Zwanetski, Matthias Kronauge, and Hermann Rohling. Waveform design for fmcw mimo radar based on frequency division. In *2013 14th International Radar Symposium (IRS)*, volume 1, pages 89–94, 2013.

[47] Reinhard Feger, Clemens Pfeffer, and Andreas Stelzer. A frequency-division mimo fmcw radar system using delta-sigma-based transmitters. In *2014 IEEE MTT-S International Microwave Symposium (IMS2014)*, pages 1–4, 2014.

[48] Eun Hee Kim and Ki Hyun Kim. Random phase code for automotive mimo radars using combined frequency shift keying-linear fmcw waveform. *IET Radar, Sonar & Navigation*, 12(10):1090–1095, 2018.

[49] Avik Santra, Alexander Rudolf Ganis, Jan Mietzner, and Volker Ziegler. Ambiguity function and imaging performance of coded fmcw waveforms with fast 4d receiver processing in mimo radar. *Digital Signal Processing*, 97:102618, 2020.

[50] A Hoess. Multifunctional automotive radar network. In *European Conference on Intelligent Road Vehicles, Clermont-Ferrand, France, June, 2001*, 2001.

[51] F. Folster, H. Rohling, and U. Lubbert. An automotive radar network based on 77 ghz fmcw sensors. In *IEEE International Radar Conference, 2005.*, pages 871–876, 2005.

[52] Qian He, Rick S. Blum, and Zishu He. Noncoherent versus coherent mimo radar for joint target position and velocity estimation. In *Proceedings of 2011 IEEE CIE International Conference on Radar*, volume 1, pages 108–111, 2011.

[53] Brett Borden. *Radar Imaging of Airborne Targets: A primer for applied mathematicians and physicists.* CRC Press, 1999.

[54] Ieee standard letter designations for radar-frequency bands. *IEEE Std 521-2019 (Revision of IEEE Std 521-2002)*, pages 1–15, 2020.

[55] Mark Rodwell, E. Lobisser, Mark Wistey, Vibhor Jain, Ashish Baraskar, Erik Lind, J. Koo, B. Thibeault, A. Gossard, Z. Griffith, Jonathan Hacker, and M. Urteaga. Development of thz transistors and (300-3000 ghz) sub-mm-wave integrated circuits. In *WPMC 2008, The 11th International Symposium on Wireless Personal Multimedia Communications, Sept. 8-11, Lapland, Finland.*, 01 2008.

[56] K. Statnikov, J. Grzyb, N. Sarmah, S. Malz, B. Heinemann, and U. R. Pfeiffer. A 240-ghz circularly polarized fmcw radar based on a sige transceiver with a lens-coupled on-chip antenna. *International Journal of Microwave and Wireless Technologies*, 7(3-4):415–423, 2015.

[57] Ingmar Kallfass, Jochen Antes, Thomas Schneider, Fabian Kurz, Daniel Lopez-Diaz, Sebastian Diebold, Hermann Massler, Arnulf Leuther, and Axel Tessmann. All active mmic-based wireless communication at 220 ghz. *IEEE Transactions on Terahertz Science and Technology*, 1(2):477–487, 2011.

[58] K. Sarabandi, M. Vahidpour, M. Moallem, and J. East. Compact beam scanning 240GHz radar for navigation and collision avoidance. In Thomas George, M. Saif Islam, and Achyut K. Dutta, editors, *Micro- and Nanotechnology Sensors, Systems, and Applications III*, volume 8031, pages 318 – 325. International Society for Optics and Photonics, SPIE, 2011.

[59] Armin Jam, Mehrnoosh Vahidpour, Jack East, and Kamal Sarabandi. Microfabricaion and measurement of a sub-millimeterwave beam-scanning antenna array at y-band. In *2014 XXXIth URSI General Assembly and Scientific Symposium (URSI GASS)*, pages 1–2, 2014.

[60] Janusz Grzyb, Konstantin Statnikov, Neelanjan Sarmah, Bernd Heinemann, and Ullrich R. Pfeiffer. A 210–270-ghz circularly polarized fmcw radar with a single-lens-coupled sige hbt chip. *IEEE Transactions on Terahertz Science and Technology*, 6(6):771–783, 2016.

[61] Morteza Abbasi, Sten E. Gunnarsson, Niklas Wadefalk, Rumen Kozhuharov, Jan Svedin, Sergey Cherednichenko, Iltcho Angelov, Ingmar Kallfass, Arnulf Leuther, and Herbert Zirath. Single-chip 220-ghz active heterodyne receiver and transmitter mmics with on-chip integrated antenna. *IEEE Transactions on Microwave Theory and Techniques*, 59(2):466–478, 2011.

[62] Armin Jam and Kamal Sarabandi. A horizontally polarized beam-steerable antenna for sub-millimeter-wave polarimetrie imaging and collision avoidance radars. In *2016 IEEE International Symposium on Antennas and Propagation (APSURSI)*, pages 789–790, 2016.

[63] Meysam Moallem and Kamal Sarabandi. Polarimetric study of mmw imaging radars for indoor navigation and mapping. *IEEE Transactions on Antennas and Propagation*, 62(1):500–504, 2014.

[64] Roger Appleby and Rupert N. Anderton. Millimeter-wave and submillimeter-wave imaging for security and surveillance. *Proceedings of the IEEE*, 95(8):1683–1690, 2007.

[65] DM SHEEN, TE HALL, H SEVERTSEN, et al. Standoff concealed weapon detection using a 350 ghz radar imaging system, passive millimeter-wave imaging technology. *Florida: SPIE Proceedings*, 7670:08, 2010.

[66] Duncan A Robertson, Paul N Marsh, David R Bolton, Robert JC Middleton, Robert I Hunter, Peter J Speirs, David G Macfarlane, Scott L Cassidy, and Graham M Smith. 340-ghz 3d radar imaging test bed with 10-hz frame rate. In *Passive and Active Millimeter-Wave Imaging XV*, volume 8362, page 836206. International Society for Optics and Photonics, 2012.

[67] Holger Quast and Torsten Loffler. 3d-terahertz-tomography for material inspection and security. In *2009 34th International Conference on Infrared, Millimeter, and Terahertz Waves*, pages 1–2. IEEE, 2009.

[68] Jesus Grajal, Alejandro Badolato, Gorka Rubio-Cidre, Luis Ubeda-Medina, Beatriz Mencia-Oliva, Antonio Garcia-Pino, Borja Gonzalez-Valdes, and Oscar Rubinos. 3-d high-resolution imaging radar at 300 ghz with enhanced fov. *IEEE Transactions on Microwave Theory and Techniques*, 63(3):1097–1107, 2015.

[69] Amr A Ibrahim and Kamal Sarabandi. Sub-terahertz dielectric measurement and its application to concealed object detection. *IEEE Transactions on Terahertz Science and Technology*, 5(3):445–455, 2015.

[70] Adib Y. Nashashibi, Amr A. Ibrahim, Samuel Cook, and Kamal Sarabandi. Experimental characterization of polarimetric radar backscatter response of distributed targets at high millimeter-wave frequencies. *IEEE Transactions on Geoscience and Remote Sensing*, 54(2):1013–1024, 2016.

[71] K. Sarabandi, E.S. Li, and A. Nashashibi. Modeling and measurements of scattering from road surfaces at millimeter-wave frequencies. *IEEE Transactions on Antennas and Propagation*, 45(11):1679–1688, 1997.

[72] E.S. Li and K. Sarabandi. Low grazing incidence millimeter-wave scattering models and measurements for various road surfaces. *IEEE Transactions on Antennas and Propagation*, 47(5):851–861, 1999.

[73] K. Sarabandi and E.S. Li. Polarimetric characterization of debris and faults in the highway environment at millimeter-wave frequencies. *IEEE Transactions on Antennas and Propagation*, 48(11):1756–1768, 2000.

[74] K. Sarabandi and E.S. Li. Characterization of optimum polarization for multiple target discrimination using genetic algorithms. *IEEE Transactions on Antennas and Propagation*, 45(12):1810–1817, 1997.

[75] Abdulrahman A. Alaqeel, Amr A. Ibrahim, Adib Y. Nashashibi, Hussein N. Shaman, and Kamal Sarabandi. Experimental characterization of multi-polarization radar backscatter response of vehicles at ¡inline-formula¿ ¡tex-math notation="latex"¿J ¡/tex-math¿¡/inline-formula¿-band. *IEEE Transactions on Intelligent Transportation Systems*, 20(9):3337–3350, 2019.

[76] Seongwook Lee, Byeong-Ho Lee, Jae-Eun Lee, and Seong-Cheol Kim. Statistical characteristic-based road structure recognition in automotive fmcw radar systems. *IEEE Transactions on Intelligent Transportation Systems*, 20(7):2418–2429, 2019.

[77] Bunyo Okumura, Michael R. James, Yusuke Kanzawa, Matthew Derry, Katsuhiro Sakai, Tomoki Nishi, and Danil Prokhorov. Challenges in perception and decision making for intelligent automotive vehicles: A case study. *IEEE Transactions on Intelligent Vehicles*, 1(1):20–32, 2016.

[78] Stefan Brüggenwirth, Marcel Warnke, Simon Wagner, and Kilian Barth. Cognitive radar for classification. *IEEE Aerospace and Electronic Systems Magazine*, 34(12):30–38, 2019.

[79] Albert Huizing, Matijs Heiligers, Bastiaan Dekker, Jacco de Wit, Lorenzo Cifola, and Ronny Harmanny. Deep learning for classification of mini-uavs using micro-doppler spectrograms in cognitive radar. *IEEE Aerospace and Electronic Systems Magazine*, 34(11):46–56, 2019.

[80] Yang Xiao, Liam Daniel, and Marina Gashinova. Image segmentation and region classification in automotive high-resolution radar imagery. *IEEE Sensors Journal*, 21(5):6698–6711, 2021.

[81] Ole Schumann, Jakob Lombacher, Markus Hahn, Christian Wöhler, and Jürgen Dickmann. Scene understanding with automotive radar. *IEEE Transactions on Intelligent Vehicles*, 5(2):188–203, 2020.

[82] A. Nashashibi, K. Sarabandi, and F.T. Ulaby. A calibration technique for polarimetric coherent-on-receive radar systems. *IEEE Transactions on Antennas and Propagation*, 43(4):396–404, 1995.

[83] Fawwaz T. Ulaby and David G. Long. *Microwave radar and radiometric remote sensing.* University of Michigan Press, 2014.

[84] Adib Y. Nashashibi, Badeea Alazem, and Kamal Sarabandi. Fully polarimetrie fmcw instrumentation radar at 228 ghz. In *2017 USNC-URSI Radio Science Meeting (Joint with AP-S Symposium)*, pages 35–36, 2017.

[85] Mark A Richards. *Fundamentals of radar signal processing.* McGraw-Hill Education, 2014.

[86] F.T. Ulaby, A. Nashashibi, A. El-Rouby, E.S. Li, R.D. De Roo, K. Sarabandi, R.J. Wellman, and H.B. Wallace. 95-ghz scattering by terrain at near-grazing incidence. *IEEE Transactions on Antennas and Propagation*, 46(1):3–13, 1998.

[87] M W Long. *Fundamentals of radar signal processing.* MA, USA:Artech House, 2001.

[88] E Jakeman. On the statistics of k-distributed noise. *Journal of Physics A: Mathematical and General*, 13(1):31–48, jan 1980.

[89] Douglas A. Abraham and Anthony P. Lyons. Reliable methods for estimating the ¡formula formulatype="inline"¿¡tex notation="tex"¿k¡/tex¿¡/formula¿-distribution shape parameter. *IEEE Journal of Oceanic Engineering*, 35(2):288–302, 2010.

[90] Frank J Massey Jr. The kolmogorov-smirnov test for goodness of fit. *Journal of the American statistical Association*, 46(253):68–78, 1951.

[91] W. Buller, B. Wilson, L. van Nieuwstadt, and J. Ebling. Statistical modelling of measured automotive radar reflections. In *2013 IEEE International Instrumentation and Measurement Technology Conference (I2MTC)*, pages 349–352, 2013.

[92] L. Tsang and J. A. Kong. Emissivity of half-space random media. *Radio Science*, 11(7):593–598, 1976.

[93] M. Zuniga and J. A. Kong. Active remote sensing of random media. *Journal of Applied Physics*, 51(1):74–79, jan 1980.

[94] Leung Tsang, Jin Au Kong, and Robert T. Shin. *Theory of Microwave Remote Sensing (Wiley Series in Remote Sensing and Image Processing).* Wiley-Interscience, 1985.

[95] R. T. Shin and J. A. Kong. Radiative transfer theory for active remote sensing of a homogenous layer containing spherical scatterers. *Journal of Applied Physics*, 52(6):4221–4230, 1981.

[96] L. Tsang and J. A. Kong. Radiative transfer theory for active remote sensing of half-space random media. *Radio Science*, 13(5):763–773, 1978.

[97] Leung Tsang and Akira Ishimaru. Radiative wave equations for vector electromagnetic propagation in dense nontenuous media. *Journal of Electromagnetic Waves and Applications*, 1(1):59–72, 1987.

[98] L. Tsang, J. A. Kong, and R. T. Shin. Radiative transfer theory for active remote sensing of a layer of nonspherical particles. *Radio Science*, 19(02):629–642, 1984.

[99] B. Wen, L. Tsang, D.P. Winebrenner, and A. Ishimaru. Dense medium radiative transfer theory: comparison with experiment and application to microwave remote sensing and polarimetry. *IEEE Transactions on Geoscience and Remote Sensing*, 28(1):46–59, 1990.

[100] R. West, L. Tsang, and D.P. Winebrenner. Dense medium radiative transfer theory for two scattering layers with a rayleigh distribution of particle sizes. *IEEE Transactions on Geoscience and Remote Sensing*, 31(2):426–437, 1993.

[101] E. P. W. Attema and Fawwaz T. Ulaby. Vegetation modeled as a water cloud. *Radio Science*, 13(2):357–364, 1978.

[102] Yi-Cheng Lin and K. Sarabandi. A monte carlo coherent scattering model for forest canopies using fractal-generated trees. *IEEE Transactions on Geoscience and Remote Sensing*, 37(1):440–451, 1999.

[103] N.S. Chauhan, D.M. Le Vine, and R.H. Lang. Discrete scatter model for microwave radar and radiometer response to corn: comparison of theory and data. *IEEE Transactions on Geoscience and Remote Sensing*, 32(2):416–426, 1994.

[104] Adib Y. Nashashibi, Kamal Sarabandi, Fahad A. Al-Zaid, and Sami Alhumaidi. An empirical model of volume scattering from dry sand-covered surfaces at millimeter-wave frequencies. *IEEE Transactions on Geoscience and Remote Sensing*, 51(6):3673–3682, 2013.

[105] J.R. Kendra, K. Sarabandi, and F.T. Ulaby. Radar measurements of snow: experiment and analysis. *IEEE Transactions on Geoscience and Remote Sensing*, 36(3):864–879, 1998.

[106] J.R. Kendra and K. Sarabandi. A hybrid experimental/theoretical scattering model for dense random media. *IEEE Transactions on Geoscience and Remote Sensing*, 37(1):21–35, 1999.

[107] P.S. Chang, J.B. Mead, E.J. Knapp, G.A. Sadowy, R.E. Davis, and R.E. McIntosh. Polarimetric backscatter from fresh and metamorphic snowcover at millimeter wavelengths. *IEEE Transactions on Antennas and Propagation*, 44(1):58–73, 1996.

[108] Yasuo Kuga, Fawwaz T. Ulaby, Thomas F. Haddock, and Roger D. DeRoo. Millimeter-wave radar scattering from snow 1. radiative transfer model. *Radio Science*, 26(2):329–341, 1991.

[109] Fawwaz T. Ulaby, Thomas F. Haddock, Richard T. Austin, and Yasuo Kuga. Millimeter-wave radar scattering from snow: 2. comparison of theory with experimental observations. *Radio Science*, 26(2):343–351, 1991.

[110] Abdulrahman A. Alaqeel. Temp. *IEEE*, 1(1):1–2, 2022.

[111] Jin Au Kong. *Electromagnetic wave theory.* EMW Publishing, 2008.

[112] Y. Oh, K. Sarabandi, and F.T. Ulaby. An empirical model and an inversion technique for radar scattering from bare soil surfaces. *IEEE Transactions on Geoscience and Remote Sensing*, 30(2):370–381, 1992.

[113] Fawwaz T. Ulaby, Richard K. Moore, and Adrian K. Fung. *Microwave Remote Sensing: Active and Passive, from Theory to Applications: vols. 2-3.* Artech House, 1986.

[114] A.K. Fung, Z. Li, and K.S. Chen. Backscattering from a randomly rough dielectric surface. *IEEE Transactions on Geoscience and Remote Sensing*, 30(2):356–369, 1992.

[115] A. Nashashibi, F.T. Ulaby, and K. Sarabandi. Measurement and modeling of the millimeter-wave backscatter response of soil surfaces. *IEEE Transactions on Geoscience and Remote Sensing*, 34(2):561–572, 1996.

[116] Adrian K. Fung. *Microwave Scattering and Emission Models and their Applications.* Artech House Publishers, 1994.

[117] B. Smith. Geometrical shadowing of a random rough surface. *IEEE Transactions on Antennas and Propagation*, 15(5):668–671, 1967.

[118] K. Sarabandi, F.T. Ulaby, and M.A. Tassoudji. Calibration of polarimetric radar systems with good polarization isolation. *IEEE Transactions on Geoscience and Remote Sensing*, 28(1):70–75, 1990.

[119] Jakob Johannes Van Zyl. *ON THE IMPORTANCE OF POLARIZATION IN RADAR SCATTERING PROBLEMS (SYNTHETIC APERTURE, IMAGING).* California Institute of Technology, 1986.

[120] G Ioannidis and D Hammers. Optimum antenna polarizations for target discrimination in clutter. *IEEE Transactions on Antennas and Propagation*, 27(3):357–363, 1979.

[121] JJ Van Zyl, N Engheta, CH Papas, C Elachi, and H Zebker. Modelling of backscatter from vegetation layers. 1985.

[122] Steffen Heuel and Hermann Rohling. Pedestrian classification in automotive radar systems. In *2012 13th International Radar Symposium*, pages 39–44, 2012.

[123] H. Yamada and T. Horiuchi. High-resolution indoor human detection by using millimeter-wave mimo radar. In *2020 International Workshop on Electromagnetics: Applications and Student Innovation Competition (iWEM)*, pages 1–2, 2020.

[124] Matthias Kronauge and Hermann Rohling. Fast two-dimensional cfar procedure. *IEEE Transactions on Aerospace and Electronic Systems*, 49(3):1817–1823, 2013.

[125] FT Ulaby. *FT Ulaby and C Elachi, Eds.* 1990.

[126] Michael Thiel and Kamal Sarabandi. Ultrawideband multi-static scattering analysis of human movement within buildings for the purpose of stand-off detection and localization. *IEEE Transactions on Antennas and Propagation*, 59(4):1261–1268, 2011.

[127] Mehrnoosh Vahidpour and Kamal Sarabandi. Millimeter-wave doppler spectrum and polarimetric response of walking bodies. *IEEE Transactions on Geoscience and Remote Sensing*, 50(7):2866–2879, 2012.

[128] Amr A. Ibrahim and Kamal Sarabandi. Sub-terahertz dielectric measurement and its application to concealed object detection. *IEEE Transactions on Terahertz Science and Technology*, 5(3):445–455, 2015.

[129] Merrill I Skolnik. *Radar handbook*. McGraw-Hill Education, 2008.

[130] Matthias Kronauge and Hermann Rohling. New chirp sequence radar waveform. *IEEE Transactions on Aerospace and Electronic Systems*, 50(4):2870–2877, 2014.

[131] Po Li, De-Chun Wang, and Lu Wang. Separation of micro-doppler signals based on time frequency filter and viterbi algorithm. *Signal, Image and Video Processing*, 7(3):593–605, 2013.

[132] Przemyslaw Mazurek. Estimation of micro-doppler signals using viterbi track-before-detect algorithm. In *2017 22nd International Conference on Methods and Models in Automation and Robotics (MMAR)*, pages 898–902. IEEE, 2017.

[133] Graeme Edward Smith. *Radar target micro-Doppler signature classification*. University of London, University College London (United Kingdom), 2008.

[134] Michael Glen Anderson. *Design of multiple frequency continuous wave radar hardware and micro-Doppler based detection and classification algorithms*. The University of Texas at Austin, 2008.

[135] Svante Björklund, Henrik Petersson, and Gustaf Hendeby. Features for micro-doppler based activity classification. *IET radar, sonar & navigation*, 9(9):1181–1187, 2015.

[136] JJM De Wit, RIA Harmanny, and P Molchanov. Radar micro-doppler feature extraction using the singular value decomposition. In *2014 International Radar Conference*, pages 1–6. IEEE, 2014.

[137] Victor C. Chen. *The micro-Doppler effect in radar*. Artech House radar series. Artech House, second edition. edition, 2019.

[138] Benjamin Wolfe, Bobbie Seppelt, Bruce Mehler, Bryan Reimer, and Ruth Rosenholtz. Rapid holistic perception and evasion of road hazards. *Journal of experimental psychology: general*, 149(3):490, 2020.